IONOSPHERIC ELECTRON DENSITY AND T_e/T_i ESTIMATION USING INCOHERENT SCATTER POWER DATA COLLECTED AT ALTAIR

BY

MARCO ANTONIO MILLA

Bachiller en Ingeniería Electrónica, Pontificia Universidad Católica del Perú, 2001

THESIS

Submitted in partial fulfillment of the requirements
for the degree of Master of Science in Electrical and Computer Engineering
in the Graduate College of the
University of Illinois at Urbana-Champaign, 2006

Urbana, Illinois

To my mother Chela, my father Ñofi, my sister Pili, and my brother Calín.

ACKNOWLEDGMENTS

I would like to express my gratitude to my advisor, Dr. Erhan Kudeki, for his guidance during the development of this work. I appreciate the discussions we exchanged and the time he expended in clarifying my doubts. Additionally, I would like to thank the technical staff at the ALTAIR radar — in particular Dale Sponseller, Robert Ferguson, Linda Schuett, Julie Wathen, and Phillip Phu — for their cooperation and assistance during the NASA EQUIS 2 campaign. This work has been funded at the University of Illinois by NASA and NSF grants NAG5-5368 and ATM-0215246, respectively.

TABLE OF CONTENTS

LIST OF TABLES

LIST OF FIGURES

CHAPTER 1

INTRODUCTION

The main concern of this thesis is the estimation of ionospheric parameters from incoherent scatter (IS) power data collected with the ALTAIR radar. The estimation is performed using a radar calibration and inversion technique based on a forward model of the scattered power. The model considers the physics of the ionosphere in terms of IS radar cross section (RCS) of the medium. The inversion procedure provides the estimates of plasma density and electron-ion temperature ratio (T_e/T_i) of the probed ionosphere. This introductory chapter overviews the incoherent scatter radar (ISR) technique and concludes with an outline of the remaining chapters in the thesis.

1.1 The Incoherent Scatter Radar Technique

Electromagnetic waves traveling thorough a medium with a varying refractive index will be partially reradiated or *scattered* in different directions. In the ionosphere, as in any other plasma, refractive index variations are caused by fluctuations in the density distribution of charged particles that constitute the medium. When ionospheric particles are in thermal equilibrium, the scattering process is termed *incoherent*.

Applications of incoherent scattering for ionospheric research using large and powerful radar systems were first proposed by *Gordon* [1958]. He suggested that incoherent scattering could be used to measure ionospheric electron densities, but it was subsequently discovered that other parameters can also be obtained, e.g., electron and ion temperatures, ion composition, and plasma drifts. A detailed review of these ISR methods and their importance for ionospheric studies can be found in *Beynon and Williams* [1978].

The problem of calculating the spectrum of incoherently scattered radio waves was first addressed by *Dougherty and Farley* [1960], *Fejer* [1960], and others. Different methods of derivation were followed, but the results were nearly the same. Over the years, the theory has been successfully tested on many experimental observations. Using sophisticated algorithms for inversion of ISR data, physical parameters of the background ionosphere are routinely measured in radio observatories distributed around the world [*Evans*, 1969; *Farley*, 1970].

The extension of the spectral theory to include the effects of an external magnetic field was of particular interest for ionospheric research [*Farley et al.*, 1961; *Fejer*, 1961]. The theory showed that the spectrum has some dependence on the magnetic aspect angle α—defined as the complement of the angle between the scattered field wavevector $\vec{k}$ and the ambient magnetic field $\vec{B}$. For α greater than a few degrees, the spectrum is fairly independent of the magnetic aspect angle, and it is only for small α that the dependance shows up. In this regime, the spectrum gets narrower and taller as $\alpha \to 0°$, limit where the wavevector is perpendicular to $\vec{B}$.

A known issue in the theory was its inaccuracy in quantifying the observations at small magnetic aspect angles. Recent experimental techniques developed for modes propagating perpendicular to $\vec{B}$ [*Kudeki et al.*, 1999, 2003] have brought back to light this problem. This was inherited by the spectral models from neglecting the effect of collisions in the physics of the plasma. In the past few years, *Sulzer and González* [1999] and *Woodman* [2004] have tackled the problem. A new model for the spectrum at small magnetic aspect angles has emerged, and further development in radar techniques perpendicular to $\vec{B}$ can be pursued.

1.2 Thesis Outline

Radar scans of the low-latitude ionosphere were conducted with the ALTAIR system during the Equis 2 campaign. An interesting feature of the observations was the increment of the returned power when the radar beam went through a perpendicular direction with respect to the Earth's magnetic field. A detailed description of the radar configuration used in these observations is presented in Chapter 2.

A radar equation that models ALTAIR power data is derived in Chapter 3. The model accounts for the physics of the ionosphere in terms of the total RCS of the medium. Since small aspect angles are involved, the RCS model is based on new theoretical approaches that account for the effect of Coulomb collisions in a plasma [*Woodman*, 2004; *Kudeki and Milla*, 2006].

Taking advantage of the aspect angle sensitivity of the backscattered power collected at ALTAIR, electron densities N_e and T_e/T_i profiles were estimated using the forward model of Chapter 3. For this purpose, accurate calculation of some system calibration constants was required. The methods for the computation of these parameters are developed in the first section of Chapter 4. The second section details the numerical technique used in the data inversions, namely, a regularized least-squares minimization algorithm. The procedure relies on the L-curve criterion for optimal selection of the regularization parameter, and provides smooth profiles of the ionospheric variables.

The proposed ISR technique works for the region around magnetic perpendicularity, and under the plausible assumption of meridional homogeneity of the ionosphere over a horizontal scale of a few hundred kilometers. The results obtained with this method are presented and discussed in Chapter 5.

The thesis concludes in Chapter 6 with a critical discussion of the procedures developed for this application. The work presented here has been recently published by *Milla and Kudeki* [2006] and *Kudeki et al.* [2006]. Moreover, the results have been used for comparison with in situ density measurements carried out by rockets during the Equis 2 campaign [*Friedrich et al.*, 2006; *Lehmacher et al.*, 2006].

CHAPTER 2

RADAR CONFIGURATION AND DATA ACQUISITION

The Advanced Long Range Tracking and Identification Radar (ALTAIR) is a dual-band (VHF and UHF) high-sensitivity radar designed for ballistic missile detection and tracking. It is located on Roi-Namur island of the Kwajalein Atoll in the western Pacific (9.39° N, 167.47° E). Its 150-ft parabolic dish antenna is fully steerable, capable of accelerations of $2°/s^2$ and angular rates of $10°/s$ [*Lemnios and Grometstein*, 2002]. Its transmitter can deliver up to 4 MW of peak power in the UHF band with a maximum duty cycle of 5%. During transmission, circularly polarized pulses are used, while in reception, both right- and left-circularly polarized returns can be monitored and detected independently. These characteristics, in addition to its unique location with respect to the Earth's magnetic equator (4.3° N geomagnetic latitude), make ALTAIR suitable for IS observations of the equatorial and low-latitude ionosphere.

2.1 Experiment Description

During the 2004 Equis 2 NASA rocket campaign, ISR measurements of the low-latitude daytime ionosphere were conducted by the ALTAIR UHF radar. The measurements were made for common volume comparisons with rocket based D- and E-region electron density estimates described in *Friedrich et al.* [2006]. During the observations, the ALTAIR beam was scanned along a north-south oriented plane that coincides with the rocket trajectories, and incoherently scattered returns were

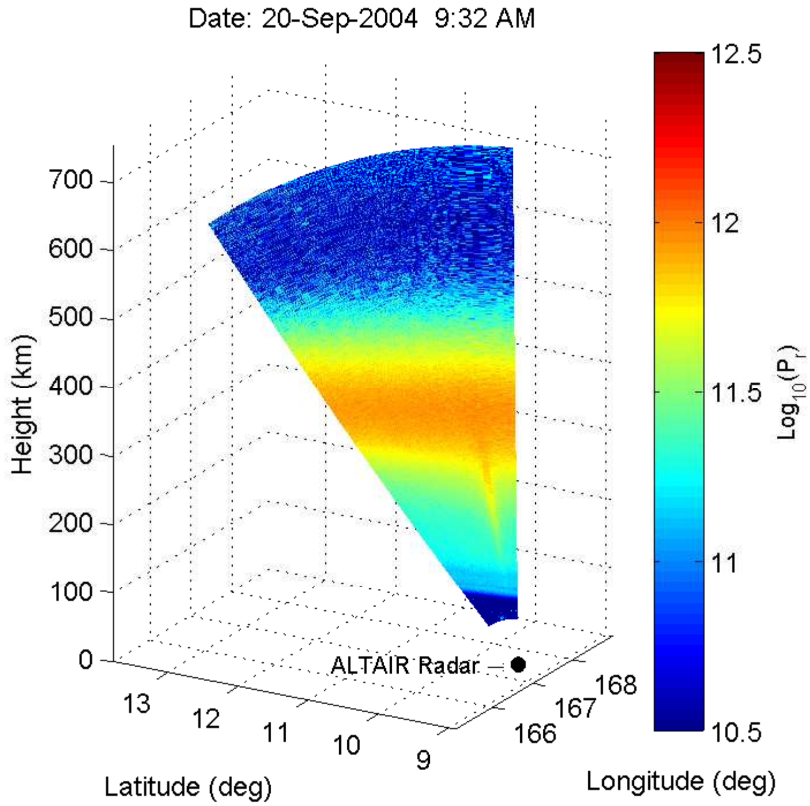

Figure 2.1 An example of the ALTAIR scan measurements collected during the Equis 2 campaign. In colors, levels of backscattered power calibrated to match electron densities in the probed region are displayed.

sampled from D-region heights up to the topside F-region. The scan geometry and radar data collected in a single scan are illustrated in Figure 2.1 where the color map corresponds to the logarithm of the backscattered power.

In the scans, the radar beam was swept along the $-13.5°$ azimuth plane starting from an elevation angle of 50° up to zenith position and steering at an angular rate of 8 s/deg. Thus, each scan lasted about 5 min and 20 s. As the beam moves, ALTAIR probed the ionosphere at different magnetic aspect angles, going through a perpendicular orientation with respect to the geomagnetic field at an elevation around 80°. The perpendicular orientation coincides with the spike-like intrusion seen in Figure 2.1. This is better illustrated in Figure 2.2 where power is now

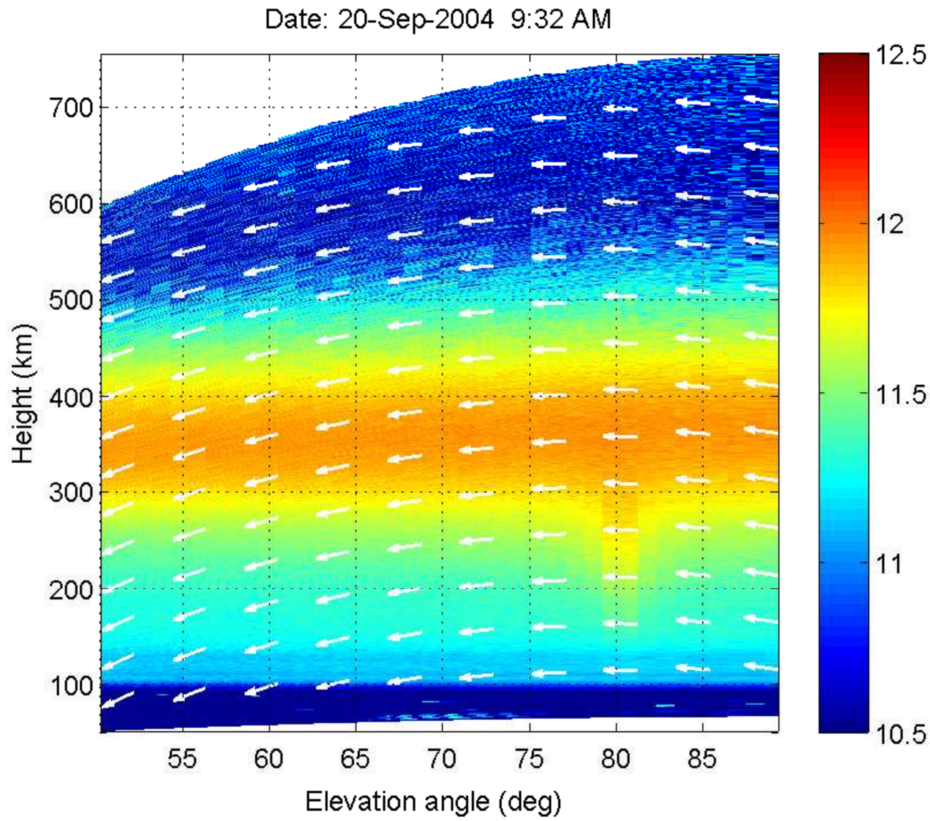

Figure 2.2 Backscattered power data displayed as function of beam elevation angle and height. The white arrows depict the relative orientation of the geomagnetic field with respect to the radar beam direction. Note that the power enhancement at an elevation $\sim 80°$ corresponds to altitudes where $T_e > T_i$ and the radar line-of-sight is perpendicular to $\vec{B}$.

displayed as a function of elevation angle and height. The superposed white arrows depict the relative orientation of the geomagnetic field $\vec{B}$ with respect to the radar beam direction. The enhanced power corresponding to the spike observed in both figures is characteristic of the incoherent scatter process in regions where the electron temperature exceeds the ion temperature (i.e., $T_e > T_i$) and the probing direction is perpendicular to $\vec{B}$.

Table 2.1 presents a summary of the primary ALTAIR parameters configured for these ionospheric scans. As indicated, the radar was operated using an LFM waveform (chirped pulse) of 400 μs duration, 422 MHz center frequency, 250 kHz

Table 2.1 Experiment configuration.

Radar parameters	
Peak power	4 MW
Radar frequency	422 MHz
Pulse modulation	250 kHz LFM
Pulse width	400 μs (60 km)
Inter-pulse period	8.3 ms (1250 km)
Sampling rate	1.6 μs (240 m)
Range	65 - 755 km
Samples per pulse	2874
Pulses per scan	38400
Scan duration	5 min and 20 s
Angular scan rate	8 s/deg

bandwidth, and a 120 Hz pulse repetition frequency (PRF) that corresponds to an interpulse period (IPP) of 8.33 ms. In total, 38400 pulses were transmitted during each scan. Note that this sampling period is longer than typical correlation times of the ISR signal returns (that are less than 1 ms for ALTAIR's radar wavelength). Thus, the signal spectrum is severely aliased, making impossible the estimation of meaningful ionospheric parameters using any pulse-to-pulse correlation or spectral analysis. However, we were able to make meaningful estimations by taking advantage of the magnetic aspect angle dependence of the measured power. The effects introduced due to LFM modulation of the transmitted pulse—and subsequently matched-filter detection of the returned signal—are properly accounted for in our inversion procedure, and will be described and formulated in the next chapter.

2.2 Radar Power Profiles

As mentioned previously, the ALTAIR antenna is configured to independently detect right- and left-circularly polarized returns using coherent and matched-filter reception. During the radar scans, outputs of these complex channels were sampled

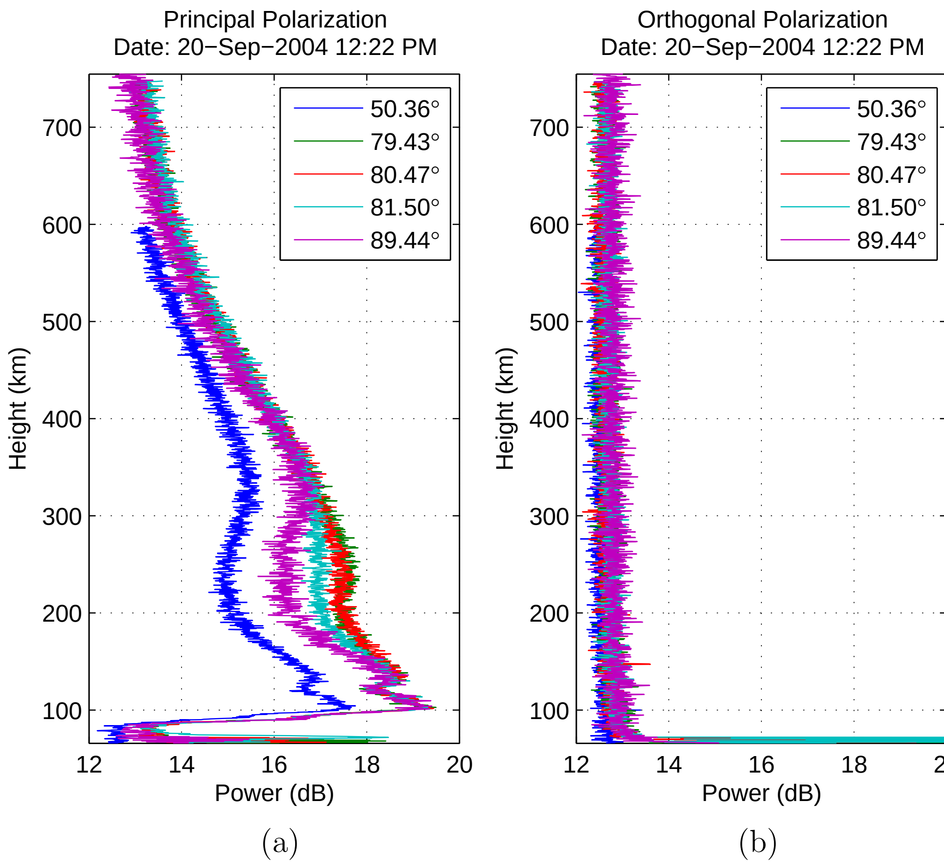

Figure 2.3 ALTAIR echo power measured in both (a) "principal" and (b) "orthogonal" antenna channels that are right- and left-circularly polarized. Each profile corresponds to a different elevation angle. Note that depolarization of the returned signal was not detected because generalized Faraday effects are negligible at 422 MHz.

at a rate corresponding to 240 m range spacing, and a total of 2874 gates were taken covering radar ranges between 65 and 755 km.

In Figure 2.3, radar echo power calculated from the sampled voltages at both receiver outputs are plotted as function of height. Each individual profile corresponds to a different elevation angle of the radar beam and represents an integration over 1000 radar pulses. This is equivalent to 8.33 s of data during which the beam moves about one degree. We can notice that only the channel labeled as "principal polarization" contains backscattered power, indicating that possible depolarization effects can be neglected in our analysis. This is an expected result, not only because circularly polarized transmissions correspond to a normal mode of propagation for most scanning directions involved, but also because generalized Faraday effects [*Yeh et al.*, 1999] are very weak at 422 MHz even for propagation perpendicular to the geomagnetic field (in which case the normal modes are linearly polarized).

During the Equis 2 campaign, ALTAIR was operated in this mode on September 20, 21, and 25, 2004. A collection of radar scans were recorded at unequally spaced time intervals and only for daytime hours. In addition, "control" data was taken on January 15, 2005. In the next chapter, we develop a quantitative model for the enhanced power data detected by the principal polarization channel, which is subsequently used in Chapter 4 to estimate N_e and T_e/T_i profiles of the low-latitude ionospheric regions.

CHAPTER 3

INCOHERENT SCATTER POWER MODEL

In this chapter, we present a soft-target radar equation for the incoherently scattered power data recorded by ALTAIR. The radar power is modeled in terms of the IS radar cross section, which is a function of plasma density, electron-ion temperature ratio, and magnetic aspect angle [*Farley*, 1966]. In addition, pulse compression effect due to matched-filter detection is considered in terms of the radar ambiguity function (AF). Our model explains and quantifies the angular variability of the backscattered signal at small magnetic aspect angles. In this regime, the effects of electron and ion Coulomb collisions become important [*Sulzer and González*, 1999] and have to be considered in the RCS model. This is accomplished by following the procedure outlined in *Kudeki and Milla* [2006] based on the collisional incoherent scatter spectrum model developed by *Woodman* [1967], and the empirical collision frequency formula proposed by *Woodman* [2004].

3.1 Radar Equation and Ambiguity Function

In soft-target Bragg scattering each infinitesimal volume $dv \equiv r^2 dr d\Omega$ of a radar field-of-view behaves like a hard-target with a radar cross section $dv \int \frac{d\omega}{2\pi}\sigma(\vec{k},\omega)$, where $\sigma(\vec{k},\omega)$, by definition, is soft-target RCS per unit volume per unit Doppler frequency $\frac{\omega}{2\pi}$, and $\vec{k} \equiv -2k_o\hat{r}$ denotes the relevant Bragg vector for a radar with a carrier wavenumber k_o. As a consequence, the hard-target radar equation generalizes for soft-target Bragg-scatter radars as

$$P_r(t) = \int dr\, d\Omega\, \frac{d\omega}{2\pi}\, \frac{G(\hat{r})A(\hat{r})}{(4\pi r)^2}\, P_t(t - \frac{2r}{c})\, \sigma(\vec{k}, \omega), \tag{3.1}$$

where $P_t(t) \propto |f(t)|^2$ is the transmitted power carried by a pulse waveform $f(t)$, $G(\hat{r})$ and $A(\hat{r})$ are the gain and effective area of the radar antenna as a function of radial unit vector $\hat{r}$, r is the radar range, and c the speed of light. Furthermore, equation (3.1), which assumes an open radar bandwidth, can be recast for a match-filtered receiver output as

$$\frac{P_r(t)}{E_t K_s} = \int dr\, d\Omega\, \frac{d\omega}{2\pi}\, \frac{g^2(\hat{r})}{r^2}\, |\chi(t - \frac{2r}{c}, \omega)|^2\, \sigma(\vec{k}, \omega), \tag{3.2}$$

where E_t is the total energy of the transmitted radar pulse, K_s denotes a system calibration constant including loss factors ignored in (3.1), $g(\hat{r})$ is the self-normalized version of $G(\hat{r})$, and

$$\chi(\tau, \omega) \equiv \frac{1}{T} \int dt\, e^{j\omega t}\, f(t) f^*(t - \tau) \tag{3.3}$$

has a magnitude known as radar *ambiguity function* [*Levanon*, 1988]. In (3.3) the normalization constant T denotes the duration of pulse waveform $f(t)$ and (3.3) itself is effectively the normalized cross-correlation of Doppler-shifted pulse $f(t)\, e^{j\omega t}$ with a delayed pulse echo $\propto f(t - \tau)$ that would be expected from a point target located at a radar range

$$R \equiv c\,\tau/2. \tag{3.4}$$

Hence, variable τ in (3.3) not only represents a time delay, but also a corresponding radar range R. We will refer to τ as delay or range as we find convenient in the following discussion. A detailed derivation of Equations (3.2) and (3.3) is offered in

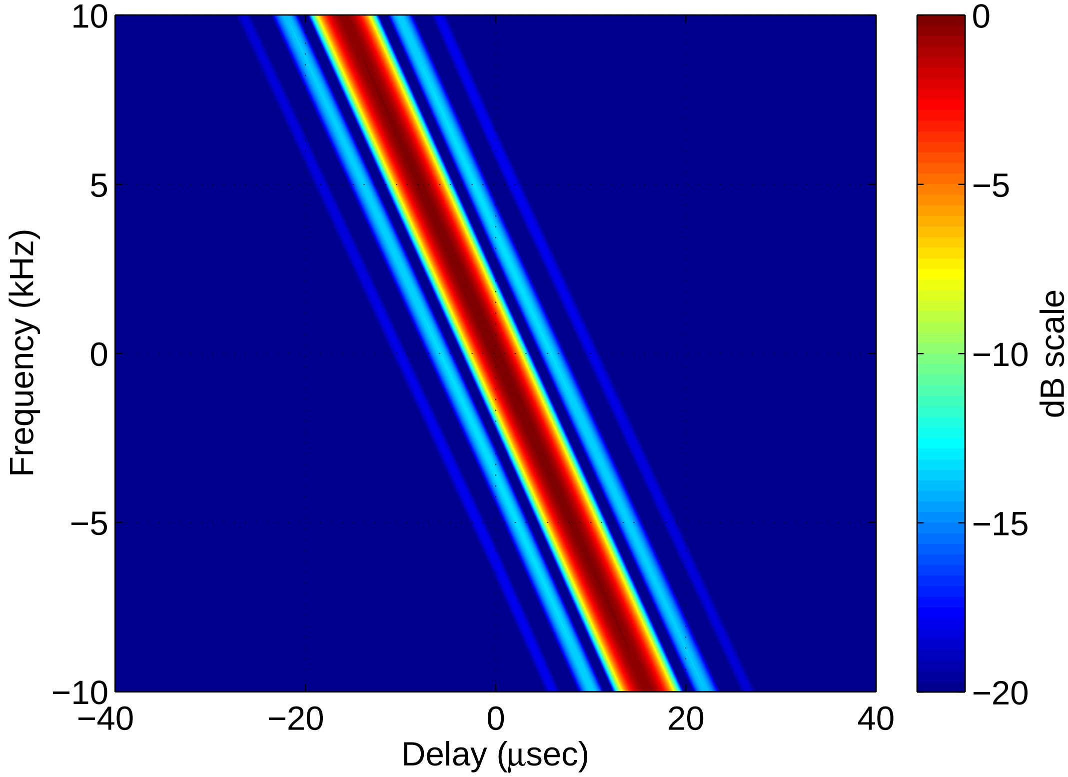

Figure 3.1 Ambiguity function $|\chi(\tau, \omega)|$ of a chirped pulse of width $T = 400\,\mu\mathrm{s}$ and frequency span $\Delta f = 250\,\mathrm{kHz}$.

Appendix A.

In our experiment, we have used a chirped pulse waveform

$$f(t) = \mathrm{rect}(t/T)\, e^{j\frac{\beta}{2}t^2}, \tag{3.5}$$

which, in effect, causes a slow linear variation of the carrier frequency over a bandwidth Δf and at a rate $\frac{\beta}{2\pi} = \frac{\Delta f}{T}$. The corresponding ambiguity function,

$$|\chi(\tau, \omega)| = \triangle(\frac{\tau}{2T})\, |\mathrm{sinc}(\frac{(T - |\tau|)(\omega + \beta\tau)}{2})|, \tag{3.6}$$

is plotted in Figure 3.1 for $T = 400\,\mu\mathrm{s}$ and $\Delta f = 250\,\mathrm{kHz}$ (parameters used in the experiment). This expression is derived in Appendix B.

According to formula (3.6), the overall width of $|\chi(\tau, \omega)|$ along the delay axis τ over the frequency bandwidth B of the RCS spectrum corresponds to $2\pi B/\beta$ (given $B \ll \Delta f$), which implies a range resolution Δr—defined as the range separation between independent measurements—described by

$$\frac{2\Delta r}{c} = \frac{2\pi B}{\beta} = \frac{TB}{\Delta f}. \tag{3.7}$$

For instance, for a plausible ionospheric bandwidth of $B = 10\,\text{kHz}$, the range resolution is $\Delta r = 2.4\,\text{km}$. In addition, any mean Doppler shift of the RCS spectrum will imply a displacement of the actual position of the backscatter signal; such a displacement can be estimated as

$$d = f_o T \frac{v_d}{\Delta f}, \tag{3.8}$$

where v_d is the Doppler shift measured in m/s and f_o the radar carrier frequency in Hz. In ionospheric observations, possible Doppler shifts are around 100 m/s, with a corresponding displacement of about 67 m, a small fraction of the range resolution Δr that can be safely neglected.

Assuming that $\sigma(\vec{k}, \omega)$ varies slowly with the radar range r, and that the AF is almost flat within the bandwidth of the RCS spectrum (which is the case of this application), we can simplify Equation (3.2) to obtain

$$\frac{P_r(R)}{E_t K_s} \approx \frac{\delta R}{R^2} \int d\Omega\, g^2(\hat{r})\, \sigma_{\scriptscriptstyle T}(\vec{k}), \tag{3.9}$$

where $R = \frac{ct}{2}$ is the measured radar range,

$$\delta R \equiv \int dr\, |\chi(\frac{2}{c}(R - r), 0)|^2 \tag{3.10}$$

is the effective range depth of the radar scattering volume, and

$$\sigma_T(\vec{k}) \equiv \int \frac{d\omega}{2\pi}\,\sigma(\vec{k},\omega) \tag{3.11}$$

is the total volumetric RCS where dependence on range R is implied.

3.2 Incoherent Scatter RCS Spectrum (σ)

The IS theory establishes that the volumetric RCS spectrum of a quiescent ionosphere can be written as [*Dougherty and Farley*, 1960; *Farley et al.*, 1961]

$$\sigma(\vec{k},\omega) = 4\pi r_e^2\,\langle|n_e(\vec{k},\omega)|^2\rangle \tag{3.12}$$

where r_e is the classical electron radius and

$$\begin{aligned}\langle|n_e(\vec{k},\omega)|^2\rangle \;\; = \;\; & \frac{2N_e}{\omega}\left\{\frac{|jk^2\lambda_e^2+\mu y_i(\vec{k},\omega)|^2\,\mathrm{Re}\{y_e(\vec{k},\omega)\}}{|jk^2\lambda_e^2+y_e(\vec{k},\omega)+\mu y_i(\vec{k},\omega)|^2}\right. \\ & \left. + \frac{|y_e(\vec{k},\omega)|^2\,\mathrm{Re}\{y_i(\vec{k},\omega)\}}{|jk^2\lambda_e^2+y_e(\vec{k},\omega)+\mu y_i(\vec{k},\omega)|^2}\right\}\end{aligned} \tag{3.13}$$

denotes the space-time spectrum of electron density fluctuations. Above, N_e is the mean electron density, λ_e is the electron Debye length, μ the temperature ratio T_e/T_i, and y_e and y_i are normalized electron and ion admittance functions proportional to conductivities in the medium. These admittances can be expressed as

$$y_s = j + \theta_s\,J_s(\theta_s), \tag{3.14}$$

where s denotes each species (electrons or ions) and $\theta_s \equiv \frac{\omega}{\sqrt{2}kC_s}$ is the frequency normalized by wavenumber k and thermal speed C_s. The function J_s, which will be specified later, is a Gordeyev integral that can be interpreted as one-sided Fourier transform of normalized autocorrelation of echoes from charged particles in the absence of collective interactions [*Hagfors and Brockelman*, 1971].

3.3 Efficiency Factor of Electron Scattering (η)

Replacing expression (3.12) in (3.9), we have

$$\frac{P_r(R)}{E_t K_s} \approx \frac{4\pi r_e^2\, N_e(R)\, \delta R}{R^2} \int d\Omega\, g^2(\hat{r})\, \eta(\vec{k}), \tag{3.15}$$

where

$$\eta(\vec{k}) \equiv \int \frac{d\omega}{2\pi} \frac{\langle |n_e(\vec{k},\omega)|^2 \rangle}{N_e} \tag{3.16}$$

is the efficiency factor of electron scattering that is $\frac{1}{2}$ in a plasma in thermodynamic equilibrium, or, more generally, $(1+\frac{T_e}{T_i})^{-1}$ in a nonmagnetized plasma with an arbitrary T_e/T_i and negligible Debye length [*Farley*, 1966]. However, in our forward model, we will need the efficiency η for a magnetized plasma with an arbitrary T_e/T_i and for arbitrarily small aspect angles α.

In general, noncollisional models for (3.13) become singular as $\alpha \to 0°$ and make numerical evaluation of η impossible in the same limit. This difficulty can be circumvented by using a collisional model for (3.13). In our computations of η, we used the collisional model developed by *Woodman* [1967], which is based on a simplified Fokker-Planck operator for Coulomb collisions, the relevant collision process for F-region altitudes [*Sulzer and González*, 1999]. The model leads to a Gordeyev integral [*Kudeki et al.*, 1999; *Kudeki and Milla*, 2006]

$$\begin{aligned} J_s(\theta_s) \;&=\; \int_0^\infty dt\, e^{-j\theta_s t}\, e^{-\frac{\psi_s t - 1 + e^{-\psi_s t}}{2\psi_s^2}\sin^2\alpha} \\ &\qquad e^{-\frac{\cos(2\gamma_s)+\psi_s t - e^{-\psi_s t}\cos(\phi_s t - 2\gamma_s)}{2(\psi_s^2+\phi_s^2)}\cos^2\alpha}, \end{aligned} \tag{3.17}$$

where $\psi_s \equiv \frac{\nu_s}{\sqrt{2}kC_s}$ and $\phi_s \equiv \frac{\Omega_s}{\sqrt{2}kC_s}$ are normalized collision- and gyro-frequencies, respectively, and $\gamma_s \equiv \tan^{-1}(\frac{\nu_s}{\Omega_s})$. For ν_i and ν_e we make use of the collision frequency models of *Woodman* [1967] and *Woodman* [2004], respectively, which are

$$\nu_i/\nu_{i0} = 0.601 \tag{3.18}$$

and (Equation (14) in the original paper)

$$\begin{aligned}\nu_e/\nu_{e0} &= 1.06 + 7.55\,\sin\alpha/\sin\alpha_c - 2.00\,(\sin\alpha/\sin\alpha_c)^2 \\ &\quad + 0.27\,(\sin\alpha/\sin\alpha_c)^3,\end{aligned} \tag{3.19}$$

where $\alpha_c \equiv \sin^{-1}(\frac{2\pi\nu_{e0}}{kC_e})$ is a critical aspect angle and

$$\nu_{s0} \equiv \frac{e^4 N_e}{4\pi\epsilon_0^2 m_s^{1/2}(2KT_s)^{3/2}} \ln(24\pi\lambda_e^3 N_e) \tag{3.20}$$

is the so-called Spitzer collision frequency for species s (electrons or ions).

In numerical evaluations of η, Gordeyev integrals J_s were computed using a chirped z-transform algorithm suggested by *Li et al.* [1991]. Each integral was evaluated for a total of 2^{15} sample frequencies equally spaced from 0 to 125 kHz. The algorithm samples the integrand of J_s in sections of the same length, and adds iteratively the contribution of each section as it is needed for convergence of the integral. Despite the accuracy that this algorithm provides, it became computationally demanding to obtain J_s at angles close to perpendicular to $\vec{B}$ because of the narrowness of the IS spectrum in this regime. Nevertheless, computations were possible even at $\alpha = 0°$ as a consequence of the collisional model used.

The efficiency factor η has been calculated for different values of aspect angle α, temperature ratio T_e/T_i, and electron density N_e. As an example, Figure 3.2(a) displays the values of η computed for a constant density of $10^{12}\,\mathrm{m}^{-3}$ and $T_e = 1000\,\mathrm{K}$.

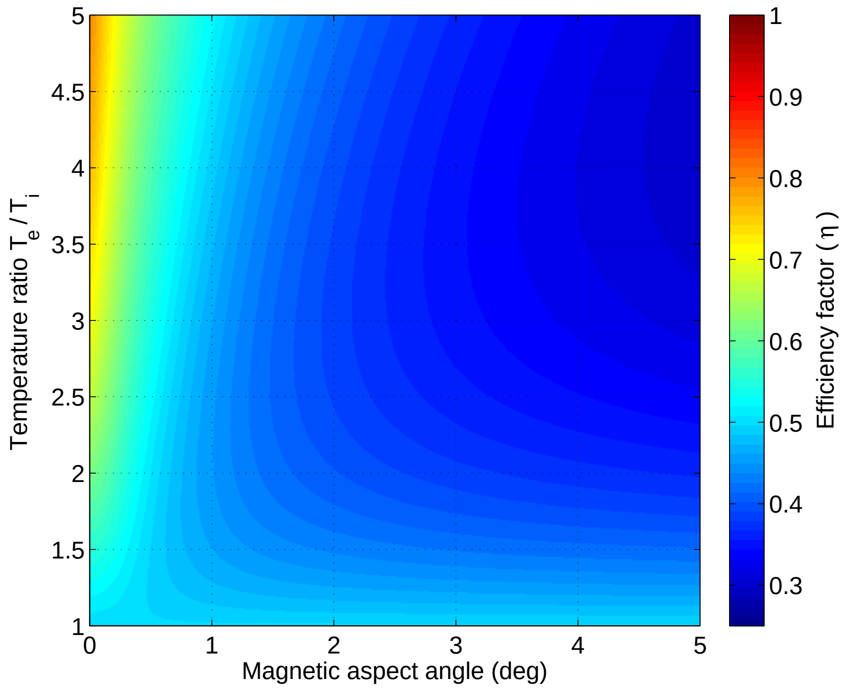

(a)

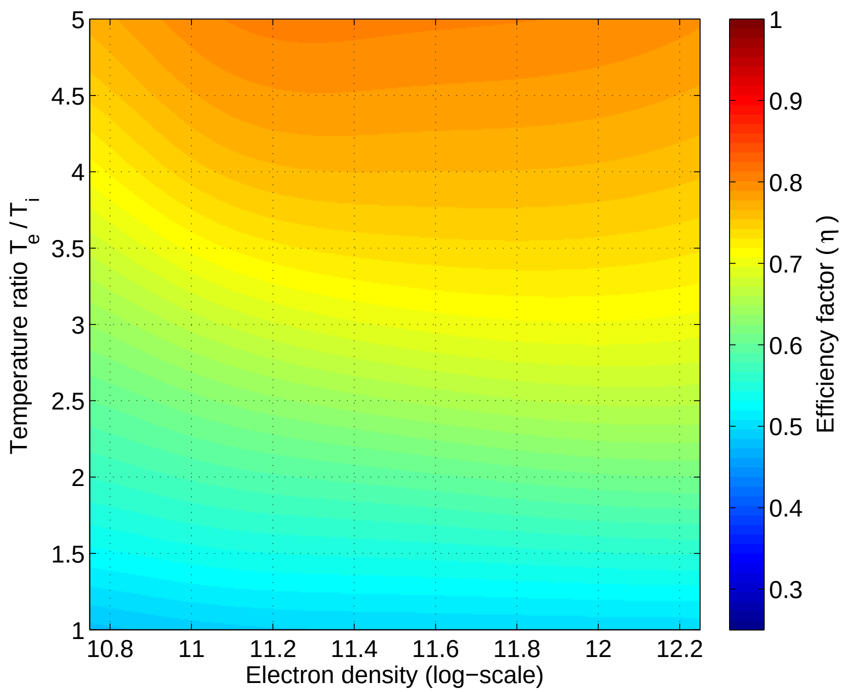

(b)

Figure 3.2 Efficiency factor η as function of (a) magnetic aspect angle vs. T_e/T_i for a constant electron density of $10^{12}\,\mathrm{m}^{-3}$, and (b) electron density vs. T_e/T_i for $\alpha = 0°$ (perpendicular to $\vec{B}$). Both graphics correspond to the case of $T_e = 1000\,\mathrm{K}$.

Here, note that the dependence of η on the magnetic aspect angle becomes relevant for small α (smaller than $\sim 3^{\circ}$). In addition, Figure 3.2b shows the variation of the efficiency factor as function of N_e for $\alpha = 0^{\circ}$ and $T_e = 1000\,\mathrm{K}$. In this case, η increases as T_e/T_i rises from unity. Note that the rate of change is not uniform for different density values.

Overall, it was found that η is not highly sensitive to variations of the collision frequency parameter. For instance, increasing ν_e by factor of 3 or decreasing it by a factor of 10 did not change the computed η values by more than $\sim 1\%$. On the other hand, drastic changes, such as a factor of 30 increase in ν_e, cause noticeable changes in the efficiency factor.

CHAPTER 4

RADAR CALIBRATION AND INVERSION TECHNIQUE

Accurate estimates of ALTAIR radar calibration parameters are required for the utilization of the IS power model presented in the previous chapter. The experimental procedures followed in the determination of these parameters are described in Section 4.1. In addition, Section 4.2 presents the regularized least-squares minimization algorithm used in the estimation of densities N_e and temperature ratios T_e/T_i from IS power data. The technique relies on a graphic criterion for optimal selection of the regularization parameter denominated L-curve.

4.1 Calibration and Power Model Calculations

The use of radar equation (3.15) to model the measured power data requires the availability of transmitted pulse energy E_t and system constant K_s. Since the transmitted peak power P_t is recorded in ALTAIR data headers on a per pulse basis, the pulse energy is trivially obtained as $E_t \equiv P_t T$. In addition, the K_s value that accounts for all the losses and gains of the entire radar system is calculated from peak power measurements conducted with a spherical target of a known RCS. This calibration is routinely performed at ALTAIR and its value is also stored in the data headers.

In addition, the effective range depth δR needed in the power model (3.15) can be computed either analytically by replacing (3.6) in the definition (3.10), or experimentally by integrating the radar response due to a single point target. The second

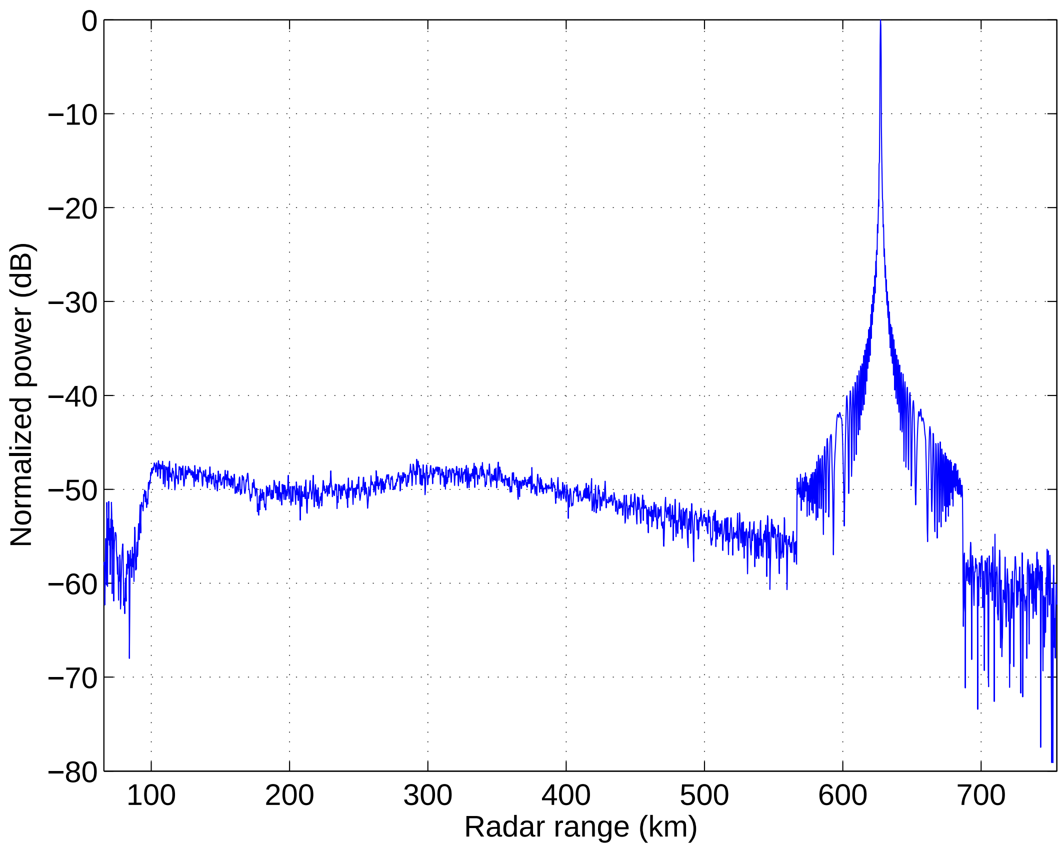

Figure 4.1 Example of the radar response due to a single point target used in the calibration of the effective range depth δR. The measured power corresponds to an integration over 100 pulses and it is normalized to its peak value.

approach provides a more accurate estimate of δR given that any systematic imperfection in the pulse generation is intrinsically taken into account. Some examples of point target radar responses—as the one displayed in Figure 4.1—were selected and then integrated to calculate δR for each of them. The minimum of these values was chosen as the appropriate δR and it is equal to 633.2 m. Note that this calibrated constant is a little larger than its analytical value (~ 600 m).

The computation of the solid angle integral in (3.15) was simplified assuming that ionospheric parameters do not vary locally in longitude. Therefore, only changes along the direction of the scan were considered. This assumption is justified by the narrowness of the ALTAIR UHF antenna beam with a beam-width of less than one degree. As a result, we collapsed the solid angle integral into a 1-D angular integral along the direction of the scan.

We considered two different approaches to evaluate the angular integral just described: The first one corresponds to assuming a fixed beam direction during the transmission of the 1000 pulses used to obtain a single averaged power profile. This approach is justified if the efficiency factor η varies linearly across the beam, in which case, it can be replaced by its central value and reduce the integral to the calculation of an equivalent solid angle defined as

$$\delta\Omega \equiv \int d\Omega \, g^2(\Omega). \tag{4.1}$$

This simplifies the radar equation (3.15) into

$$\frac{P_r(R)}{E_t K_s} \approx \frac{4\pi r_e^2 \, \delta R \, \delta\Omega}{R^2} \, N_e(R) \, \eta(\hat{k}), \tag{4.2}$$

where vector $\vec{R} \equiv R\,\hat{k}$ is the position vector of the scattering parcel with respect to the radar location. Because only a few points of ALTAIR's UHF antenna pattern were available from calibration measurements, we made use of a polynomial interpolation to increase the angular grid of the normalized antenna gain. Using these interpolated data, the solid angle was determined to be $\delta\Omega = 2.0272 \times 10^{-4}$ sterad.

In the second approach, we accounted for the effect of the angular displacement of the beam from pulse to pulse and averaged 1000 profiles corresponding to each beam position to obtain a model profile for the measured power data. Comparison of the two methods revealed negligible differences in test cases, and, as a consequence, the bulk of the results to be presented in the next chapter were obtained using the less costly first approach.

4.2 Regularized Inverse Algorithm

A regularized least-squares inverse algorithm [*Tikhonov and Arsenin*, 1977] was used to perform electron density and T_e/T_i estimations from the modeled power data. In general, a regularization technique allows us to introduce some prior information about the characteristics of the parameters to be estimated in order to obtain better results. Next, we will describe our algorithm and the assumptions made in this work.

First, the ionosphere was envisioned as a stratified medium composed of layers of a fixed width that extend along longitude and latitude following the curvature of the Earth, such that, in each layer, the density and temperature ratio can be considered constants. Below, the vectors $\vec{N}_e$ and $\vec{T}_r$ denote respectively the electron density and T_e/T_i profiles that were estimated after minimization of the following cost function

$$\underbrace{\sum_i \left(\frac{p_m^i - P_r^i(\vec{N}_e, \vec{T}_r)}{\sigma_p^i} \right)^2}_{\text{Data-term}} + \underbrace{\lambda^2 \sum_j (T_r^{j+1} - T_r^j)^2}_{\text{Regularization-term}} . \tag{4.3}$$

In this expression, p_m is the measured power collected by the radar, and P_r and σ_p denote its model and standard deviation, respectively. Our power model also accounts for the background noise level detected by the radar receiver, a level that was estimated from samples taken below 80 km altitude. Above, the variable λ denotes the regularization parameter, and its significance will be discussed later in this section.

In expression (4.3), the index i implies summation over a set of radar ranges and scanning angles that correspond to the region where the power enhancement was observed. Thus, we are considering seven data profiles whose magnetic aspect angles are between $-2.5°$ and $2.5°$ (corresponding to scanning directions between

77° and 83° elevation). In range, samples taken each 6 km (which is also the width of each j-th layer) provide good enough resolution to characterize the F-region.

The simple form of the data-term in (4.3) is justified by the independence of our measurements. Based on our AF analysis, we know that samples with a separation of 6 km are range independent. In addition, given that the interpulse period of the experiment (8.33 ms) was longer than the correlation time of ISR returns, there is no angular or pulse-to-pulse correlation between power profiles. Therefore, we can define the standard deviation of the measured power as $\sigma_p \equiv \frac{p_m}{\sqrt{n_i}}$, being n_i the number of incoherent integrations (averages) performed to obtain an individual profile, in this case $n_i = 1000$. Here, it is useful to indicate that at 422 MHz, the correlation time of beam weighted ISR returns coming from the region around perpendicular to $\vec{B}$ is of the order of 1 ms.

From the analysis of our power model, it turns out that the dependence of the measurements on the plasma density is stronger than its dependence on T_e/T_i. Therefore, at ranges with relatively low SNR, the inverted T_e/T_i values may be very noisy. This fact motivated the inclusion of the regularization-term in the cost function (4.3) which is the discrete gradient of the temperature ratio profile weighted by λ. Our goal in applying this regularization is to obtain smooth and unbiased T_e/T_i estimates.

The outcome of the inversion procedure has some dependence on the right choice of the regularization parameter. An optimal value of λ reduces the noise variance in the inversion results without biasing the model appreciably away from the measured data. *Hansen* [1992] describes a graphical technique for choosing the regularization parameter which is named L-curve and consists in plotting the residuals of the data- and regularization-terms for different realizations of λ. The shape of this curve usually resembles an L and its “corner” or point of maximum curvature provides the optimal regularization parameter. The method is based on the criterion of

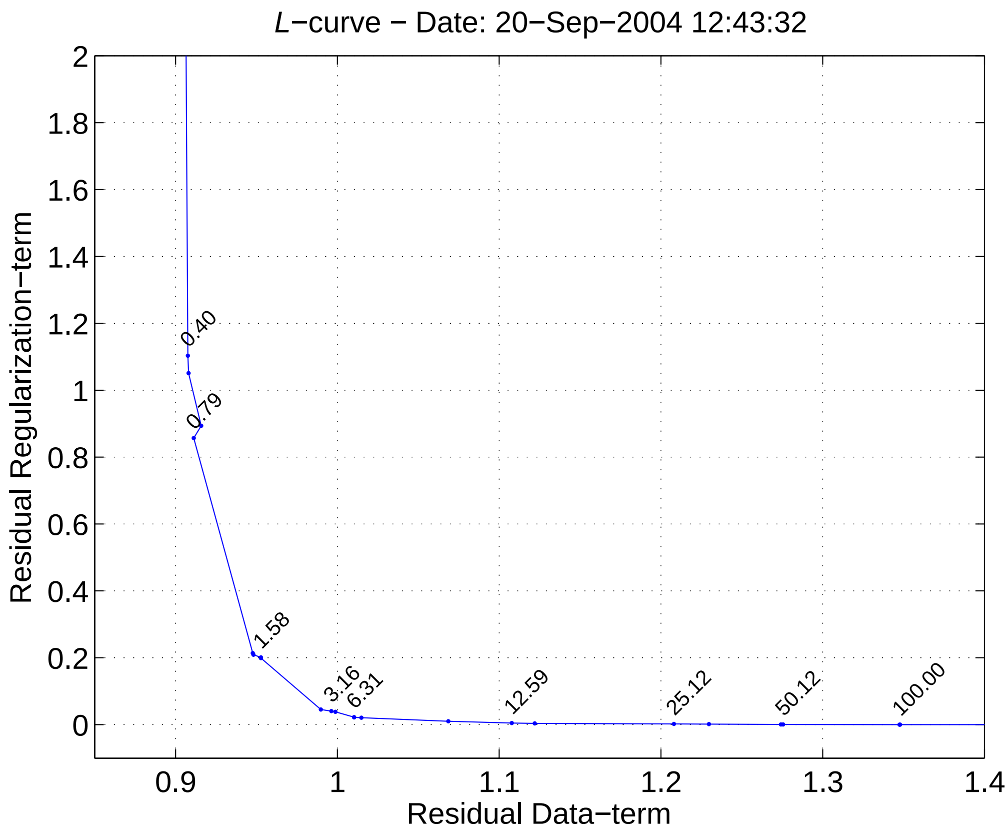

Figure 4.2 Example of the L-curves we have computed for optimal selection of the regularization parameter. Note that the corner of the curve represents a trade-off between the residuals of the data- and regularization-terms.

equalizing the contributions of each term in the cost function (4.3).

Figure 4.2 displays one of the L-curves we computed for the data collected on September 20, 2004. In this case, a value of $\lambda = 1.58$ provided the desired quality in our estimated profiles. Furthermore, we noticed that the L shape is not very sharp around the corner, and regularization parameters between 1 and 2 produced almost the same quality in the results. For other scans, we found optimal parameters within the same range; therefore, we chose a constant value of $\lambda = 1.5$ for all the estimations we performed.

In Figure 4.3, we show some of the outputs of the inverse procedure corresponding to the same case of Figure 4.2. The first two columns display the measured

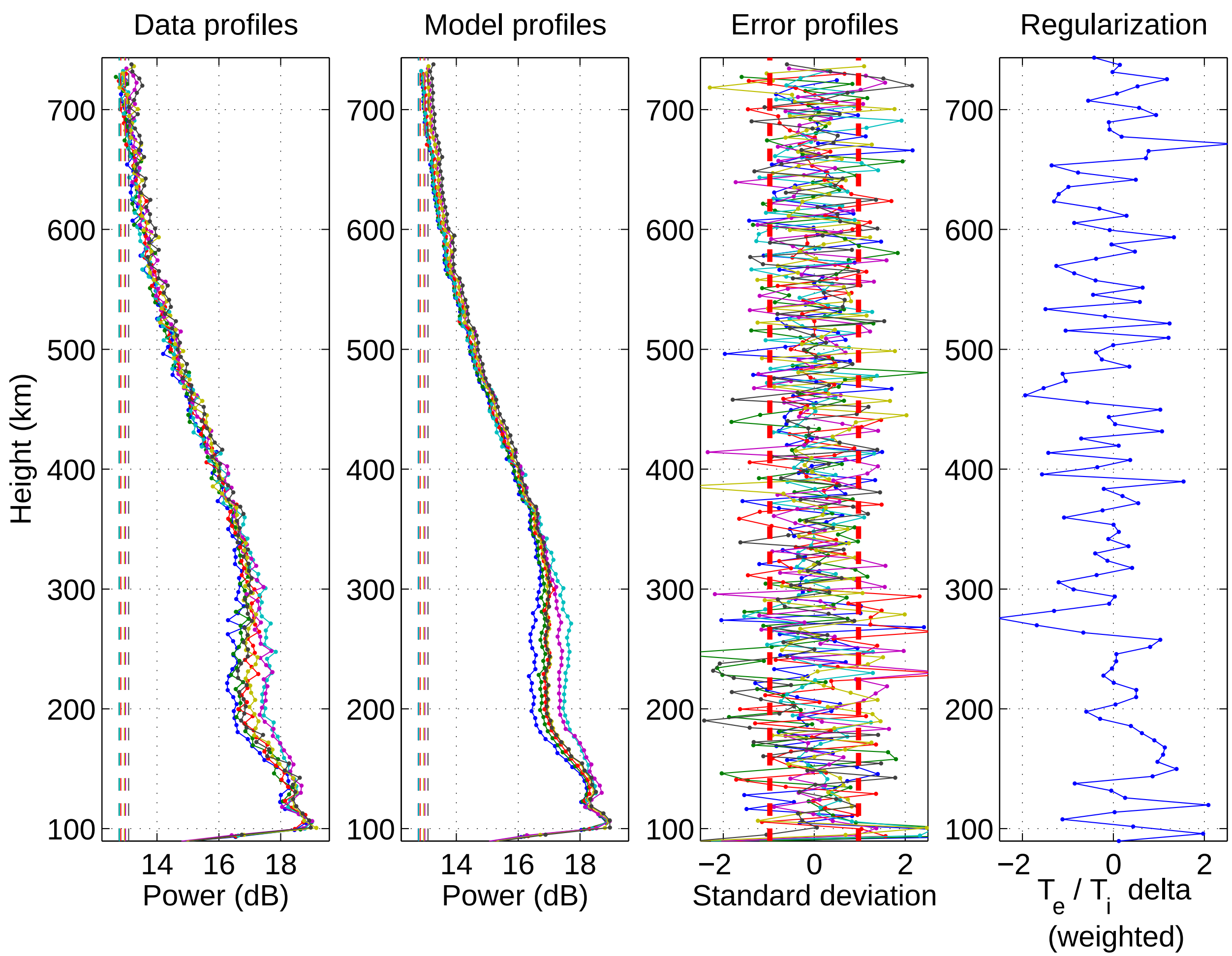

Figure 4.3 Outputs of the fitting algorithm: the first two plots (left to right) are the measured and modeled power profiles, the third one is the difference between data and model weighted by their standard deviation, and the last one is the discrete gradient of T_e/T_i profile weighted by the regularization parameter.

and modeled power profiles, the third one is the difference between data and model weighted by their uncertainties, and the last one is the regularization term. We are judging the quality of our fitting results following the *goodness-of-fit* criterion, which states that good estimates are obtained when the data-term normalized by the degrees of freedom of the data, i.e., the number of data points minus the number of estimating parameters, is around unity. Much larger or smaller values may imply a poor knowledge of σ_p and/or an inappropriate data model. In our estimations, we found values for the normalized data-term typically between 0.9 and 1.1, giving us confidence about the quality of our results.

CHAPTER 5

ELECTRON DENSITY AND T_e/T_i ESTIMATES

Using the IS radar equation and inversion procedure described in previous chapters, F-region densities and T_e/T_i estimates were obtained using the power data collected by ALTAIR. These results have shown to be in near perfect agreement with simultaneous density measurements performed by Roi-Namur ionosonde system. The comparison validates the technique. In addition, under the assumption of equal electron and ion temperatures (i.e., $T_e = T_i$), high-resolution density maps of the E-region ionosphere were also computed as function of height and distance from the radar. These data constitute the first low-latitude D- and E-region incoherent scatter measurements conducted at ALTAIR since 1979 [*Tsunoda*, 1995]. Interesting features of these measurements are discussed throughout the chapter.

5.1 *F*-Region Results

Figure 5.1 presents N_e and T_e/T_i maps for September 20, 2004, constructed from profile estimates obtained with the data model and inversion technique described in this thesis. The density map shows a typical low-latitude F-region ionosphere exhibiting a characteristic rise during the morning hours. Also, T_e/T_i is elevated above unity mainly between 200 and 300 km as expected in daytime measurements.

In order to validate our results, we performed comparisons with electron density profiles obtained with the Roi-Namur ionosonde system. As shown in Figure 5.2, the agreement between fitted-ISR and ionosonde estimates is excellent, specifically

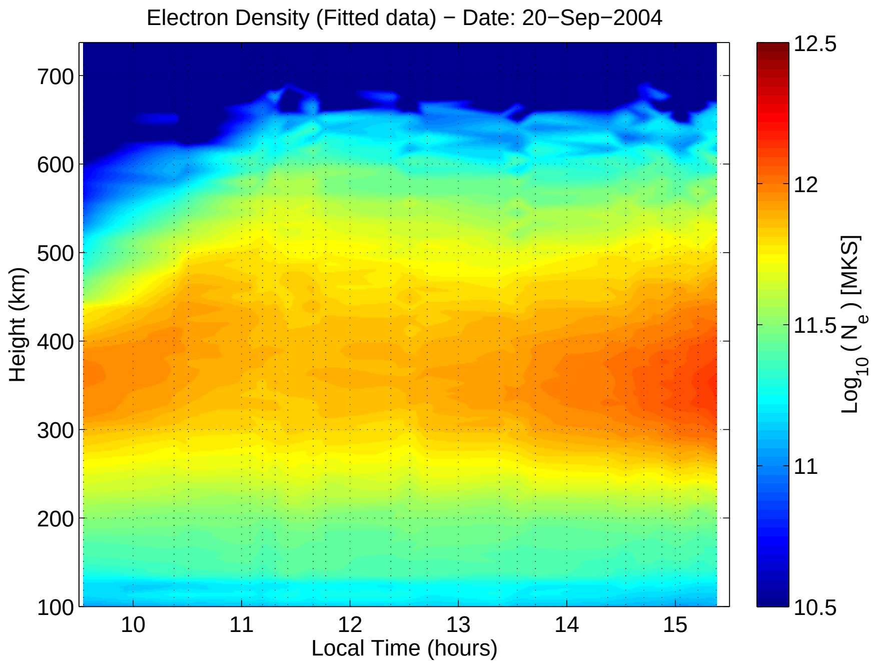

(a)

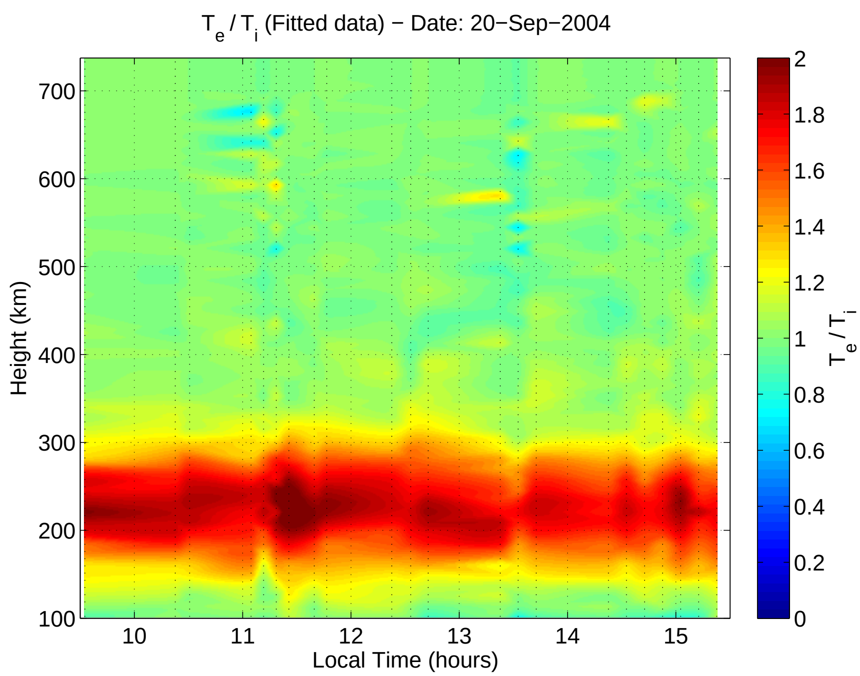

(b)

Figure 5.1 (a) Electron density and (b) T_e/T_i estimates of the F-region ionosphere inverted from ALTAIR radar scans collected on September 20, 2004.

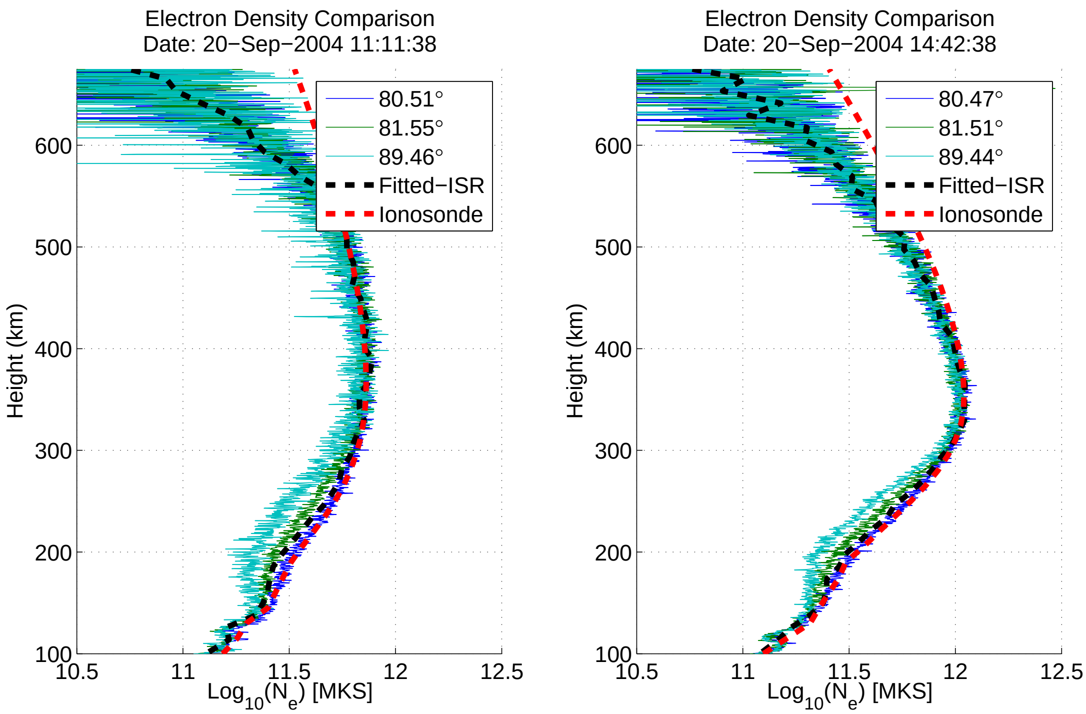

(a) (b)

Figure 5.2 Electron density comparison between fitted-ISR and ionosonde measurements corresponding to the time (a) before and (b) after midday on September 20, 2004. Density-like profiles are also plotted and were calculated by scaling the power data collected at directions around $\alpha = 0°$ and assuming $\eta = \frac{1}{2}$ as if the ionosphere were in thermal equilibrium.

at the peak and bottom-side of the F-region. The agreement at the peak effectively verifies the correctness of the ALTAIR calibration constant K_s, whereas the agreement in the bottom-side verifies the forward model underlying the data inversion given that the values and altitudes of enhanced T_e/T_i are plausible in view of our understanding of the physics of the region. This was also verified by the good comparison of our results with temperature values obtained from the International Reference Ionosphere (IRI) model [*Bilitza*, 2001].

In Figure 5.2, we are also comparing our fitted results with a set of power profiles from the vicinity of $\alpha = 0°$. They have been scaled into equivalent density profiles by proper K_s and assuming $\eta = \frac{1}{2}$ as if the ionosphere were in thermal equilibrium.

Somewhat surprisingly, we note that the profile corresponding to the scan angle closest to $\alpha = 0°$ (about 80.5° elevation) agrees very well with the fitted-ISR and ionosonde profiles. This may be the smooth result of having a moving beam with a finite width that averages the scattering contributions from different aspect angles around perpendicular to $\vec{B}$. Finally, note that the effect of $T_e/T_i > 1$ disappears at altitudes below 130 km, where density estimates can be obtained at all elevation angles assuming $\eta = \frac{1}{2}$. This is the assumption made in the calculation of E-region electron density maps that will be presented in the next section.

The technique described in previous chapters requires only a few scan directions across magnetic perpendicularity in order to obtain unbiased N_e and T_e/T_i estimates with a calibrated IS radar operating in the UHF band. The time resolution of the profile estimates can be improved by restricting the overall scan angle to a few degrees (2° or 3°) centered about $\alpha = 0°$ and increasing the frequency of the scans. This procedure can also be applied with IS radars in VHF range provided that ionospheric depolarization effects, more important at VHF, are taken into account in a proper manner [*Kudeki et al.*, 2003].

5.2 *E*-Region Results

Figure 5.3(a)-(d) present E-region electron density data collected during four different UHF ALTAIR scans corresponding to different days. In each panel the vertical axis is geodetic altitude and the horizontal axis represents ground distance away from ALTAIR (in approximately northward direction). Panel (a) shows densities measured on September 20, 2004, that were conducted for comparison with rocket measurements carried out the same day [*Friedrich et al.*, 2006]. In addition, the projection of the rocket flight trajectory onto the radar scan plane is depicted by a black line. The lateral displacement of the trajectory from the scan plane was

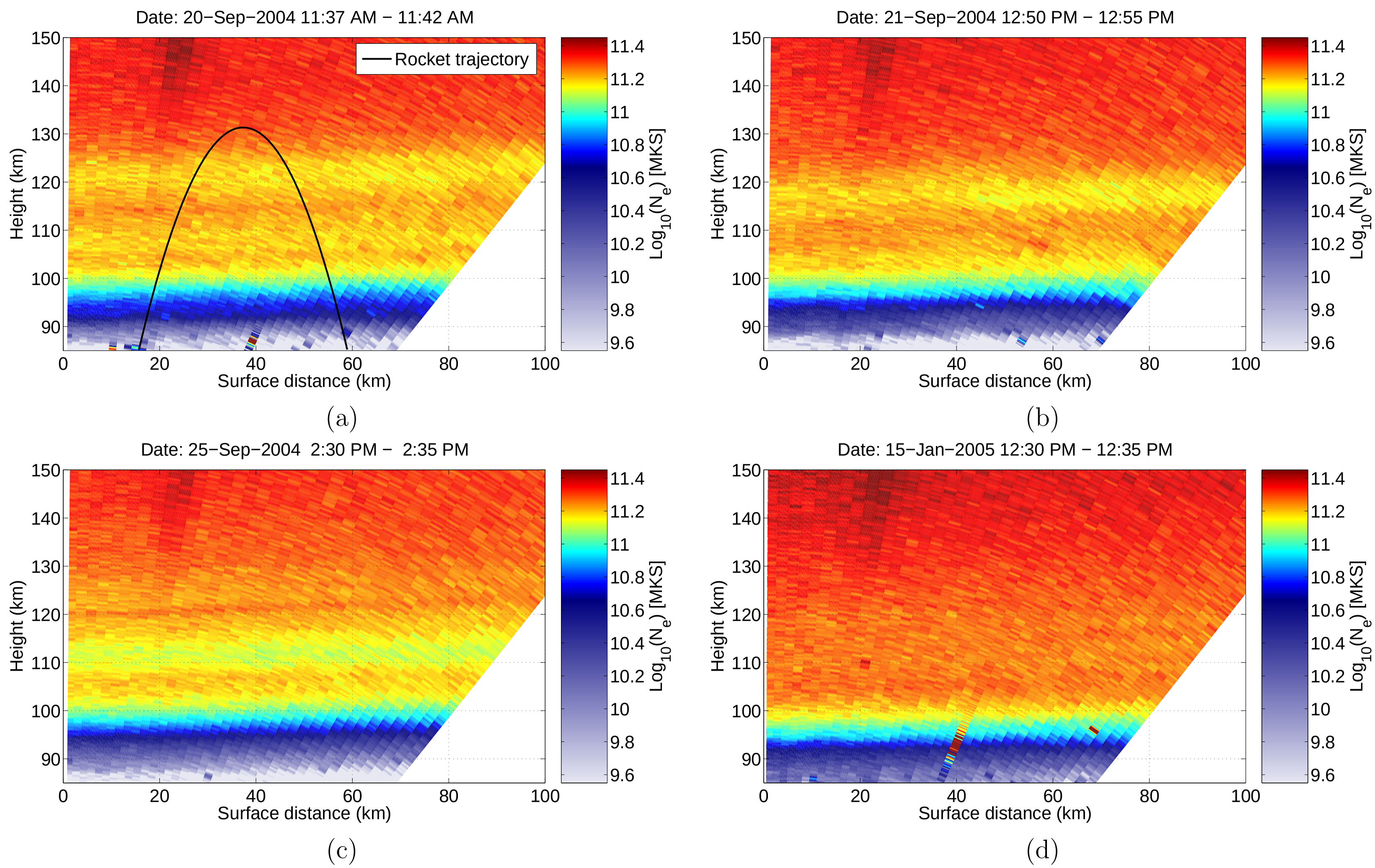

Figure 5.3 E-region electron density estimates as function of altitude and ground distance from ALTAIR. Each plot corresponds to one example scan taken on September 20, 21, and 25, 2004, and January 15, 2005.

less than 3 km throughout the upleg portion of the flight. Panels (b) and (c) show ALTAIR scan data from September 21 and 25, respectively, whereas panel (d) is from January 15, 2005.

Note that all the panels in Figure 5.3 exhibit a T_e/T_i related enhancement (like in Figure 2.1) at around 20 km ground distance down to an altitude of about 130 km. The enhancement, however, is not visible at lower altitudes, indicating that over the altitudes where rocket and ALTAIR comparisons were carried out, the condition $T_e = T_i$ was well satisfied; ALTAIR density profiles below 130 km are not expected to have distortions due to altitude variations of background parameters such as temperature, collision frequency, and geomagnetic field.

Panels (a)-(c) in Figure 5.3—but not panel (d)—exhibit meridionally extended E-region structures above 100 km. The temporal variation of the structures for September 20, 2004, can be examined in Figure 5.4, which is a montage of ALTAIR density measurements for a constant latitude of 10° N (about 70 km north of ALTAIR). The montage combines and interpolates data from 22 scans taken on September 20 at times indicated by the dashed vertical lines shown in the figure. The descending temporal signature in Figure 5.4, as well as horizontal coherence scales in excess of 100 km inferred from Figure 5.3(a)-(c), suggest a tidal origin for the observed structures. Note that Figure 5.3(a) shows localized density minima at about 105 and 120 km altitudes, whereas Figure 5.3(b) and (c) from later local times (on different days) exhibit a single density minimum at about 115 and 110 km, respectively, in general agreement with the temporal signature observed on September 20. In Figure 5.4 we see at earlier local times a pair of density minima consistent with Figure 5.3(a), but a single descending minimum in the afternoon consistent with Figure 5.3(b) and (c). Overall, the information contained in Figures 5.3 and 5.4 imply a tidal-driven dynamics with some degree of day-to-day regularity for upper E-region altitudes in September 2004 time period. There is no indication

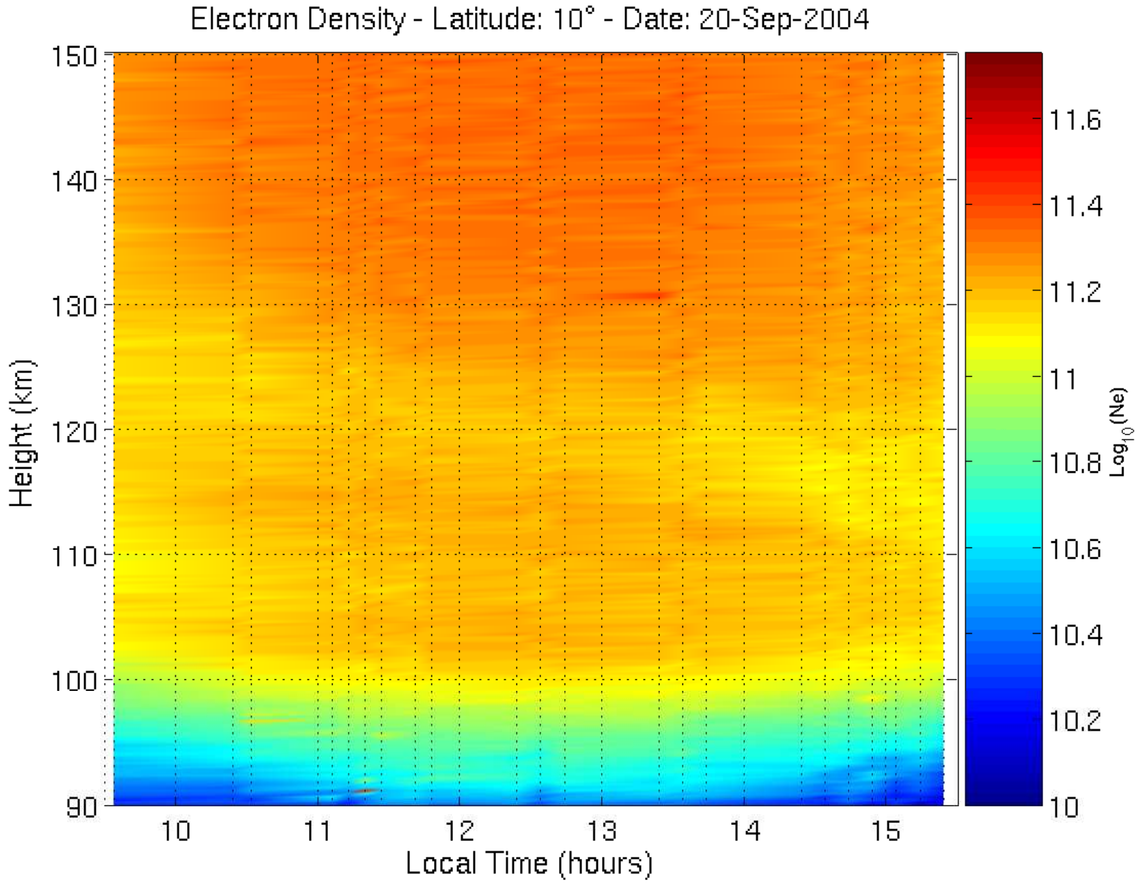

Figure 5.4 E-region electron density profiles measured at a constant latitude 10° N from September 20, 2004.

of a similarly strong tidal effect in the measurements of January 2005.

Another feature from Figure 5.3 is the hint of a thin density layer in panel (c) centered about 120 km altitude. Figure 5.5 presents a collection of individual density profiles taken from the same panel. Clearly, the layer in question has a half width of about one km, which is smaller than the vertical scale of tidal variations discussed above. However, the horizontal extent of the layer is substantial ($\sim$ 80 km or longer), and the layer was observed to develop and then weaken over a time scale of about an hour without a significant variation of its altitude. A weaker thin layer with a smaller horizontal extent can also be observed in Figure 5.3(a) at around 114 km altitude. The latter was detected by the rocket probes and is discussed by

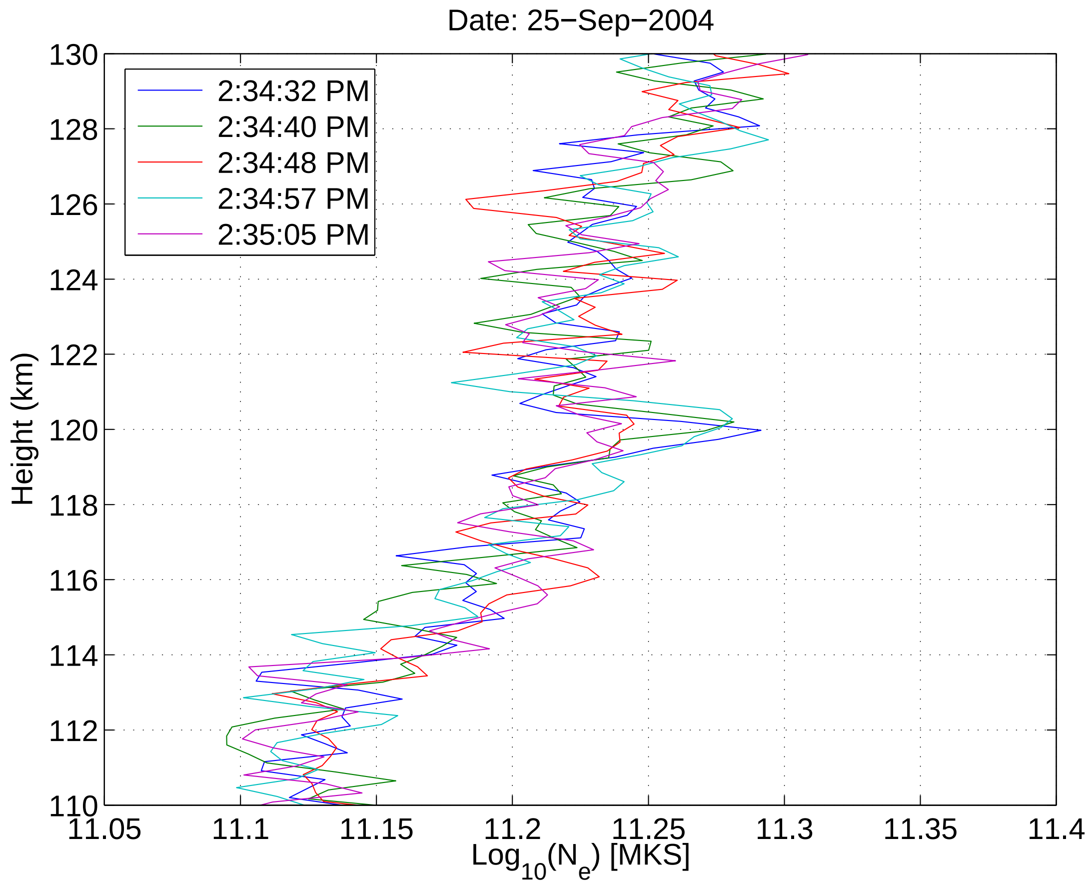

Figure 5.5 *E*-region electron density profiles from September 25, 2004, exhibiting a thin layer at about 120 km height.

Friedrich et al. [2006].

The absence of tidal structures in Figure 5.3(d) from January 15, 2005, may be a consequence of seasonal variability in tidal dynamics in the region. However, the UHF ALTAIR scans taken on January 15, 2005, coincided with a period of enhanced X-ray fluxes. The bottom panel of Figure 5.6 shows a 10-15 dB increase of the solar X-ray flux between 12.65 to 12.70 LT, which clearly causes the abrupt electron density changes in the *E*-region shown in top two panels of the same figure. The top panel displays density profiles taken in different scans, with the blue profile representing the *E*-region densities just before the X-ray flare, and the green profile the data collected in that scan which immediately followed the flare. There is

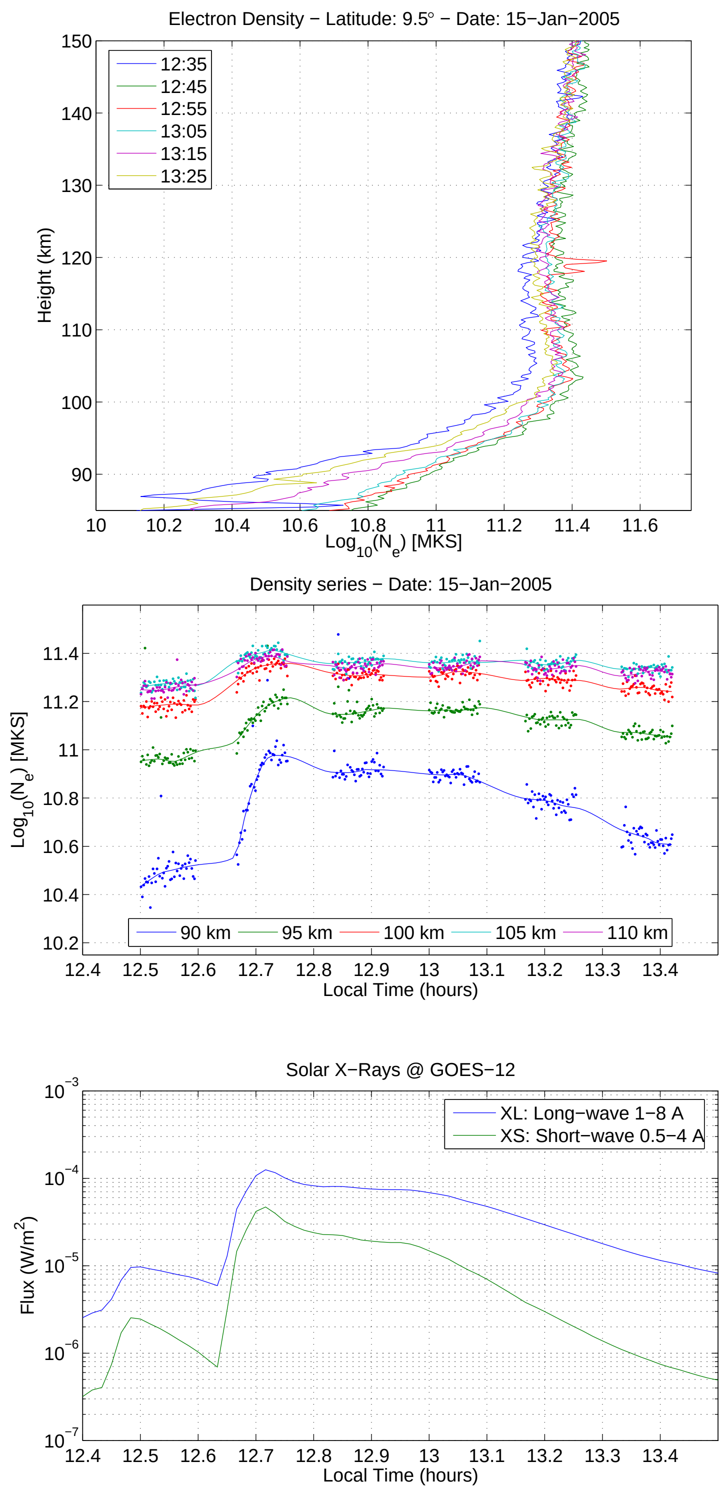

Figure 5.6 E-region electron density data measured on January 15, 2005, during an X-ray flare event depicted by the flux data shown on the bottom panel.

a substantial jump in the densities, particularly at lower altitudes below 100 km, followed by a gradual relaxation as the X-ray flux returns to lower levels over the next half hour. *E*-region density response to the flare is displayed even more clearly in the middle panel, where different colors correspond to ALTAIR density data taken from different altitudes (during each of the six scans represented in the top panel). The electron densities increase at all *E*-region altitudes in response to the flare, but the change is most dramatic at lower altitudes closer to *D*-region, consistent with earlier studies of *D*-region response to X-rays [*Rastogi et al.*, 1988]. A detailed quantitative study of the flare results may require inversion efforts where the forward model includes the finite Debye length effects ignored in our present analysis.

CHAPTER 6

DISCUSSION AND CONCLUSIONS

In this thesis, we have reported on the estimation of ionospheric state parameters N_e and T_e/T_i from IS power data collected with the ALTAIR radar. The data corresponds to meridional scans of the low-latidude E- and F-region ionosphere that included a radar viewing direction perpendicular to the geomagnetic field. As the radar beam went through this orientation, an increment of the received power was detected; this is a typical feature of the incoherent scatter process at small magnetic aspect angles. Our goal was to exploit this characteristic of the IS signal power to estimate meaningful ionospheric parameters.

For this purpose, the power data was modeled using a soft-target radar equation that accounts for the effects of radar ambiguity function and antenna pattern (see Chapter 3). Furthermore, the physics of the incoherent scatter process was considered in terms of the total RCS of the medium that is proportional to the efficiency factor of electron scattering η. Because our data analysis involved measurements at small magnetic aspect angles, the formulation of η should include the effects of electron-ion Coulomb collisions that are important in this regime [*Sulzer and González*, 1999]. In order to account for these effects, we have used the collisional IS spectral model of *Woodman* [1967] together with an empirical collision frequency formula proposed by *Woodman* [2004]. This procedure has been justified by the arguments given in *Kudeki and Milla* [2006]. By numerical integration of the proposed IS spectrum, a table of η values was built for a given set of ionospheric parameters.

Physically meaningful results obtained with ALTAIR data effectively verified the soft-target radar equation used in the inversion technique. However, the test on the collisional spectral model and collision frequency formula turned out to be weak. Based on our calculations, we found that the efficiency factor was not very sensitive to the actual value of collision frequency ν_e. In fact, increasing ν_e by a factor of three or decreasing it by a factor of ten produced deviations of η smaller than 1%. Therefore, more stringent tests to this collisional model should be conducted using IS spectral data taken for small magnetic aspect angles with steerable radar systems such as ALTAIR.

Additionally, our measurements have proved to be in good agreement with digisonde estimates performed also at ALTAIR, specifically below the F-region peak. Note that without taking into account the T_e/T_i effect, density measurements could be underestimated by at most a factor of two. Finally, the regularization technique used in our inversions has shown to be successful in providing smooth results and reducing the noise in our estimated profiles. The success is mainly because of the appropriate choice of the regularization parameter obtained with the L-curve method.

APPENDIX A

SOFT-TARGET RADAR EQUATION

In soft-target radar applications, the backscattered signal voltage detected by a radar antenna corresponds to the signal scattered from variations in the refractive index of the probed medium. In the case of an ionospheric plasma, such variations are the consequence of fluctuations in the distribution of plasma density. Although instantaneous values of these fluctuations are unpredictable, their statistical behavior is formulated by the theory of incoherent scatter. In this appendix, we will derive the radar equation presented in Chapter 3 to model the average power collected by a radar system.

A.1 Derivation of the Radar Equation

The scattered field detected by a radar antenna produces an open-circuit voltage phasor that can be formulated as

$$V_a(t) = \int d\vec{r}\, W(\vec{r},t)\, n_e(\vec{r}, t - \frac{r}{c})\, e^{-j2k_o r}. \tag{A.1}$$

This represents the linear and causal response of density fluctuations $n_e(\vec{r}, t)$ excited by a radio signal with wavenumber k_o and propagation velocity c. The effects of antenna gain $G(\hat{r})$ and transmitted pulse envelope $f(t)$ are considered in the system

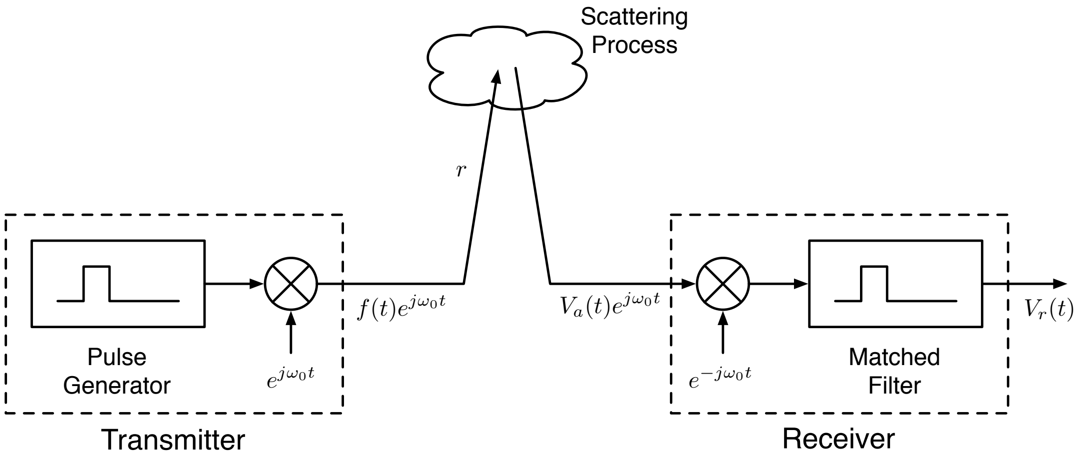

Figure A.1 Typical radar configuration.

weighting factor [*Kudeki*, 2006]

$$W(\vec{r},t) \equiv -j\, I_o\, R_{rad}\, \frac{r_e}{k_o}\, f(t-\frac{2r}{c})\, \frac{G(\hat{r})}{r^2}. \tag{A.2}$$

In this expression, I_o is the peak of the antenna current distribution, R_{rad} is the antenna radiation resistance, and r_e is the classical electron radius.

As shown in Figure A.1, the voltage $V_r(t)$, detected at the receiver output, is the convolution of receiver impulse response $h(t)$ and antenna voltage $V_a(t)$. Therefore, we can write that

$$\begin{aligned} V_r(t) = h(t) * V_a(t) &= h(t) * \int d\vec{r}\, W(\vec{r},t)\, n_e(\vec{r}, t-\frac{r}{c})\, e^{-j2k_o r} \\ &= \int d\vec{r} \int d\tau\, W(\vec{r},\tau)\, n_e(\vec{r},\tau-\frac{r}{c})\, h(t-\tau)\, e^{-j2k_o r}. \end{aligned} \tag{A.3}$$

In radar applications, matched-filter detection is extensively used. This case will be analyzed in the next section.

The squared modulus of receiver voltage (A.3) is expressed as

$$
\begin{aligned}
|V_r(t)|^2 = V_r^*(t)\, V_r(t) \;&=\; \int d\vec{r} \int d\tau\, W^*(\vec{r},\tau)\, n_e^*(\vec{r},\tau - \frac{r}{c})\, h^*(t-\tau)\, e^{j2k_o r} \\
&\quad \int d\vec{r}\,' \int d\tau'\, W(\vec{r}\,',\tau')\, n_e(\vec{r}\,',\tau' - \frac{r'}{c})\, h(t-\tau')\, e^{-j2k_o r'}
\end{aligned}
$$

$$
\begin{aligned}
&= \int d\vec{r} \int d\vec{r}\,' \int d\tau \int d\tau'\, W^*(\vec{r},\tau)\, W(\vec{r}\,',\tau')\, h^*(t-\tau)\, h(t-\tau') \\
&\quad n_e^*(\vec{r},\tau - \frac{r}{c})\, n_e(\vec{r}\,',\tau' - \frac{r'}{c})\, e^{-j2k_o(r'-r)}.
\end{aligned} \tag{A.4}
$$

Taking the expected value of both sides, we obtain

$$
\begin{aligned}
\langle |V_r(t)|^2 \rangle \;&=\; \int d\vec{r} \int d\vec{r}\,' \int d\tau \int d\tau'\, W^*(\vec{r},\tau)\, W(\vec{r}\,',\tau')\, h^*(t-\tau)\, h(t-\tau') \\
&\quad \langle n_e^*(\vec{r},\tau - \frac{r}{c})\, n_e(\vec{r}\,',\tau' - \frac{r'}{c}) \rangle\, e^{-j2k_o(r'-r)}.
\end{aligned} \tag{A.5}
$$

We know that the parameters governing the ionospheric plasma dynamics vary slowly in time and space. Indeed, it can be observed that they remain about the same during many radar pulse repetition periods. If the fluctuations $n_e(\vec{r},t)$ have homogeneous and stationary statistics, its space-time correlation will have the form

$$
\langle n_e^*(\vec{r},\tau - \frac{r}{c})\, n_e(\vec{r}\,',\tau' - \frac{r'}{c}) \rangle = R_n(\vec{r}\,' - \vec{r}, \tau' - \tau - \frac{r'-r}{c}; \vec{r}), \tag{A.6}
$$

where function R_n depends only on differences in space and time coordinates.

In addition, it can be verified that correlation R_n is very narrow in space having significant values only for small distances $\vec{r}\,' - \vec{r}$ with respect to $\vec{r}$. Applying the change of variables $\vec{x} = \vec{r}\,' - \vec{r}$ and using the approximation $r' - r \approx \vec{x} \cdot \hat{r}$ for small values of $\vec{x}$, we can obtain that

$$W^*(\vec{r},\tau)\,W(\vec{r}+\vec{x},\tau') \approx \frac{|I_o|^2\,R_{rad}^2\,r_e^2}{k_o^2}\,f^*(\tau-\frac{2r}{c})\,f(\tau'-\frac{2r}{c})\,\frac{G^2(\hat{r})}{r^4}, \tag{A.7}$$

and then rewrite the variance (A.5) as

$$\begin{aligned}\langle|V_r(t)|^2\rangle \;\approx\; & \frac{|I_o|^2\,R_{rad}^2\,r_e^2}{k_o^2}\int d\vec{r}\,\frac{G^2(\hat{r})}{r^4}\int d\tau\int d\tau'\int d\vec{x}\,R_n(\vec{x},\tau'-\tau;\vec{r})\,e^{-j2k_o\hat{r}\cdot\vec{x}} \\ & f^*(\tau-\frac{2r}{c})\,f(\tau'-\frac{2r}{c})\,h^*(t-\tau)\,h(t-\tau'). \end{aligned}\tag{A.8}$$

Note that the approximation $\frac{\vec{x}\cdot\hat{r}}{c}\to 0$ is used to simplify the expression.

Let us define the space-time power spectral density (PSD) of density fluctuations $n_e(\vec{r},t)$ as

$$\Phi_n(\vec{k},\omega;\vec{r}) \equiv \int dt\int d\vec{x}\,R_n(\vec{x},t;\vec{r})\,e^{j\vec{k}\cdot\vec{x}-j\omega t}. \tag{A.9}$$

Using this definition, we can rewrite the variance of $V_r(t)$ as

$$\begin{aligned}\langle|V_r(t)|^2\rangle \;\approx\; & \frac{|I_o|^2\,R_{rad}^2\,r_e^2}{k_o^2}\int d\vec{r}\,\frac{G^2(\hat{r})}{r^4}\int d\tau\int d\tau'\int\frac{d\omega}{2\pi}\,\Phi_n(-2k_o\hat{r},\omega;\vec{r})\,e^{j\omega(\tau'-\tau)} \\ & f^*(\tau-\frac{2r}{c})\,f(\tau'-\frac{2r}{c})\,h^*(t-\tau)\,h(t-\tau') \\ = \; & \frac{|I_o|^2\,R_{rad}^2\,r_e^2}{k_o^2}\int d\vec{r}\,\frac{G^2(\hat{r})}{r^4}\int\frac{d\omega}{2\pi}\,\Phi_n(-2k_o\hat{r},\omega;\vec{r}) \\ & (\int d\tau\,f(\tau-\frac{2r}{c})\,h(t-\tau)\,e^{j\omega\tau})^*\int d\tau'\,f(\tau'-\frac{2r}{c})\,h(t-\tau')\,e^{j\omega\tau'} \\ = \; & \frac{|I_o|^2\,R_{rad}^2\,r_e^2}{k_o^2}\int d\vec{r}\,\frac{G^2(\hat{r})}{r^4}\int\frac{d\omega}{2\pi}\,\Phi_n(-2k_o\hat{r},\omega;\vec{r}) \\ & |\int d\tau\,f(\tau)\,h((t-\frac{2r}{c})-\tau)\,e^{j\omega\tau}|^2. \end{aligned}\tag{A.10}$$

Finally, combining the fact that $d\vec{r} = r^2\,dr\,d\Omega$ together with the definition of effective antenna area $A_e(\hat{r}) \equiv \frac{\lambda_o^2}{4\pi} G(\hat{r})$, we obtain

$$P_r(t) \approx \int dr\, d\Omega\, r^2 \underbrace{\frac{A_e(\hat{r})}{r^2}}_{\substack{\text{Solid}\\ \text{angle}}} \underbrace{\frac{P_t\, G(\hat{r})}{4\pi r^2}}_{\substack{\text{Incident}\\ \text{flux}}} \int \frac{d\omega}{2\pi} \underbrace{r_e^2\, \Phi_n(-2k_o\hat{r}, \omega; \vec{r})}_{\substack{\text{Cross section}\\ \text{per unit volume,}\\ \text{solid angle,}\\ \text{and frequency}}} |\chi_{fh}(t - \frac{2r}{c}, \omega)|^2, \tag{A.11}$$

where $P_r(t) \equiv \frac{\langle |V_r(t)|^2 \rangle}{8R_{rad}}$ is the expected available power at the receiver output and $P_t \equiv \frac{1}{2}|I_o|^2 R_{rad}$ is the average peak power of the transmitted pulse. We define the cross ambiguity function as [*Blahut*, 2004]

$$\chi_{fh}(\tau, \omega) \equiv \int dt\, f(t)\, h(\tau - t)\, e^{j\omega t}. \tag{A.12}$$

This two-dimensional system function accounts for the effects of pulse envelope $f(t)$ and filter impulse response $h(t)$. In addition, we define

$$\sigma_n(\vec{k}, \omega; \vec{r}) \equiv 4\pi\, r_e^2\, \Phi_n(\vec{k}, \omega; \vec{r}), \tag{A.13}$$

as the volumetric radar cross section (RCS) spectrum of the medium. Thus, we can interpret the expected received power (A.11) as the result of filtering and integrating σ_n over frequency, incident flux, solid angle and radar range.

A.2 Matched-Filter and Ambiguity Function

As we have already mentioned, matched-filters are extensively used in radar applications in order to maximize the SNR of the received signal. Taking the impulse response of a matched-filter as

$$h(t) \equiv \frac{1}{T} f^*(-t), \tag{A.14}$$

where $f(t)$ is the envelope of the transmitted pulse and T denotes its duration, we can define the ambiguity function of $f(t)$ as

$$\chi(\tau,\omega) \equiv \frac{1}{T}\int dt\, f(t)\, f^*(t-\tau)\, e^{j\omega t}, \tag{A.15}$$

and rewrite our expression for the received power as

$$P_r(t) \approx E_t\, K_s \int dr\, d\Omega\, \frac{g^2(\hat{r})}{r^2} \int \frac{d\omega}{2\pi}\, \sigma_n(-2k_o\hat{r},\omega;\vec{r})\, |\chi(t-\frac{2r}{c},\omega)|^2. \tag{A.16}$$

Above, $E_t \equiv P_t T$ is the total energy of the transmitted pulse and $g(\hat{r})$ is the normalized antenna gain. The system calibration constant

$$K_s \equiv \frac{1}{T}\frac{D^2}{16\pi k_o^2 L} \tag{A.17}$$

accounts for system losses L, antenna directivity D, and transmitted pulse duration T. This completes the derivation of the soft-target radar equation presented in Chapter 3 as a forward model for the power data collected by a radar system.

Note that the expected received power (A.16) is the sum of the RCS function weighted in frequency and range by the ambiguity function. The width in range of $\chi(\tau,\omega)$ determines the range resolution of the measurements, while its width in frequency domain filters the volumetric RCS spectrum σ_n. How the ambiguity function affects radar measurements depends directly on the shape of the envelope of the transmitted pulse.

APPENDIX B

AMBIGUITY FUNCTION OF BASIC FUNCTIONS

B.1 Ambiguity Function of a Rectangular Pulse

Let us define the rectangular pulse envelope $f(t) = \mathrm{rect}(t/T)$, where T denotes its duration. Using the definition of ambiguity function (A.15), we can write

$$\chi(\tau,\omega) = \begin{cases} \frac{1}{T}\int_{-T/2+\tau}^{T/2} e^{j\omega t}dt, & 0 \leq \tau \leq T \\ \frac{1}{T}\int_{-T/2}^{T/2+\tau} e^{j\omega t}dt, & -T \leq \tau < 0. \end{cases} \tag{B.1}$$

Evaluating the integrals, we have that

$$\chi(\tau,\omega) = \begin{cases} e^{j\omega\tau/2}\frac{\sin(\omega T(1-\tau/T)/2)}{\omega T/2}, & 0 \leq \tau \leq T \\ e^{j\omega\tau/2}\frac{\sin(\omega T(1+\tau/T)/2)}{\omega T/2}, & -T \leq \tau < 0. \end{cases} \tag{B.2}$$

Finally, taking the absolute value of $\chi(\tau,\omega)$ and squaring it, we obtain

$$|\chi(\tau,\omega)|^2 = \left|\left(1 - \frac{|\tau|}{T}\right)\mathrm{sinc}(\omega T(1-|\tau|/T)/2)\right|^2 \tag{B.3}$$

for $|\tau| \leq T$ and zero outside.

As we can appreciate in Figure B.1, the ambiguity function of a rectangular pulse acts as a low pass filter over the frequency response of the medium at different ranges r, being its approximate bandwidth $1/2T$. On the other hand, using the Rayleigh criterion[1] for range resolution, we can find that this resolution is $cT/2$,

[1]In this context, Rayleigh resolution can be defined as the first zero-crossing of the ambiguity

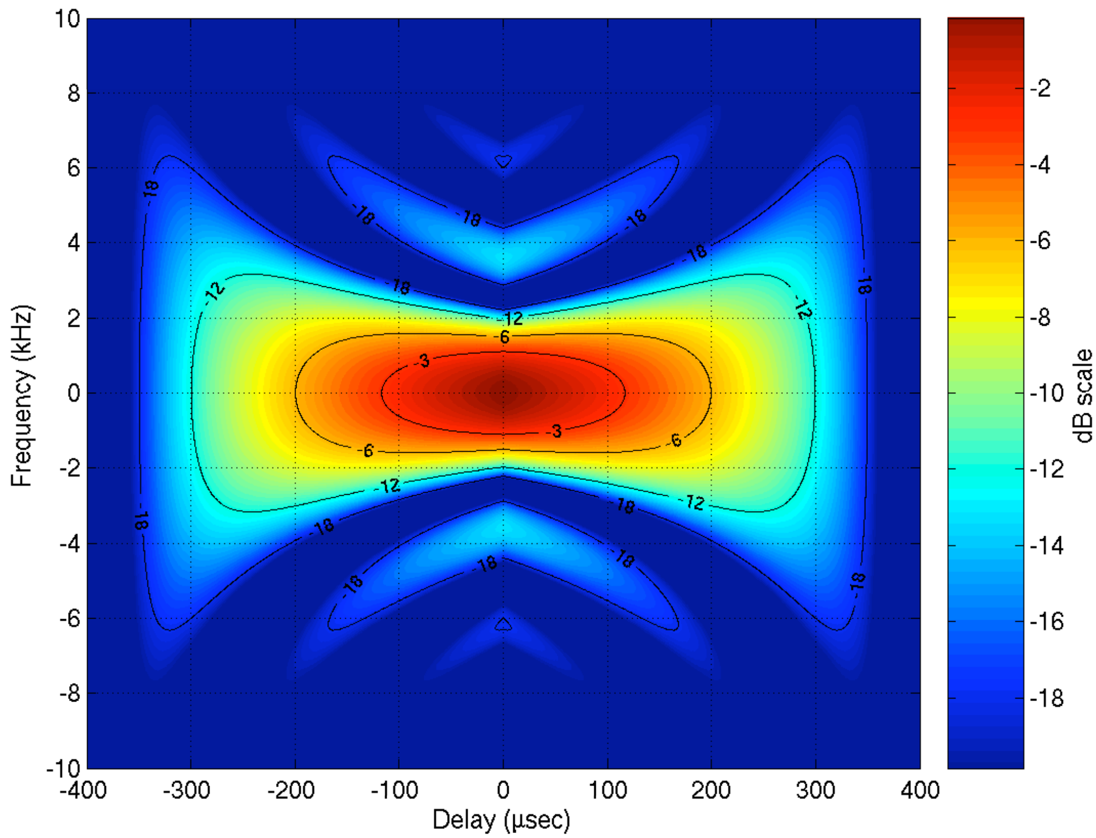

Figure B.1 Ambiguity function of a rectangular pulse with duration $T = 400\,\mu$s ($\Delta r = 60\,$km).

where c is the speed of light.

For example, if we use a $400\,\mu$s rectangular pulse, the effective bandwidth of the received signal will be about 1.25 kHz and its resolution $\Delta r = 60\,$km. It can be observed that for ionospheric radar applications operating at frequencies around 400 MHz (e.g., ALTAIR, Arecibo), the typical bandwidth of the medium response is about 10 kHz (for large magnetic aspect angles). Therefore, if we had used the pulse of our example in a real measurement, most of the frequency components of the medium response would have been filtered out by the ambiguity function.

Since the use of long pulses in ionospheric radar applications is necessary due to the intrinsic weakness of the medium response, some techniques have been devel-

function evaluated at zero frequency.

oped that improve the bandwidth of the ambiguity function and at the same time reduce the range resolution of the measurements. Among them, binary or phase coded pulses are commonly used, and a discussion about them can be found in the literature, e.g., *Levanon* [1988].

B.2 Ambiguity Function of a Chirped Pulse

A chirped pulse combines the flat amplitude modulation of a rectangular pulse with a linear frequency modulation. As we will examine, it improves the range resolution and expands the bandwidth of its ambiguity function.

The complex envelope of a chirped pulse is given by $f(t) = \mathrm{rect}(t/T)\, e^{j\frac{\beta}{2}t^2}$, where T is the duration of the pulse, $\beta = \frac{2\pi\Delta f}{T}$ is the frequency rate, and Δf is the frequency span of the chirped. Using $f(t)$ in the definition of ambiguity function, we can write

$$\chi(\tau,\omega) = \begin{cases} \frac{1}{T}\int_{-T/2+\tau}^{T/2} e^{j\frac{\beta}{2}(t^2-(t-\tau)^2)} e^{j\omega t} dt, & 0 \le \tau \le T \\ \frac{1}{T}\int_{-T/2}^{T/2+\tau} e^{j\frac{\beta}{2}(t^2-(t-\tau)^2)} e^{j\omega t} dt, & -T \le \tau < 0. \end{cases} \tag{B.4}$$

A change of variables leads to

$$\chi(\tau,\omega) = \begin{cases} \frac{1}{T} e^{j\omega\tau/2} \int_{-(T-\tau)/2}^{(T-\tau)/2} e^{j(\beta\tau+\omega)t} dt, & 0 \le \tau \le T \\ \frac{1}{T} e^{j\omega\tau/2} \int_{-(T+\tau)/2}^{(T+\tau)/2} e^{j(\beta\tau+\omega)t} dt, & -T \le \tau < 0. \end{cases} \tag{B.5}$$

Evaluating the integrals, we have that

$$\chi(\tau,\omega) = \begin{cases} e^{j\omega\tau/2} \frac{\sin(T(1-\tau/T)(\omega+\beta\tau)/2)}{T(\omega+\beta\tau)/2}, & 0 \le \tau \le T \\ e^{j\omega\tau/2} \frac{\sin(T(1+\tau/T)(\omega+\beta\tau)/2)}{T(\omega+\beta\tau)/2}, & -T \le \tau < 0. \end{cases} \tag{B.6}$$

Thus, taking the absolute value and squaring $\chi(\tau,\omega)$, we obtain

$$|\chi(\tau,\omega)|^2 = \left|\left(1-\frac{|\tau|}{T}\right)\mathrm{sinc}(T(1-|\tau|/T)(\omega+\beta\tau)/2)\right|^2 \tag{B.7}$$

for $|\tau| \leq T$ and zero outside.

First, we can notice that the ambiguity function of a chirped pulse reduces to the case of a rectangular pulse when $\beta = 0$, then as β increases the distortion with respect to the rectangular pulse case becomes more clear. In particular, for big values of β (i.e., big frequency span Δf), the ambiguity function will look like Figure 3.1, and can be interpreted as a continuous bank of narrow filters whose bandwidths are approximately $1/2T$ (as in the case of a rectangular pulse), but whose amplitudes and central frequencies vary linearly with range. By integrating all these contributions, the reception bandwidth is effectively increased up to half the frequency span of the chirped pulse.

In the case of high β and following the Rayleigh criterion, we can find that the range resolution of a chirped pulse is $c/2\Delta f$. This is a valid result for narrow band signals (lower than $1/2T$); however, for higher bandwidths, we have to use a different criterion to define the range resolution. Following the linear relation between frequency and delay $\omega + \beta\tau = 0$ that comes from the ambiguity function formula, we can determine the range resolution using $\Delta r = \frac{B_s}{\Delta f}\frac{cT}{2}$, where B_s denotes the bandwidth of the signal in Hz.

For example, if we considered a medium response of 10 kHz bandwidth, and used a chirped pulse of 400 μs length and 250 kHz of frequency span, it would be observed that the ambiguity function of this pulse would preserve all the frequency components of the medium response, and that the spatial resolution of the measurements would be about 2.4 km (16 μs).

Since the ambiguity function is an issue in the configuration of radar applications, the main goal in the design of radar pulses is to obtain a flat frequency response in the band of interest with the "minor" compromise in range resolution.

APPENDIX C

INVERSION RESULTS CATALOG OF ALTAIR SCANS

Electron density estimates inverted from ALTAIR scans are presented in this appendix. The scans were taken during the Equis 2 NASA campaign on September 20, 21, and 25, 2004. In addition, "control" data was also collected on January 15, 2005. A total of 45 scans were analyzed and the results are displayed independently for both F- and E-regions.

F-region density estimates are presented in Figures C.1 - C.45. In each figure, panel (a) displays the scan data calibrated to equivalent electron density values. These "densitites" are biased by the effect of unequal temperatures (i.e., $T_e/T_i > 1$). The unbiased densities, obtained after applying the inversion technique, are shown in panel (b). In general, the results are smooth except at altitudes corresponding to the topside F-region because of poor SNR.

E-region density maps are presented in Figures C.46 - C.90. They were obtained after calibration of the scan data using the assumption of equal temperatures (i.e., $T_e = T_i$). Densities are plotted as function of height and ground distance from ALTAIR. In most of the plots, the effect of $T_e > T_i$ (an apparent increment in density) is appreciable at altitudes above 130 km and a distance around 20 km. At lower altitudes, there is no effect verifying our assumption of equal temperatures.

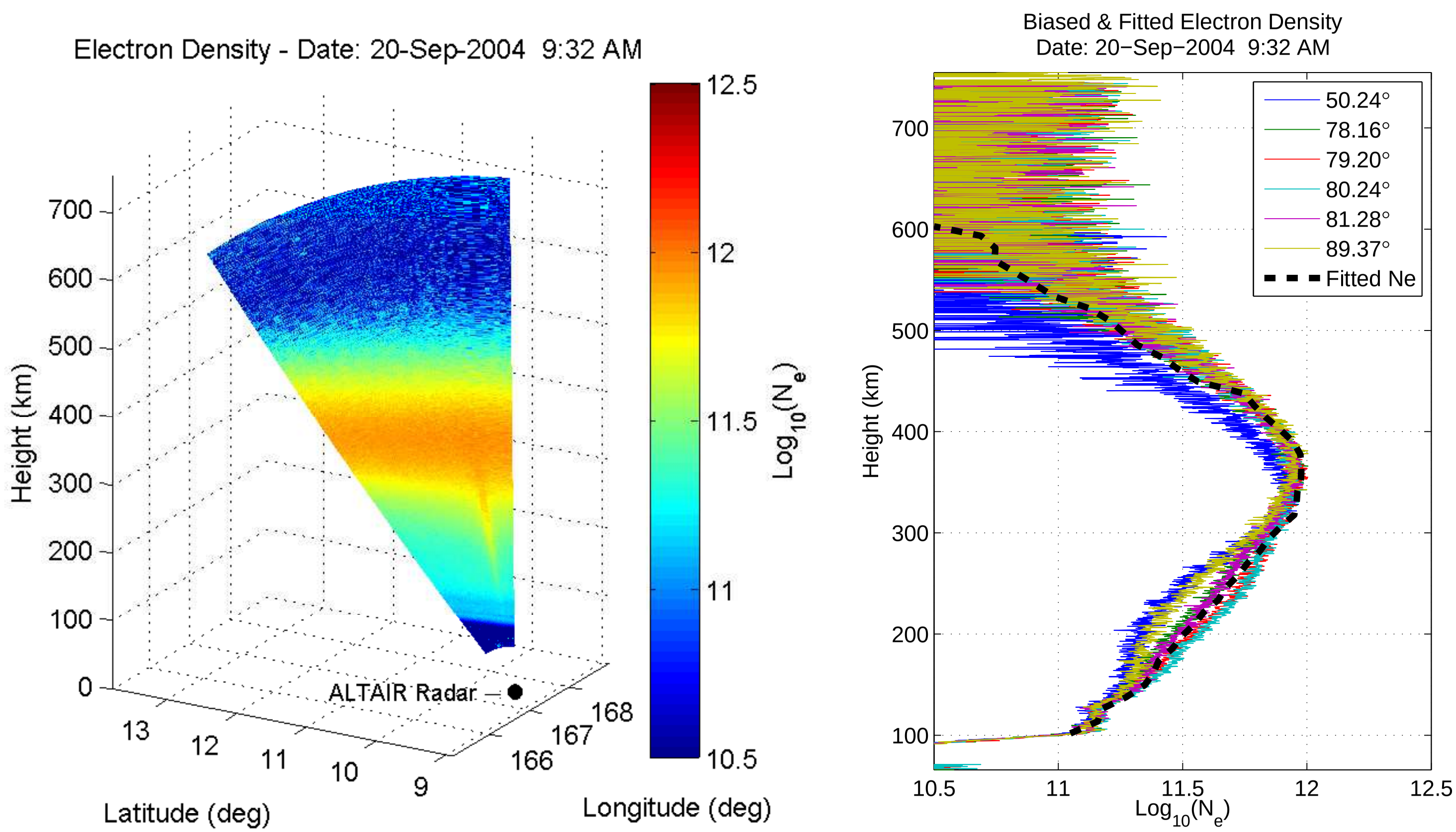

(a) (b)

Figure C.1 (a) Scan measurements and (b) electron density estimates — September 20, 2004 09:32 am.

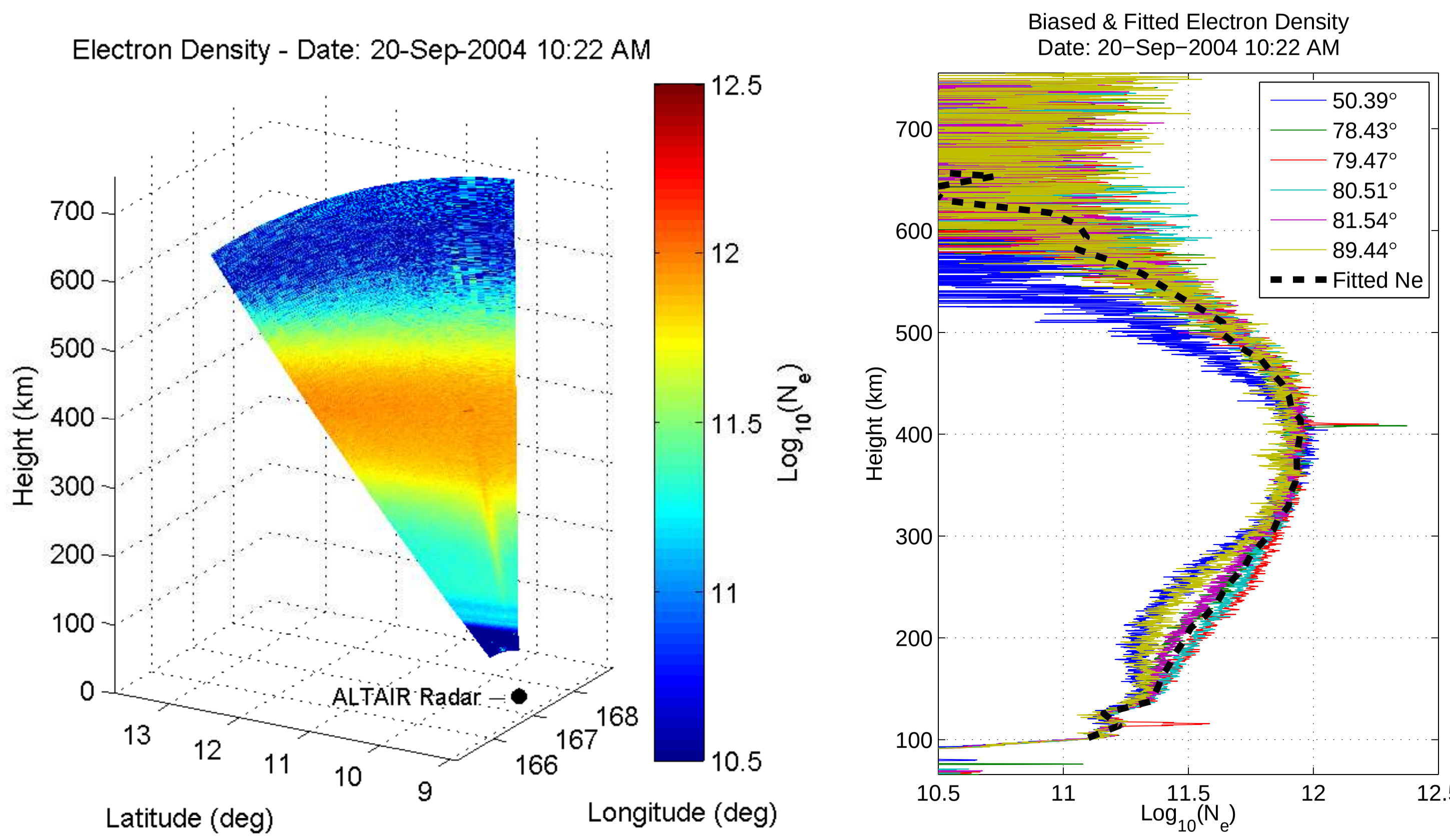

(a) (b)

Figure C.2 (a) Scan measurements and (b) electron density estimates — September 20, 2004 10:22 am.

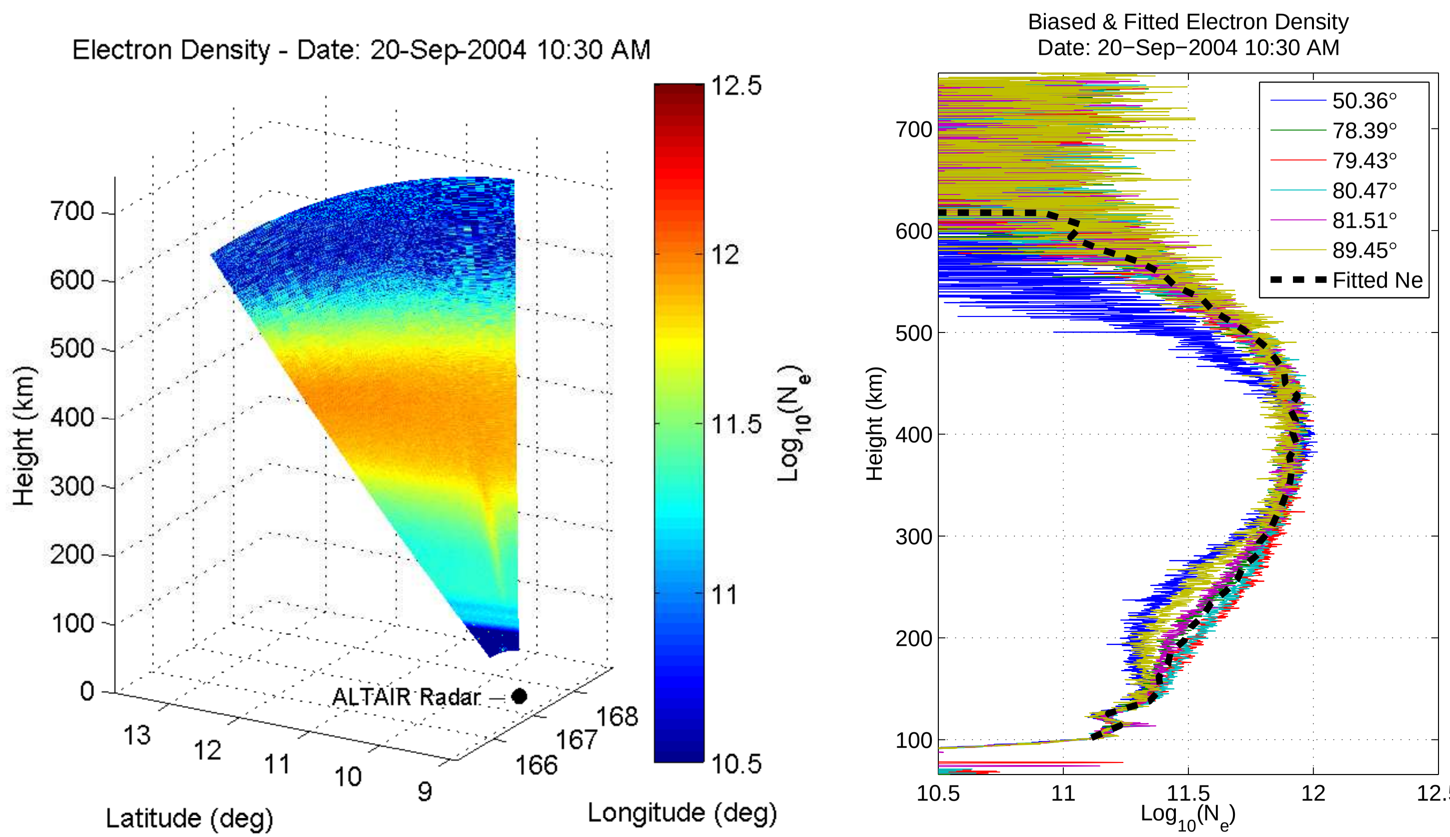

(a) (b)

Figure C.3 (a) Scan measurements and (b) electron density estimates — September 20, 2004 10:30 am.

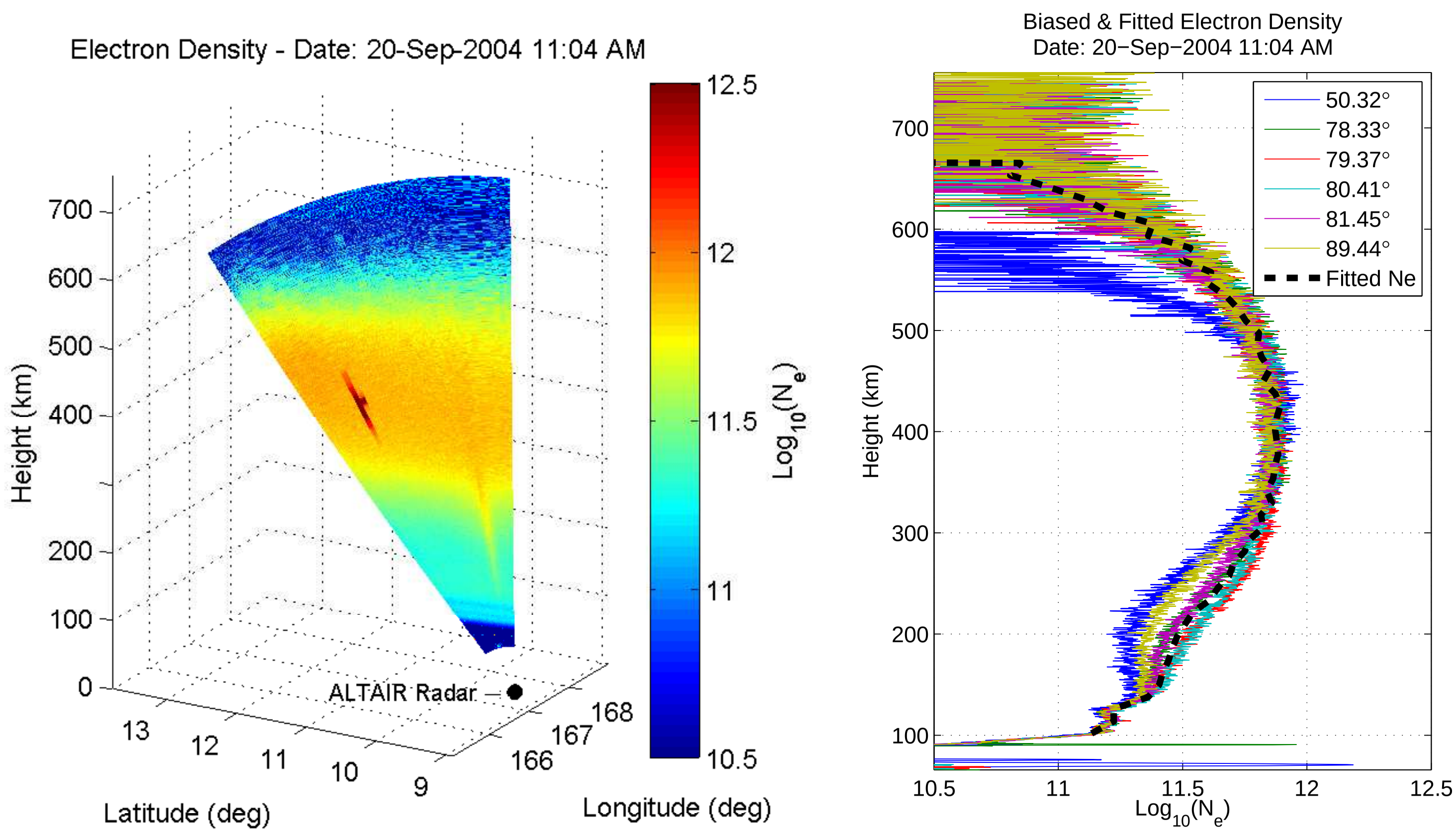

(a) (b)

Figure C.4 (a) Scan measurements and (b) electron density estimates — September 20, 2004 11:04 am.

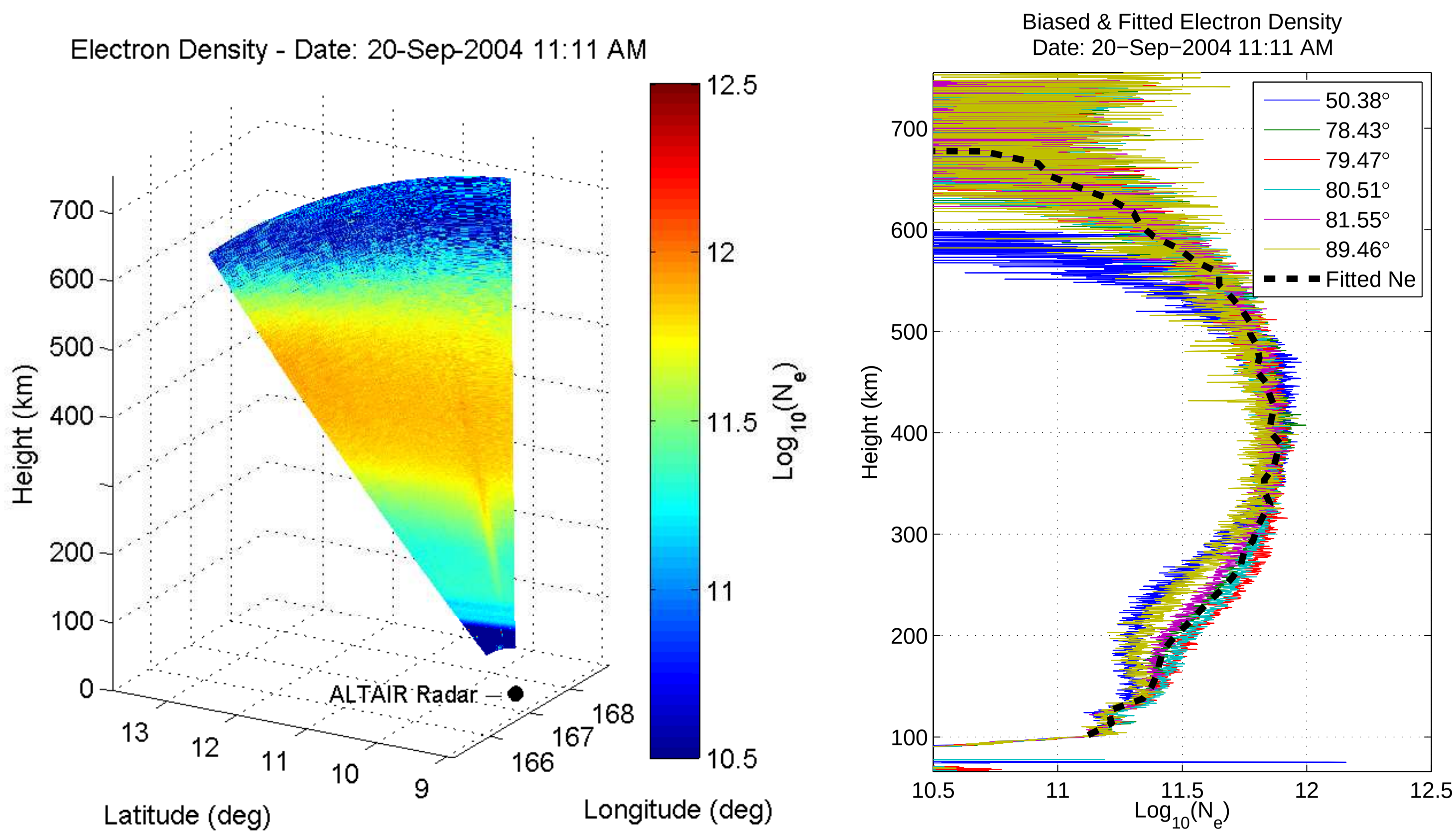

(a) (b)

Figure C.5 (a) Scan measurements and (b) electron density estimates — September 20, 2004 11:11 am.

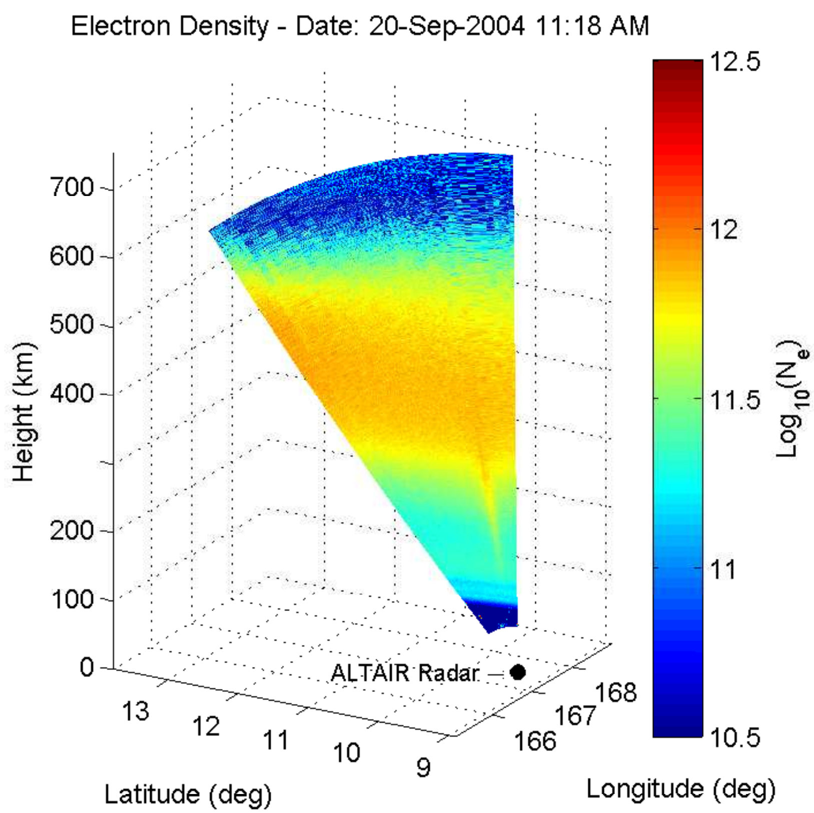

(a)

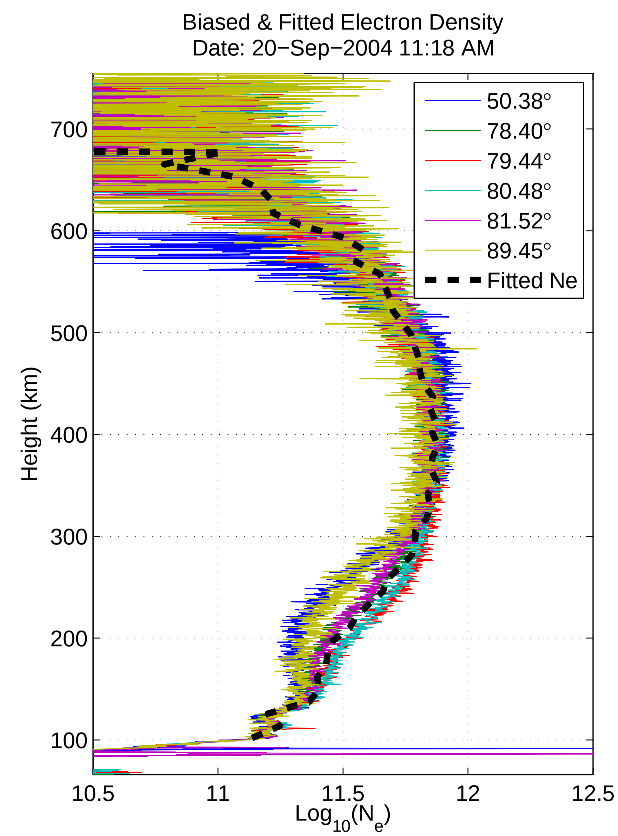

(b)

Figure C.6 (a) Scan measurements and (b) electron density estimates — September 20, 2004 11:18 am.

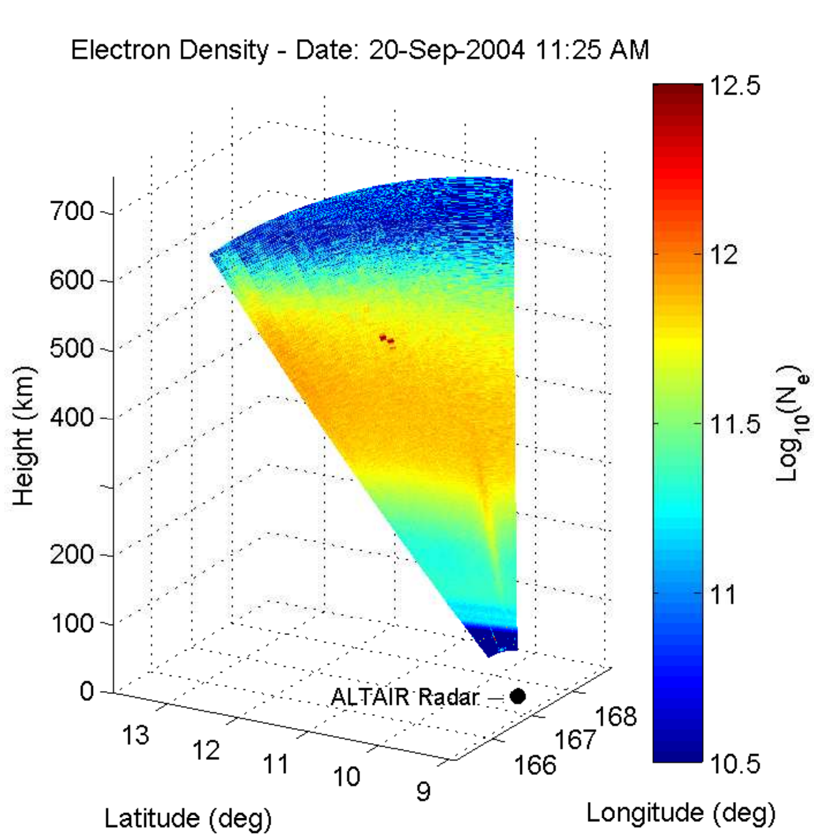

(a)

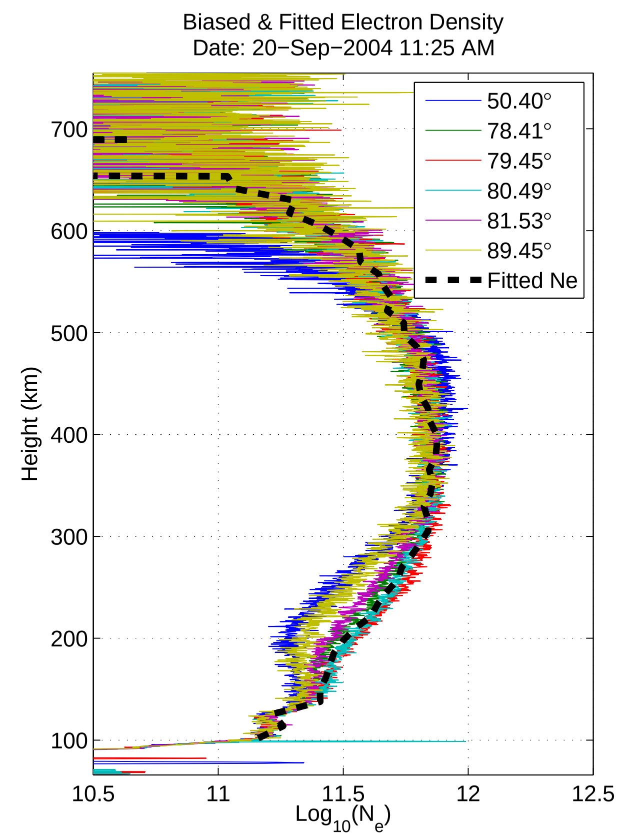

(b)

Figure C.7 (a) Scan measurements and (b) electron density estimates — September 20, 2004 11:25 am.

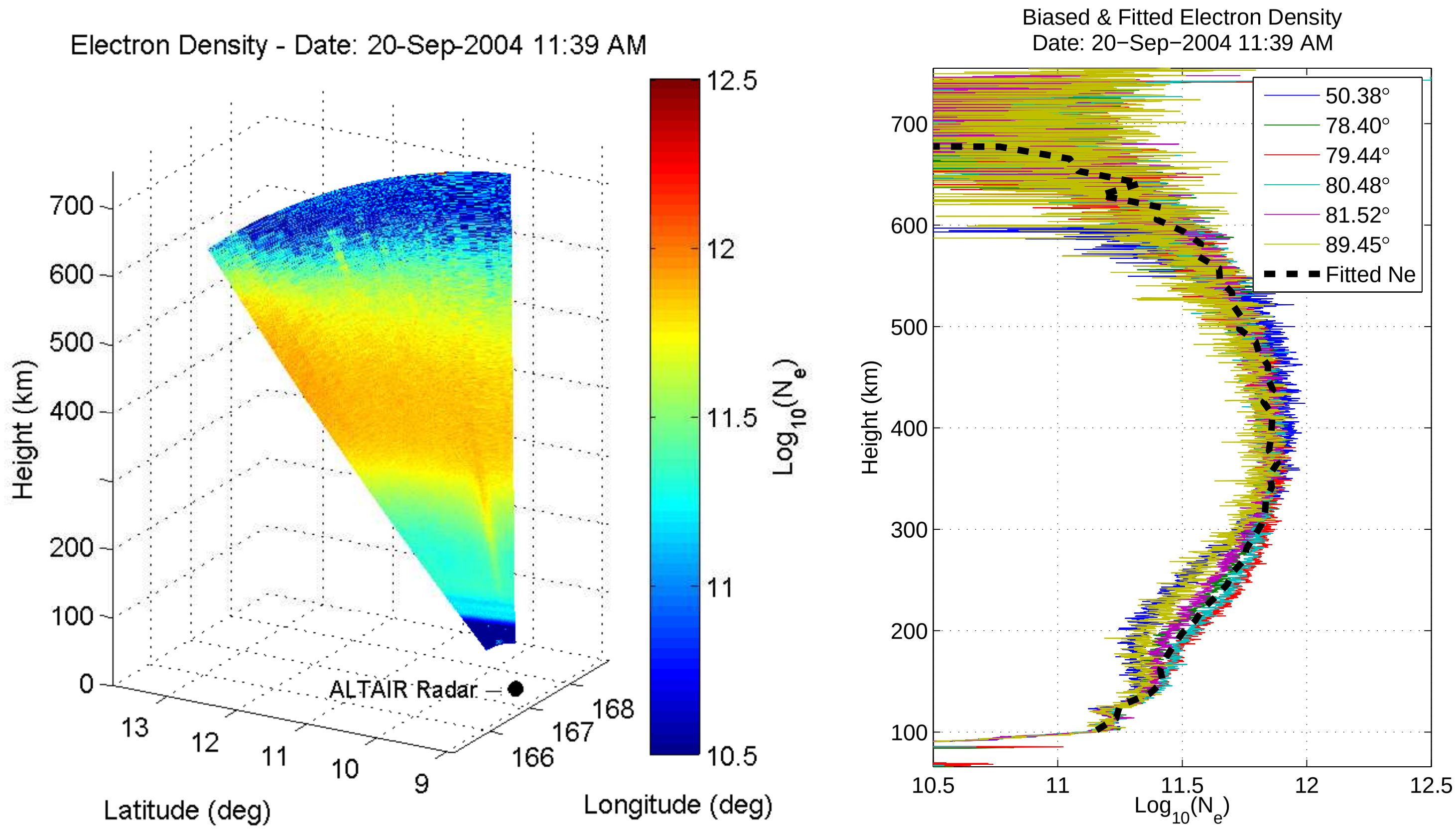

(a) (b)

Figure C.8 (a) Scan measurements and (b) electron density estimates — September 20, 2004 11:39 am.

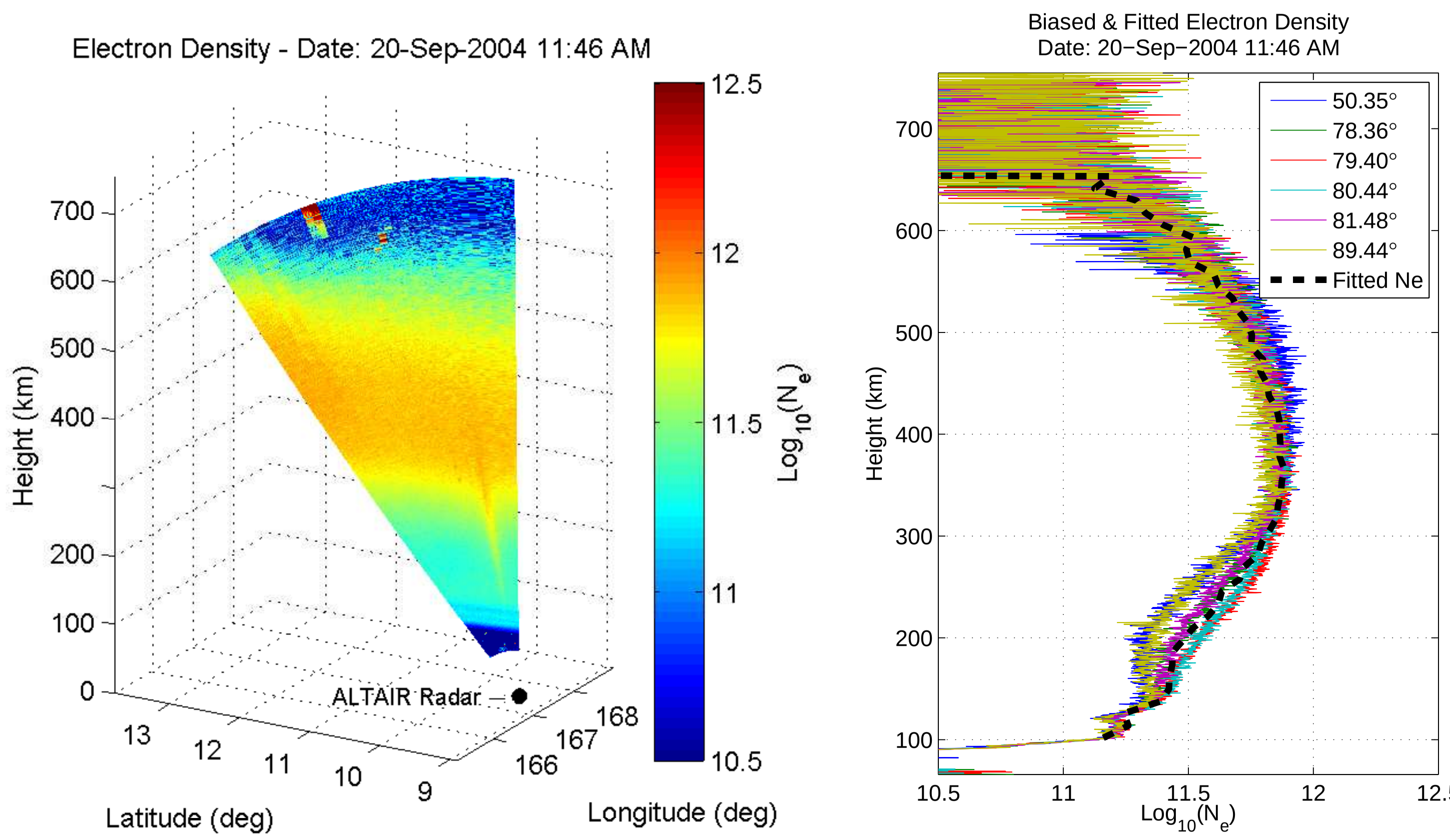

(a) (b)

Figure C.9 (a) Scan measurements and (b) electron density estimates — September 20, 2004 11:46 am.

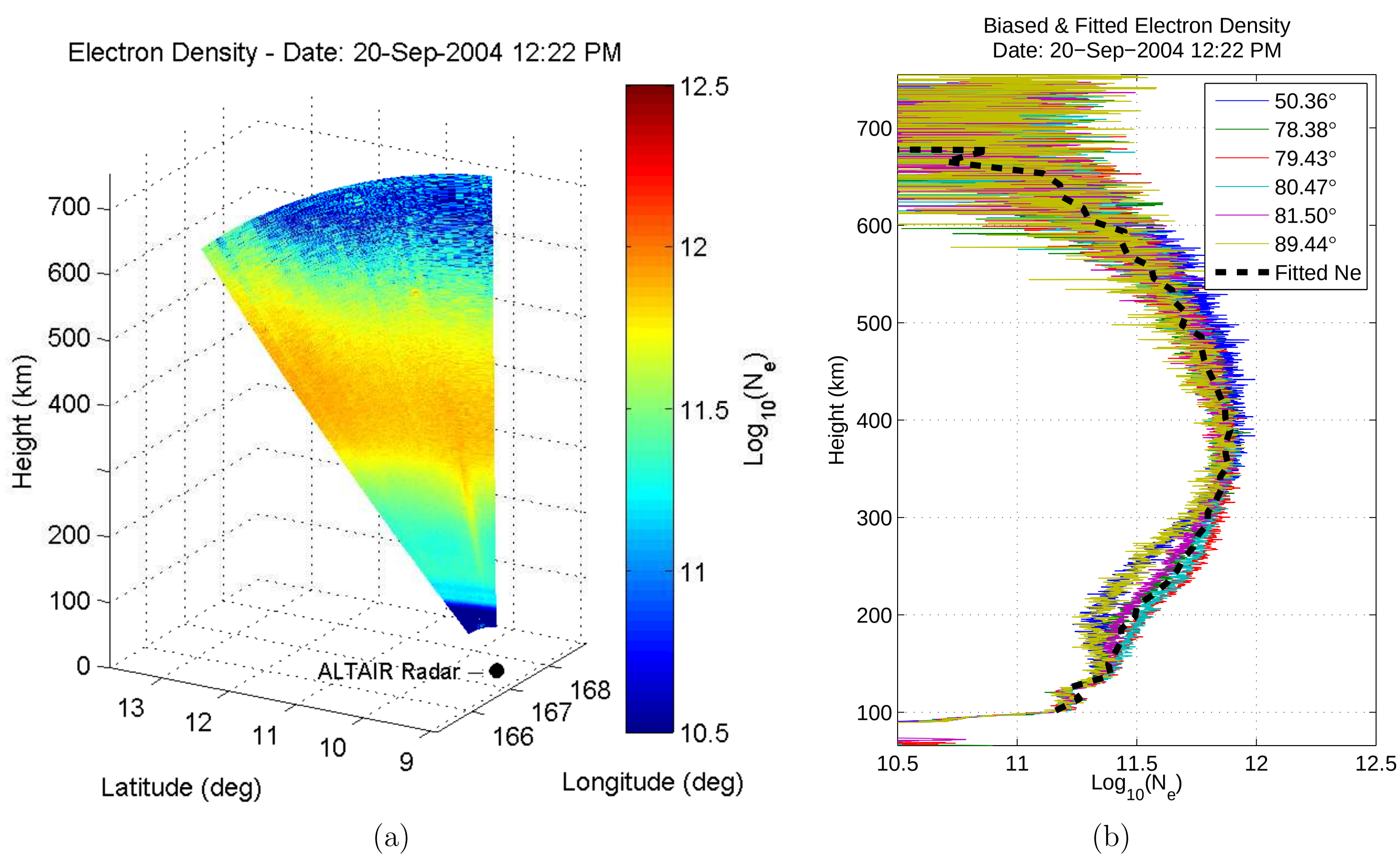

Figure C.10 (a) Scan measurements and (b) electron density estimates — September 20, 2004 12:22 pm.

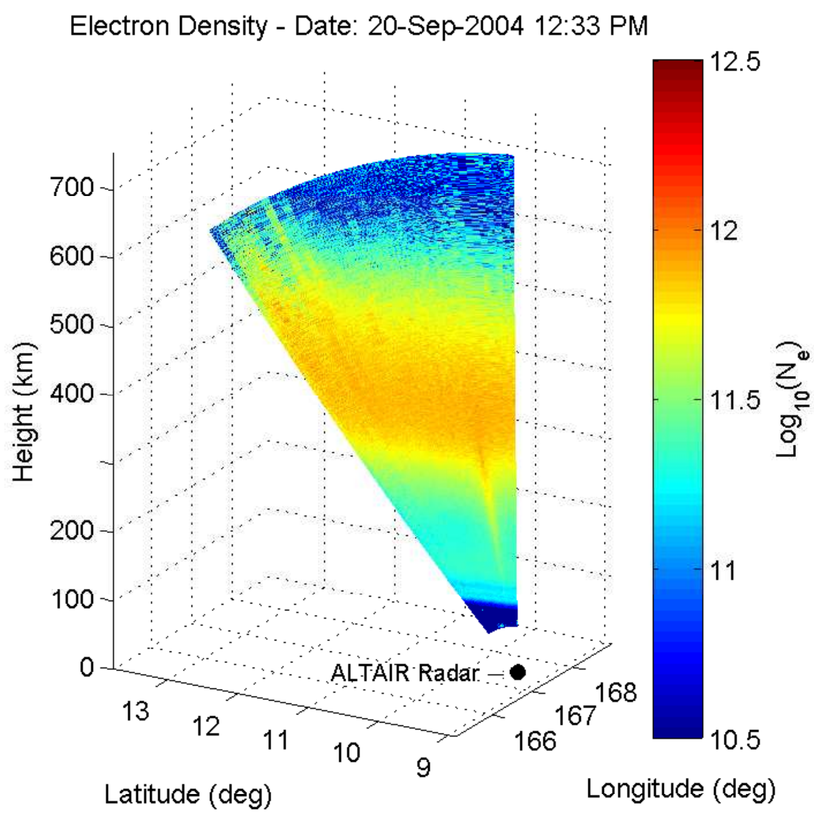

(a)

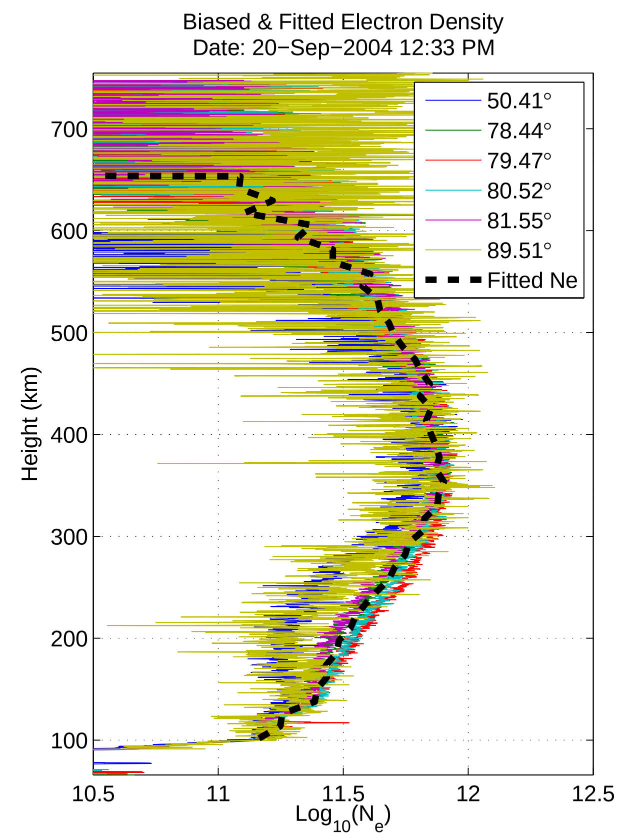

(b)

Figure C.11 (a) Scan measurements and (b) electron density estimates — September 20, 2004 12:33 pm.

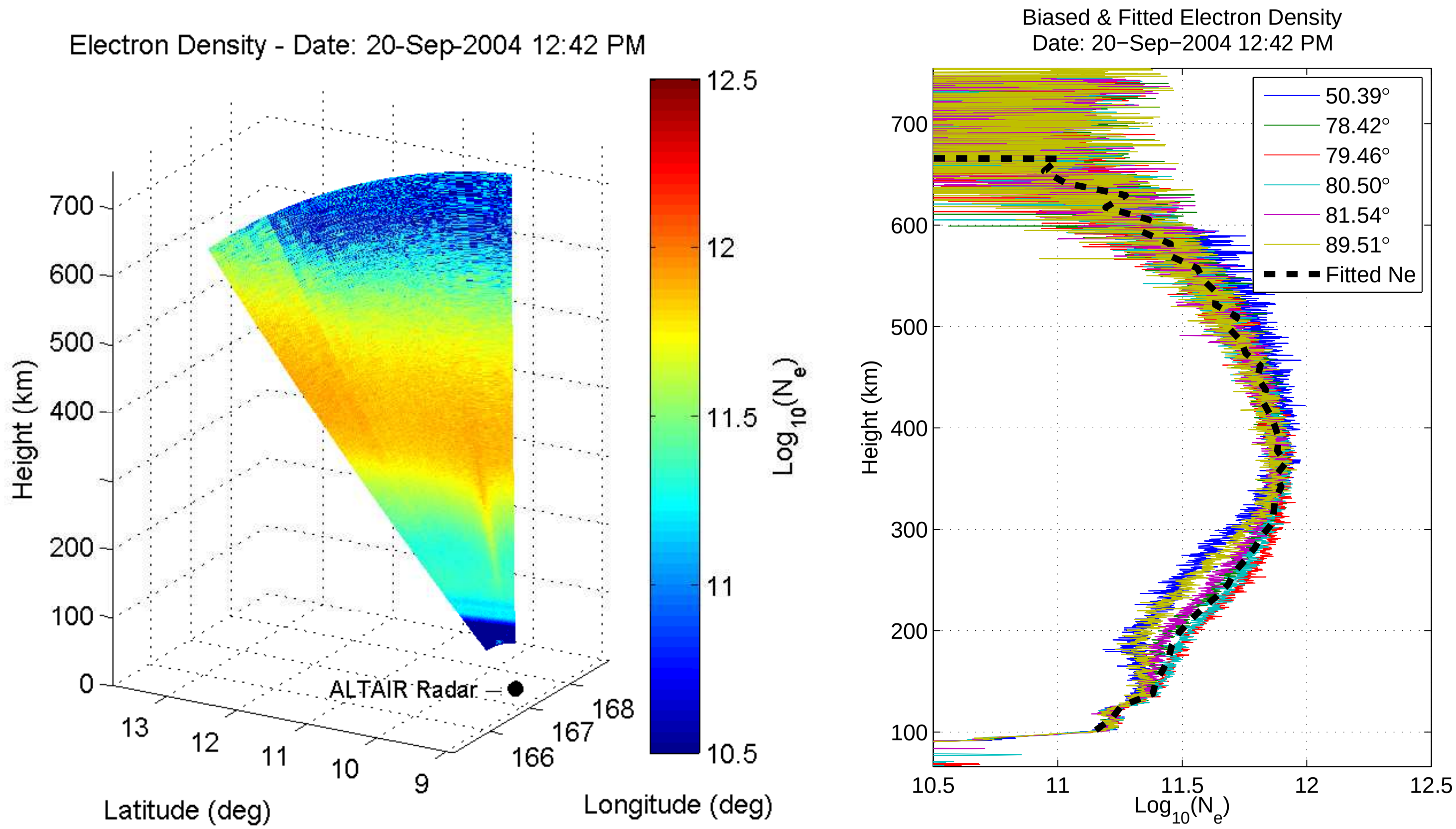

(a) (b)

Figure C.12 (a) Scan measurements and (b) electron density estimates — September 20, 2004 12:42 pm.

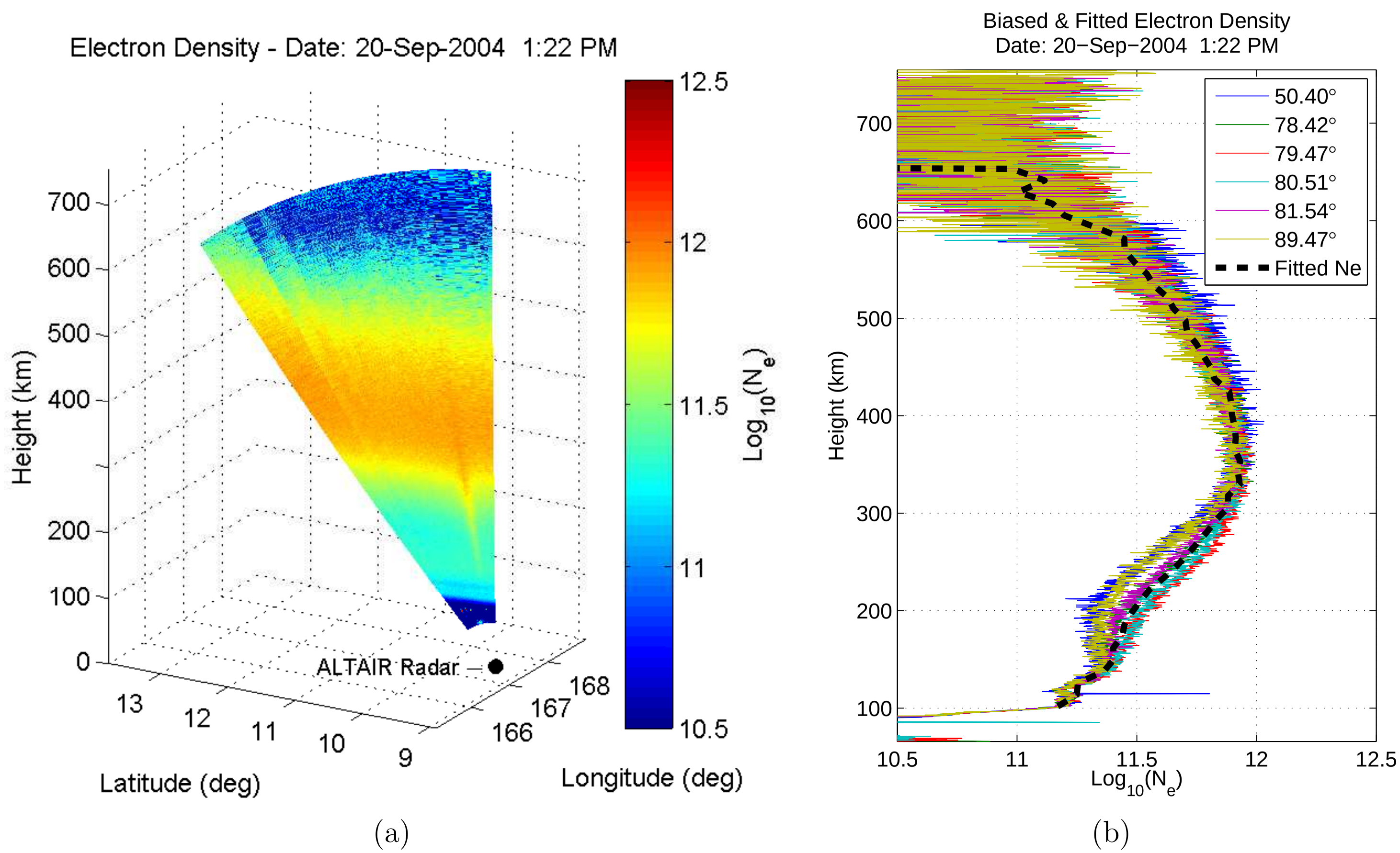

(a) (b)

Figure C.13 (a) Scan measurements and (b) electron density estimates — September 20, 2004 01:22 pm.

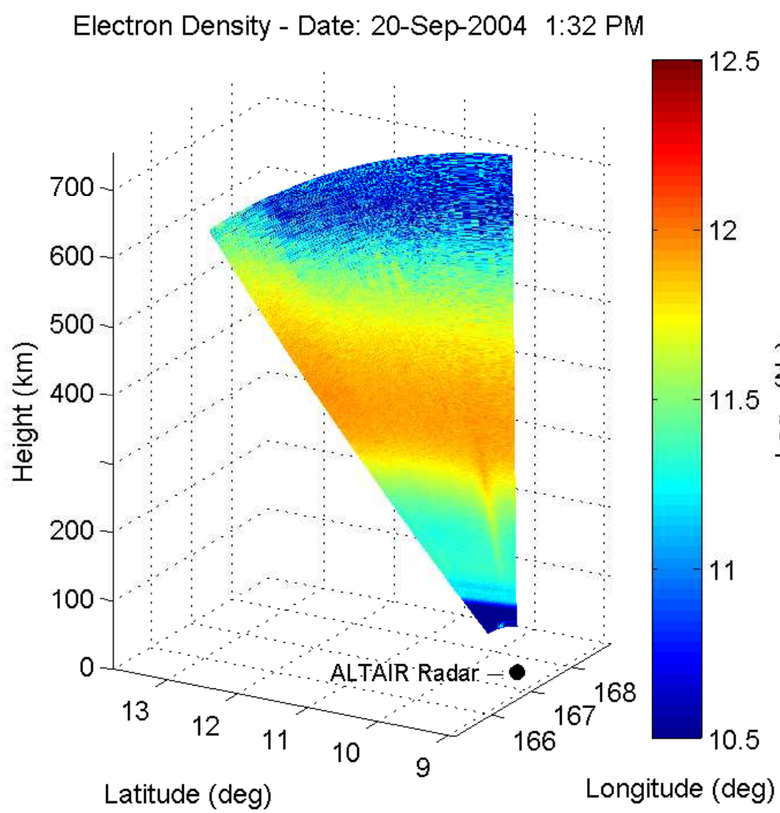

(a)

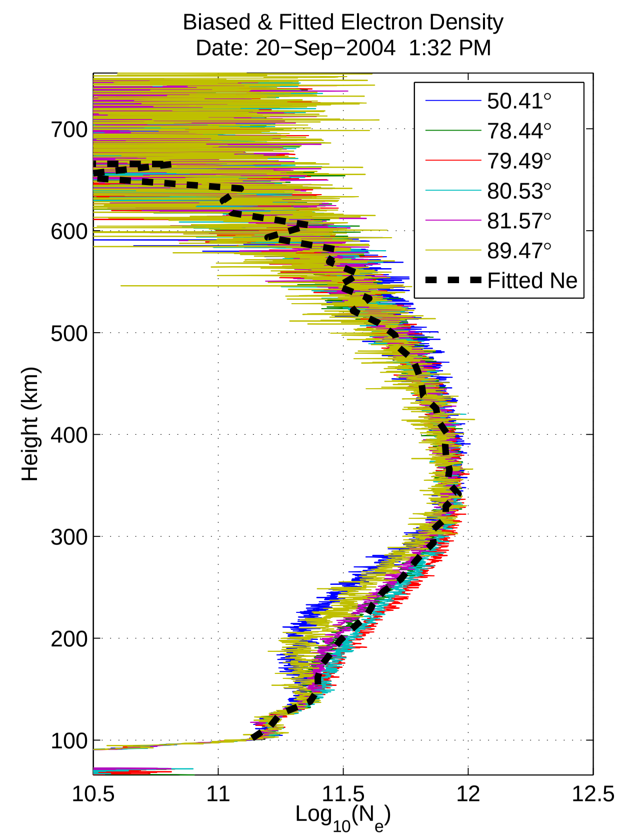

(b)

Figure C.14 (a) Scan measurements and (b) electron density estimates — September 20, 2004 01:32 pm.

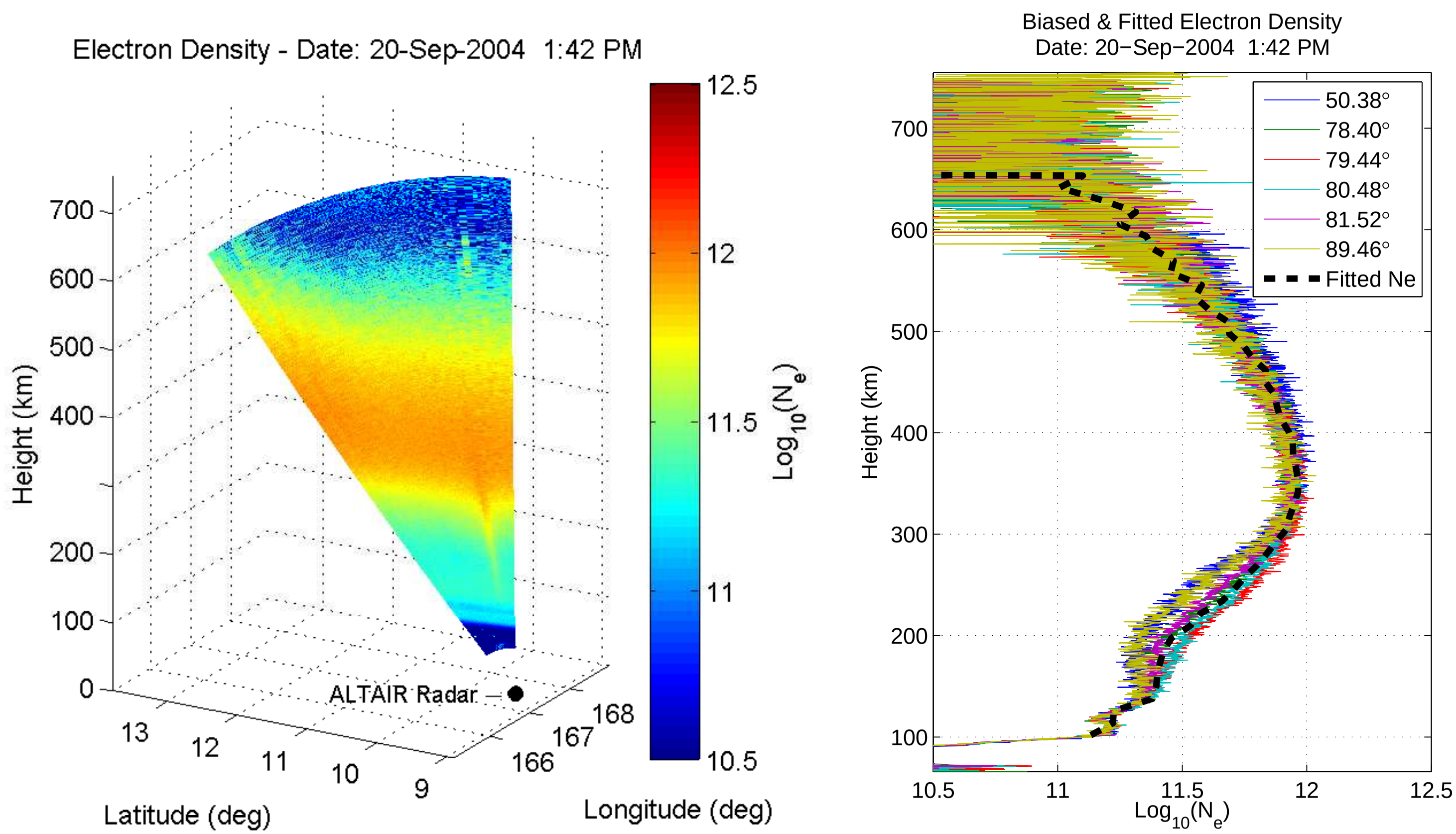

(a)

(b)

Figure C.15 (a) Scan measurements and (b) electron density estimates — September 20, 2004 01:42 pm.

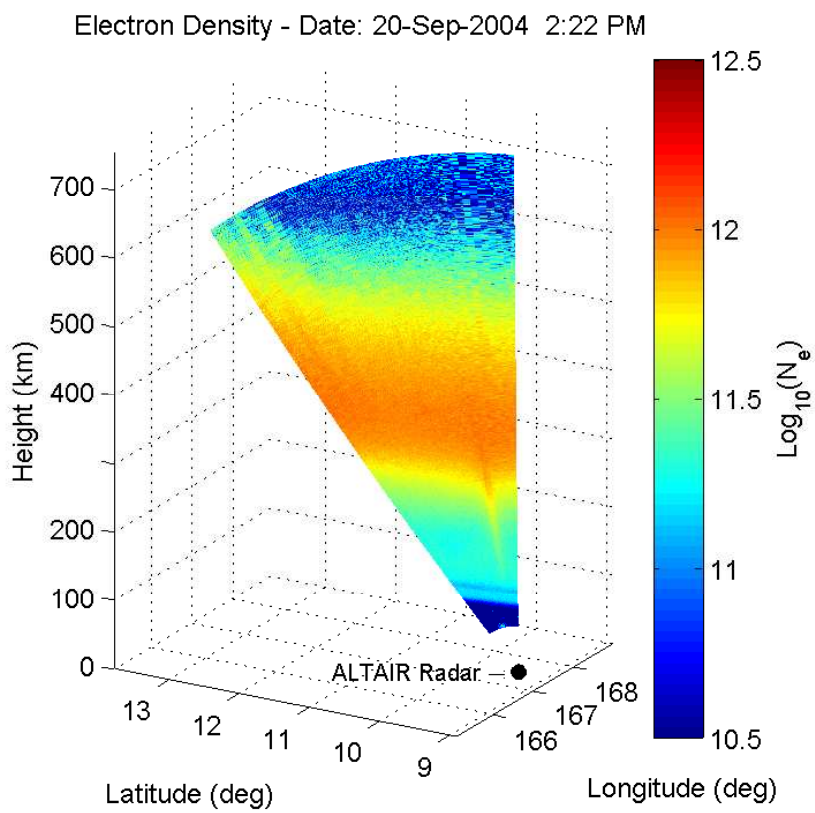

(a)

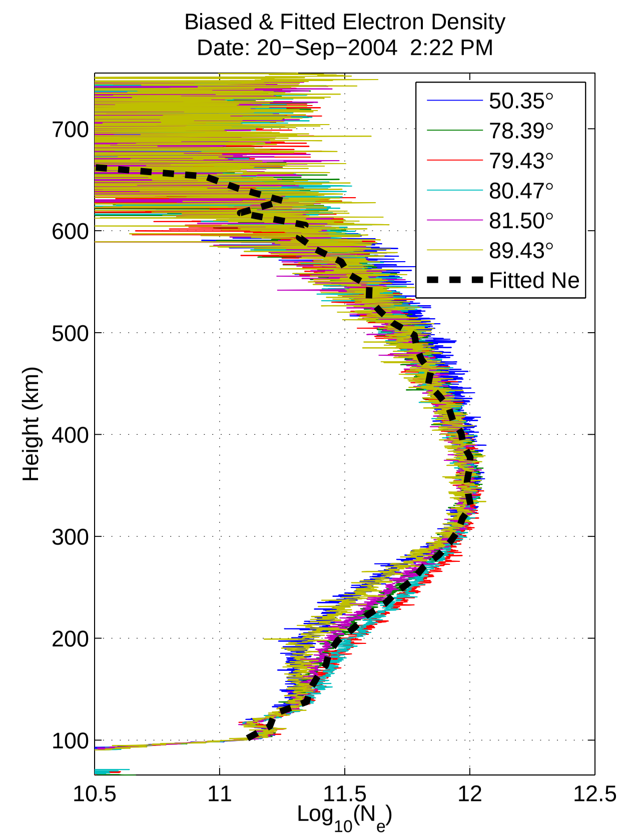

(b)

Figure C.16 (a) Scan measurements and (b) electron density estimates — September 20, 2004 02:22 pm.

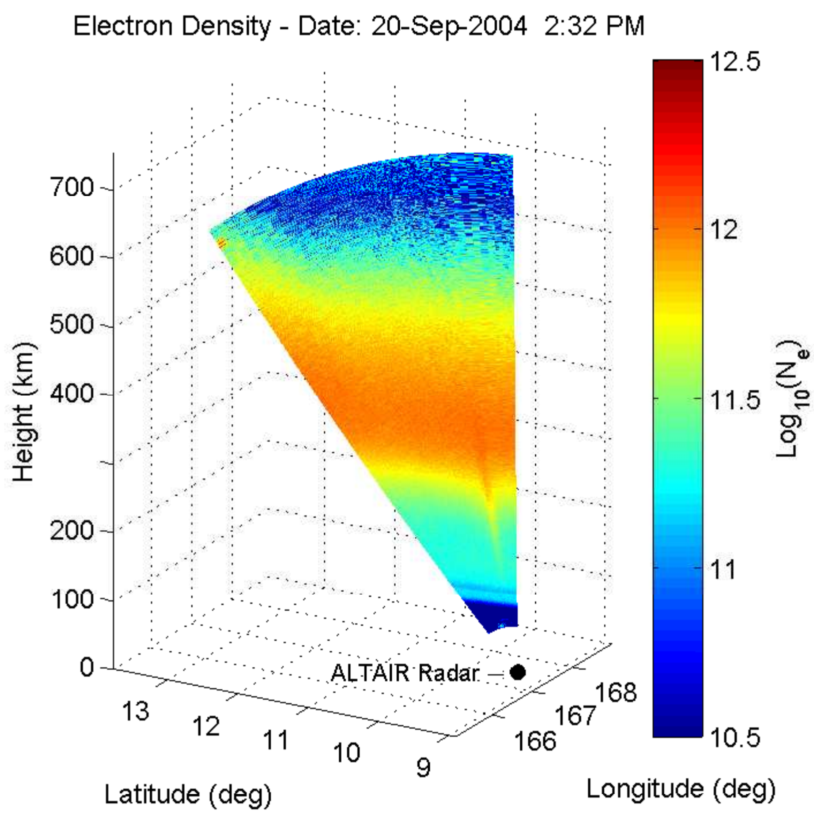

(a)

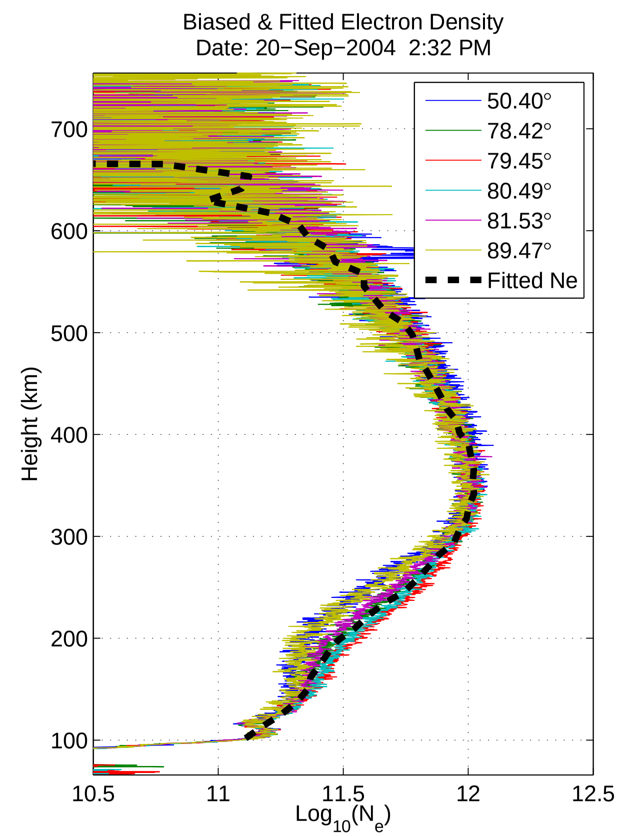

(b)

Figure C.17 (a) Scan measurements and (b) electron density estimates — September 20, 2004 02:32 pm.

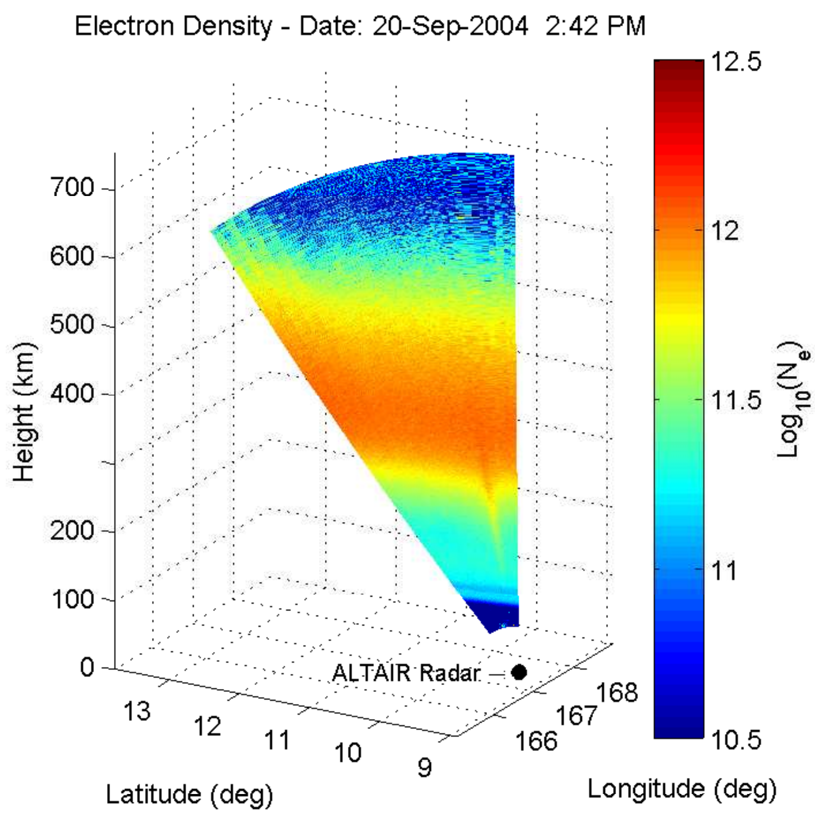

(a)

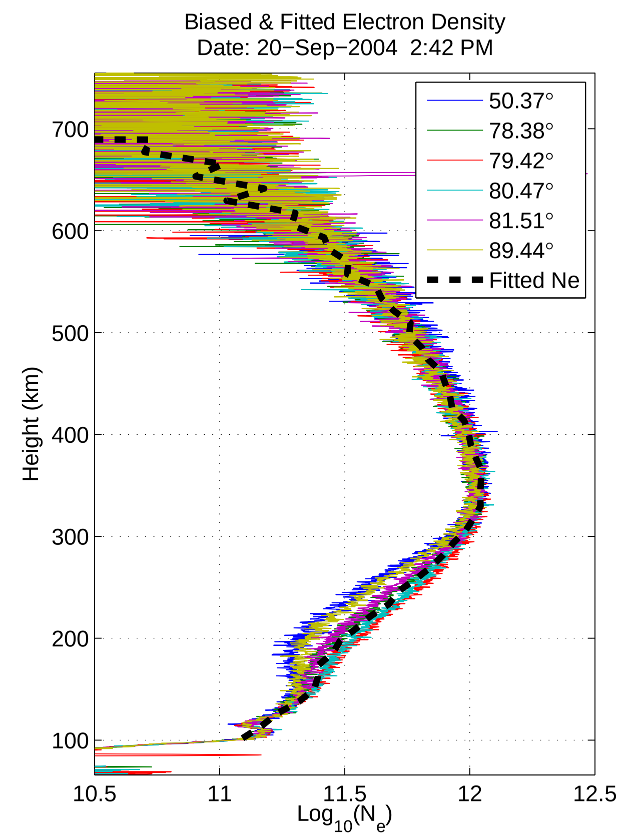

(b)

Figure C.18 (a) Scan measurements and (b) electron density estimates — September 20, 2004 02:42 pm.

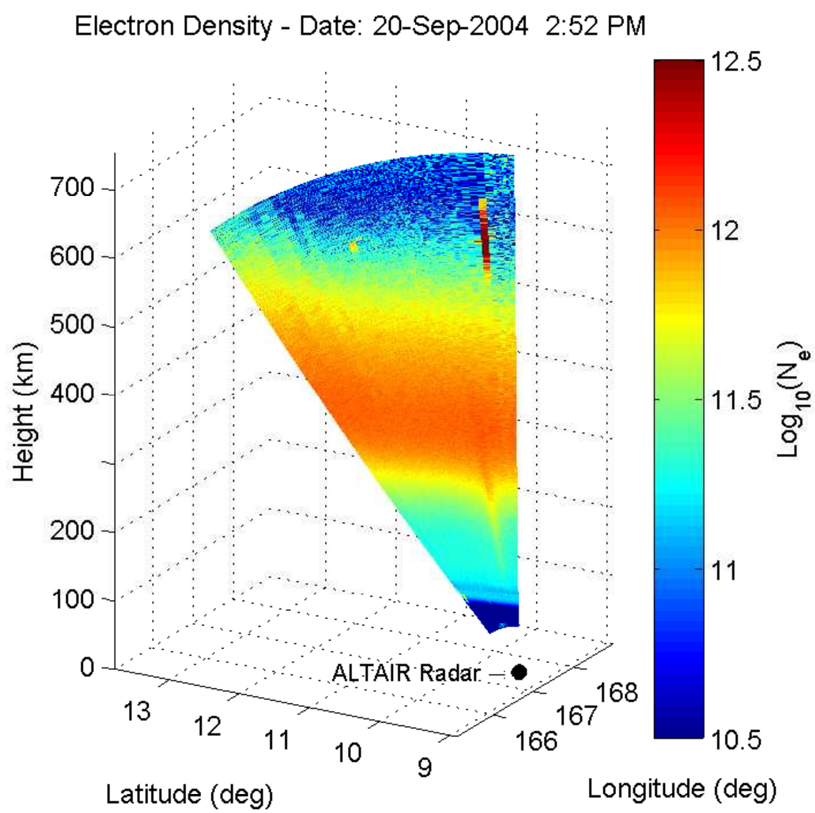

(a)

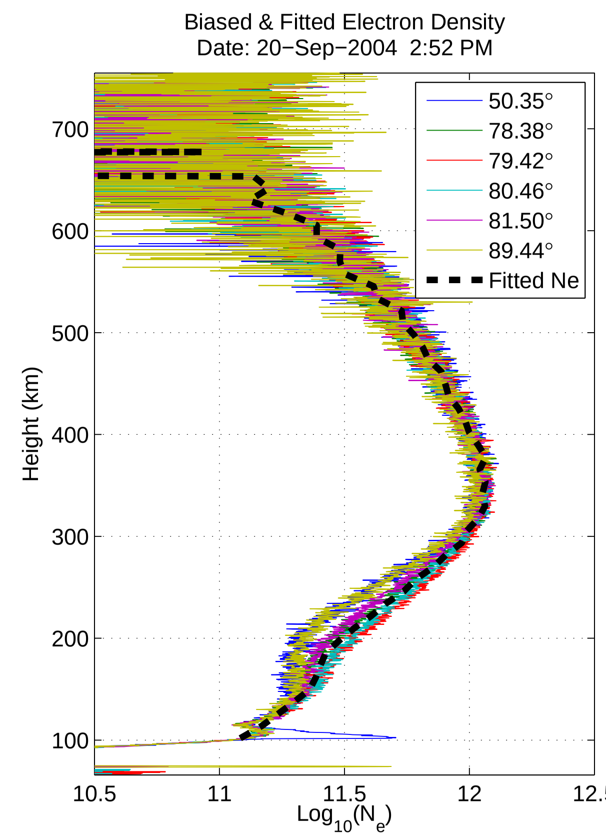

(b)

Figure C.19 (a) Scan measurements and (b) electron density estimates — September 20, 2004 02:52 pm.

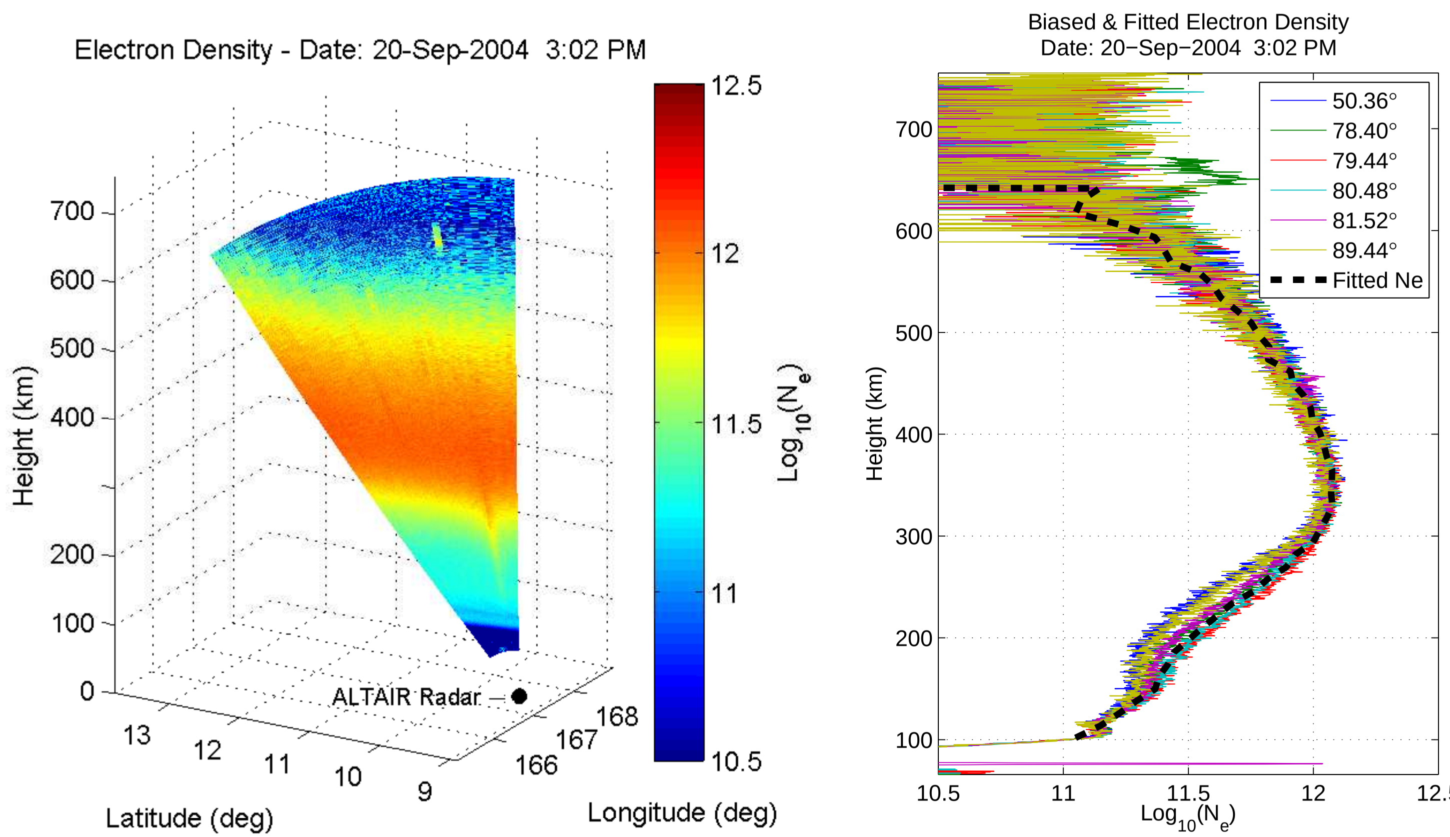

(a) (b)

Figure C.20 (a) Scan measurements and (b) electron density estimates — September 20, 2004 03:02 pm.

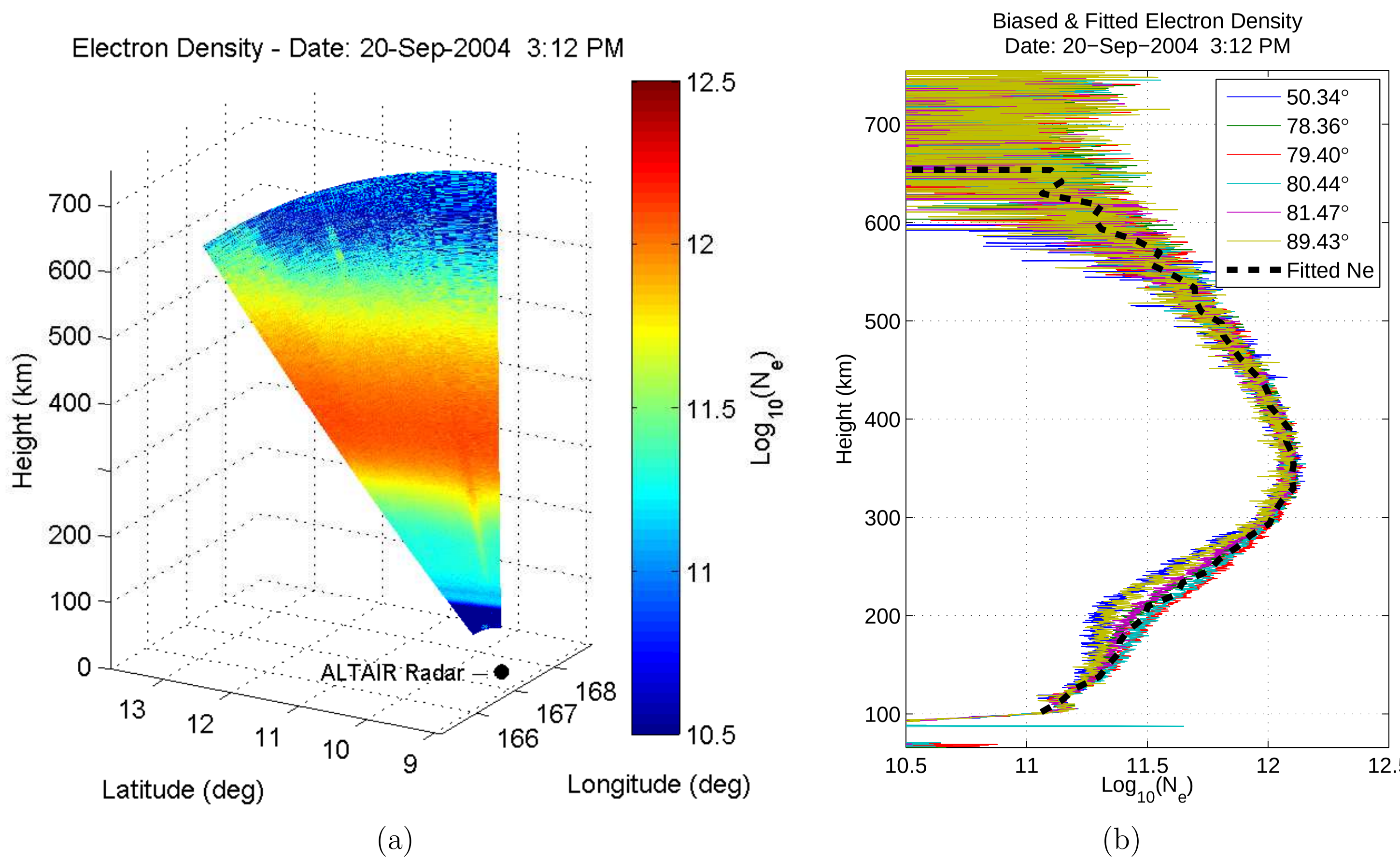

Figure C.21 (a) Scan measurements and (b) electron density estimates — September 20, 2004 03:12 pm.

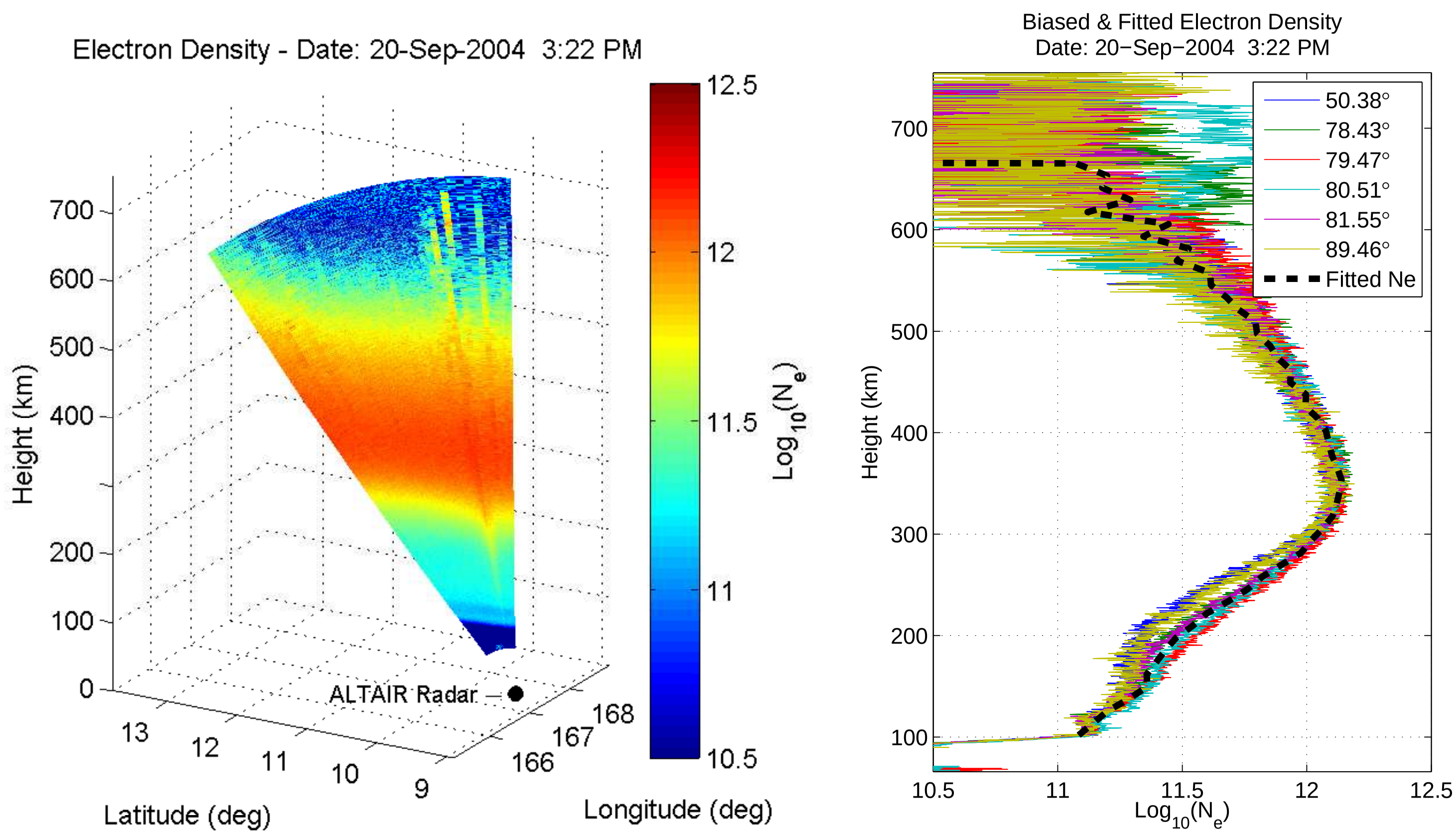

(a) (b)

Figure C.22 (a) Scan measurements and (b) electron density estimates — September 20, 2004 03:22 pm.

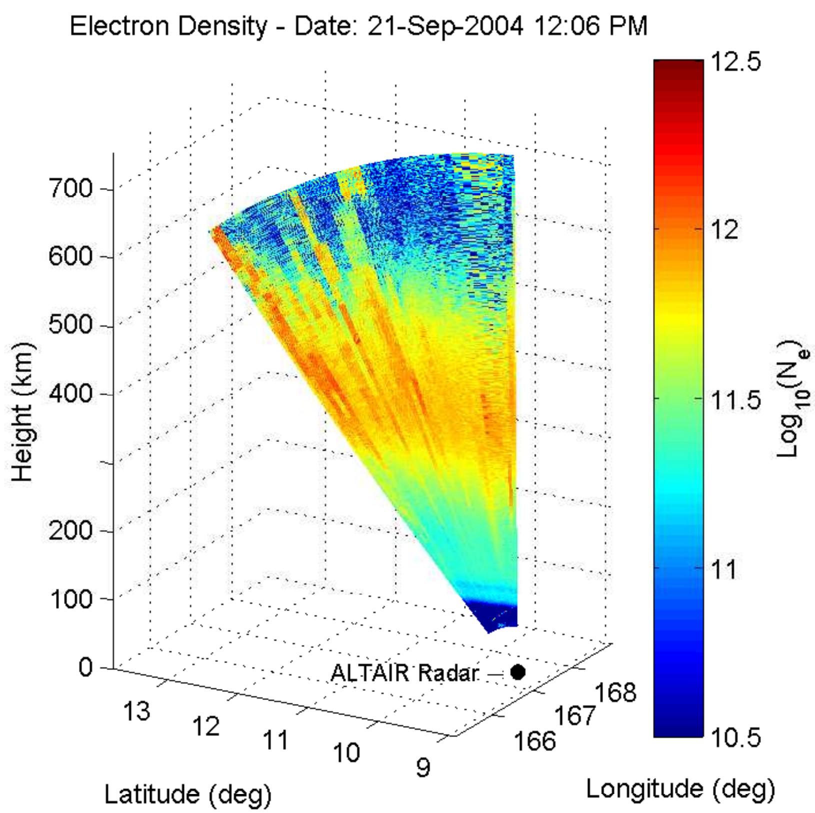

(a)

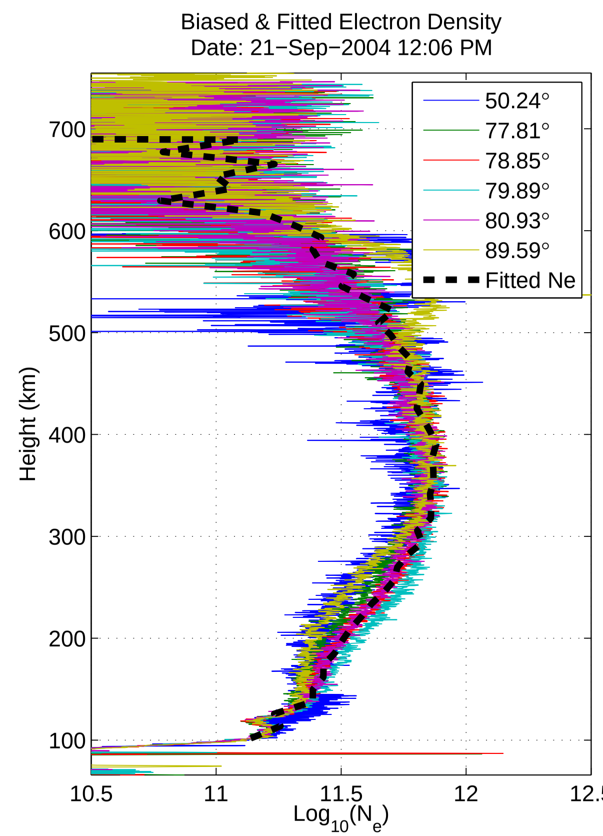

(b)

Figure C.23 (a) Scan measurements and (b) electron density estimates — September 21, 2004 12:06 pm.

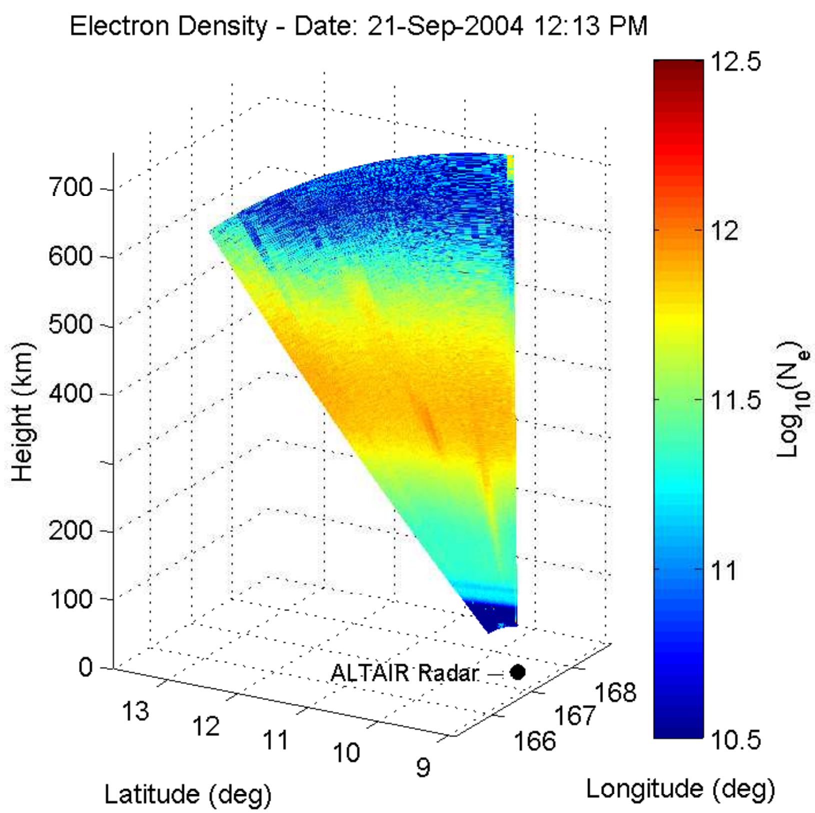

(a)

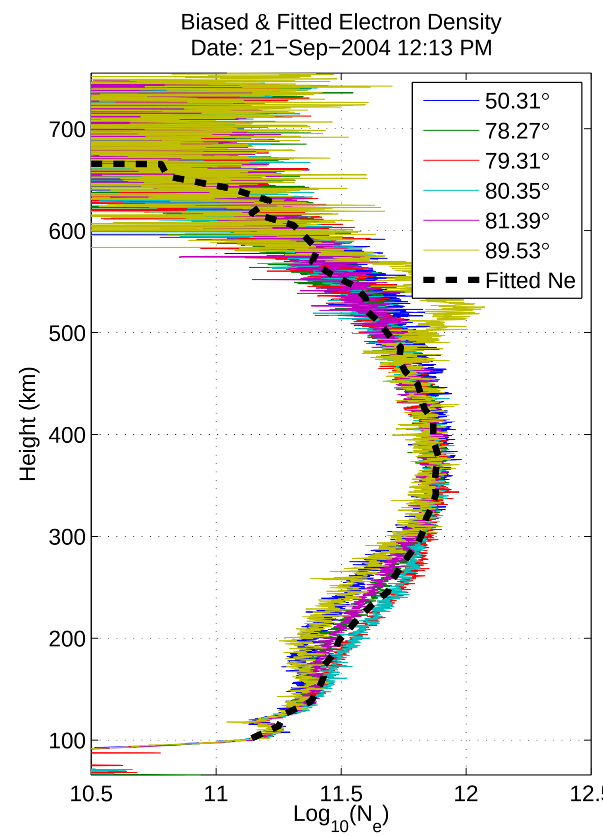

(b)

Figure C.24 (a) Scan measurements and (b) electron density estimates — September 21, 2004 12:13 pm.

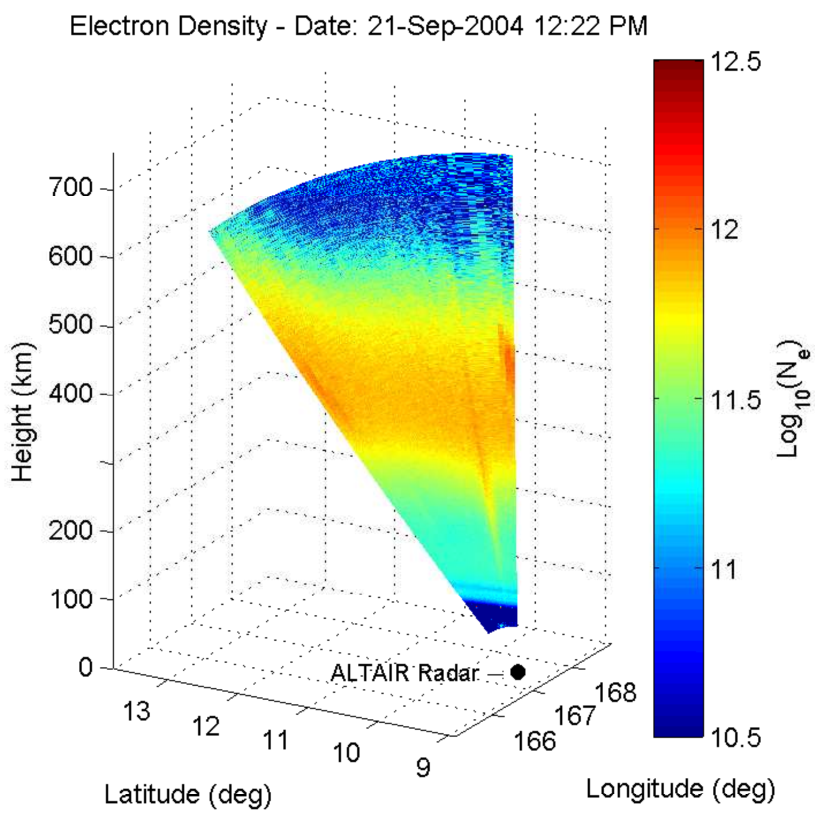

(a)

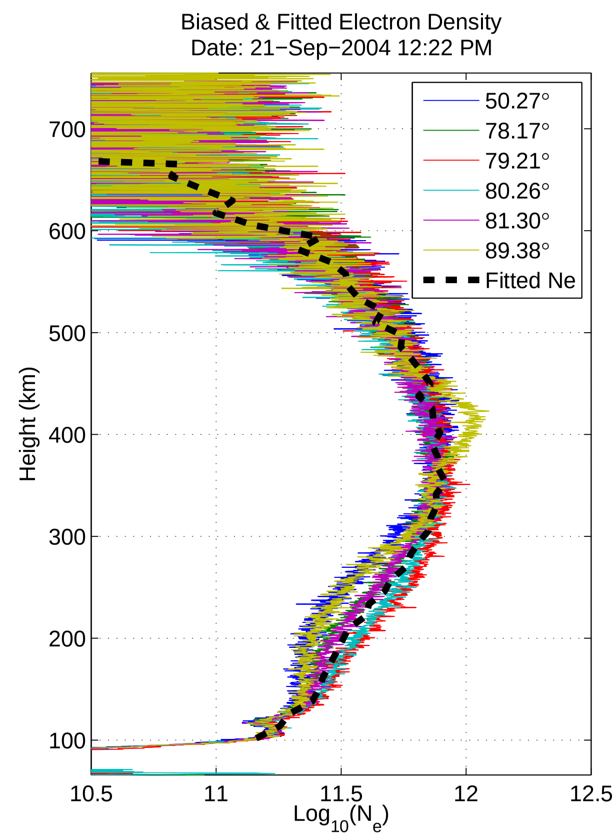

(b)

Figure C.25 (a) Scan measurements and (b) electron density estimates — September 21, 2004 12:22 pm.

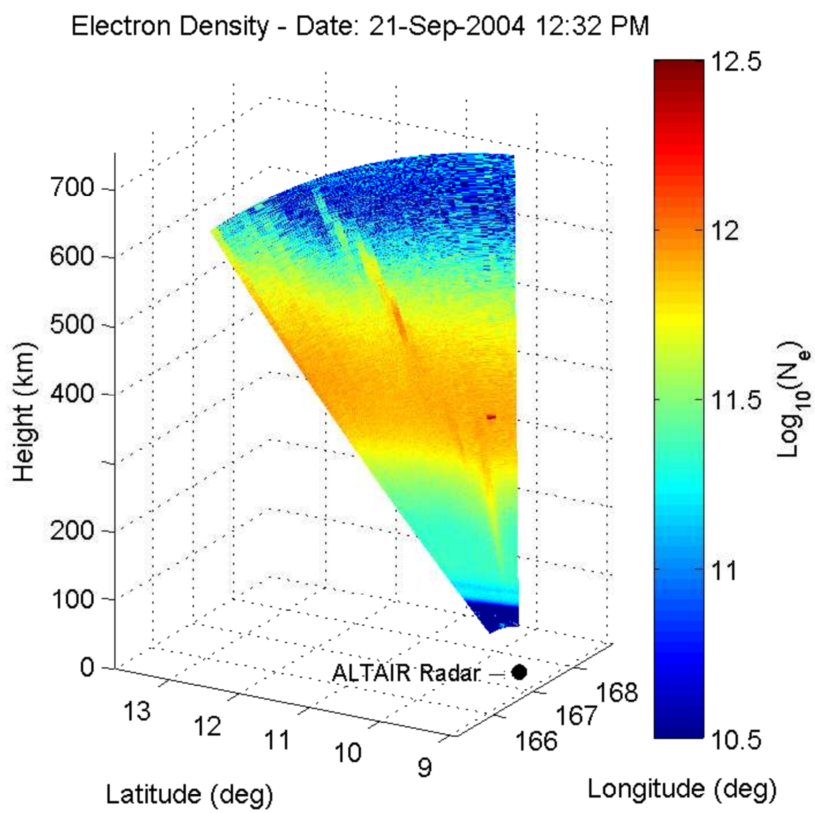

(a)

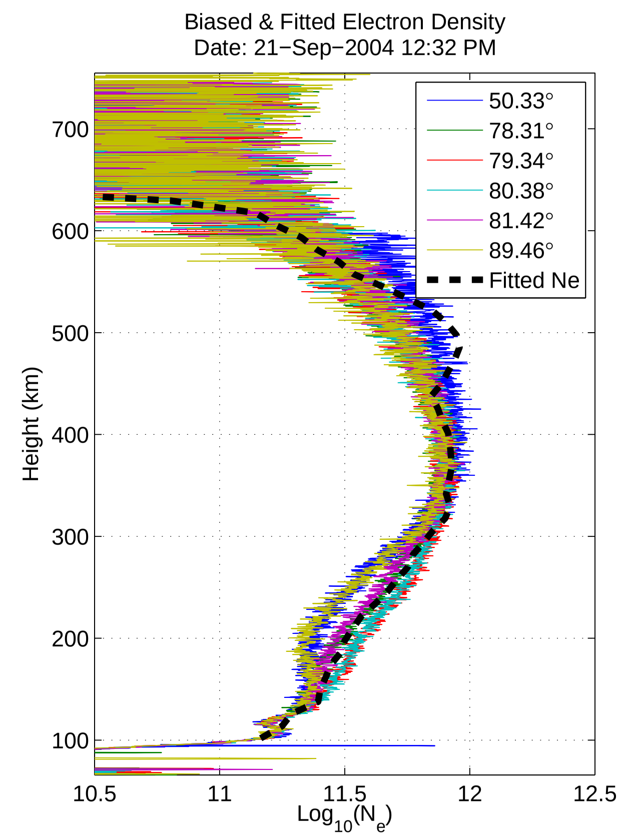

(b)

Figure C.26 (a) Scan measurements and (b) electron density estimates — September 21, 2004 12:32 pm.

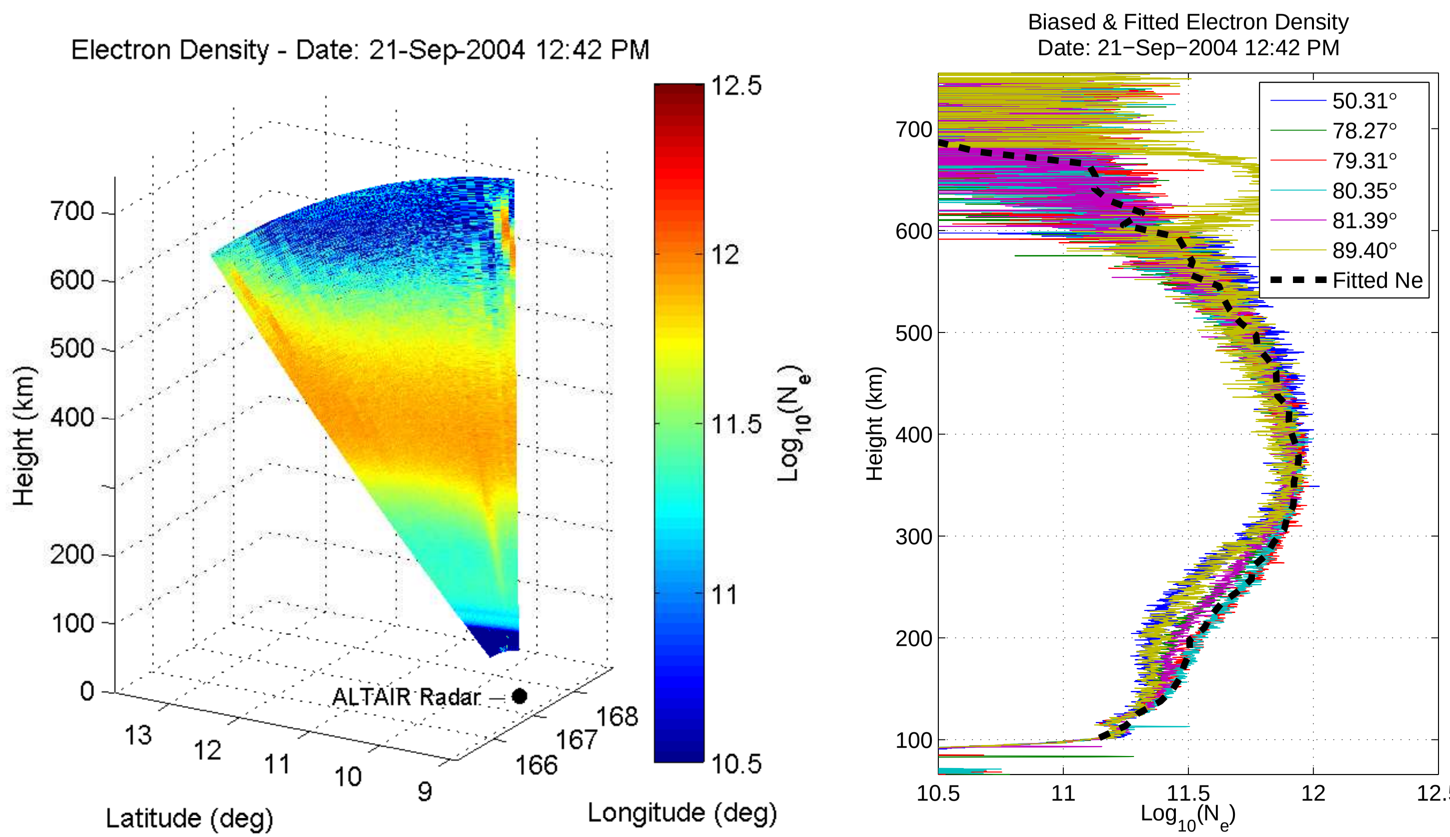

(a) (b)

Figure C.27 (a) Scan measurements and (b) electron density estimates — September 21, 2004 12:42 pm.

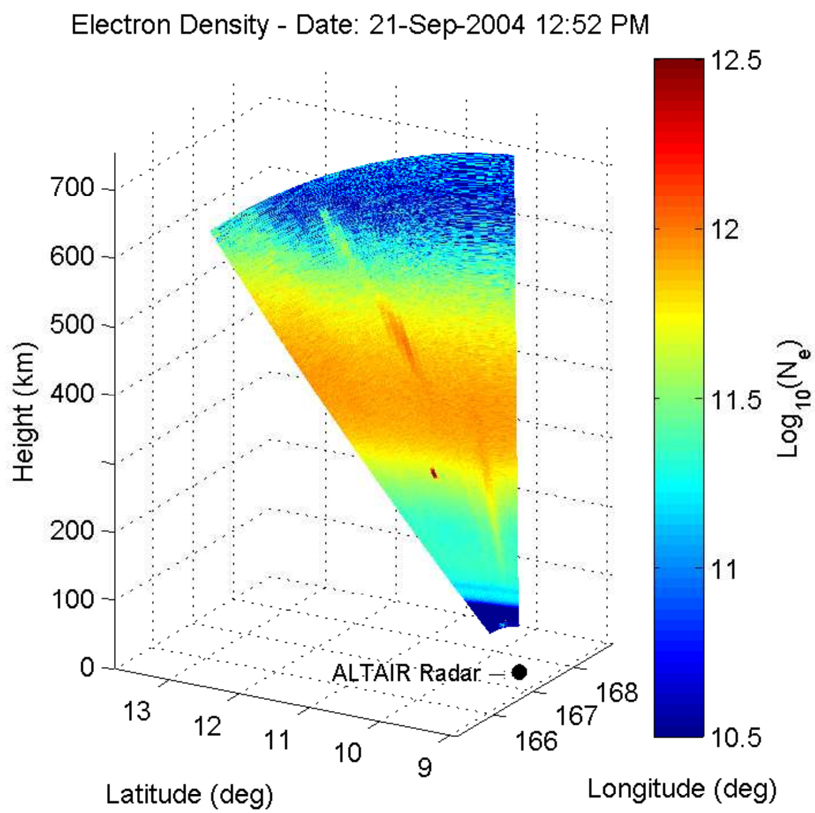

(a)

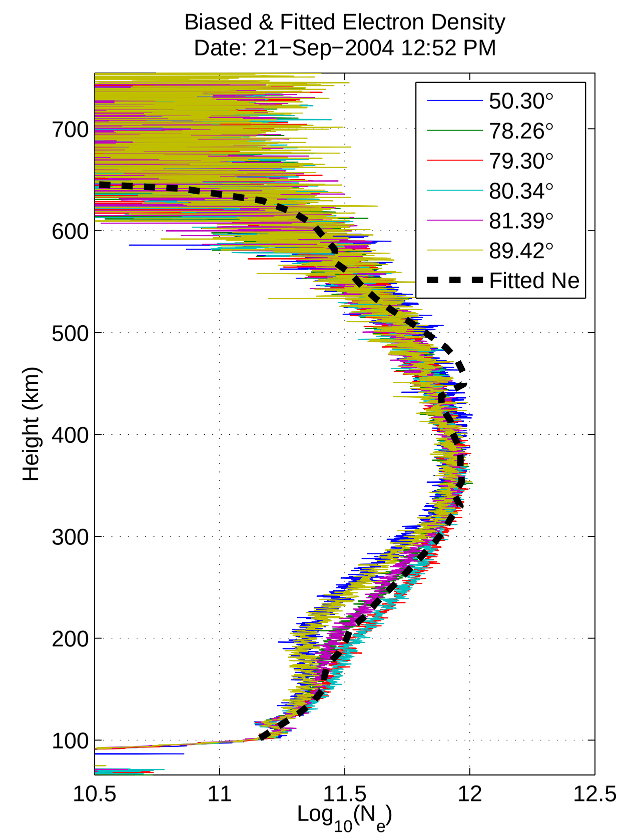

(b)

Figure C.28 (a) Scan measurements and (b) electron density estimates — September 21, 2004 12:52 pm.

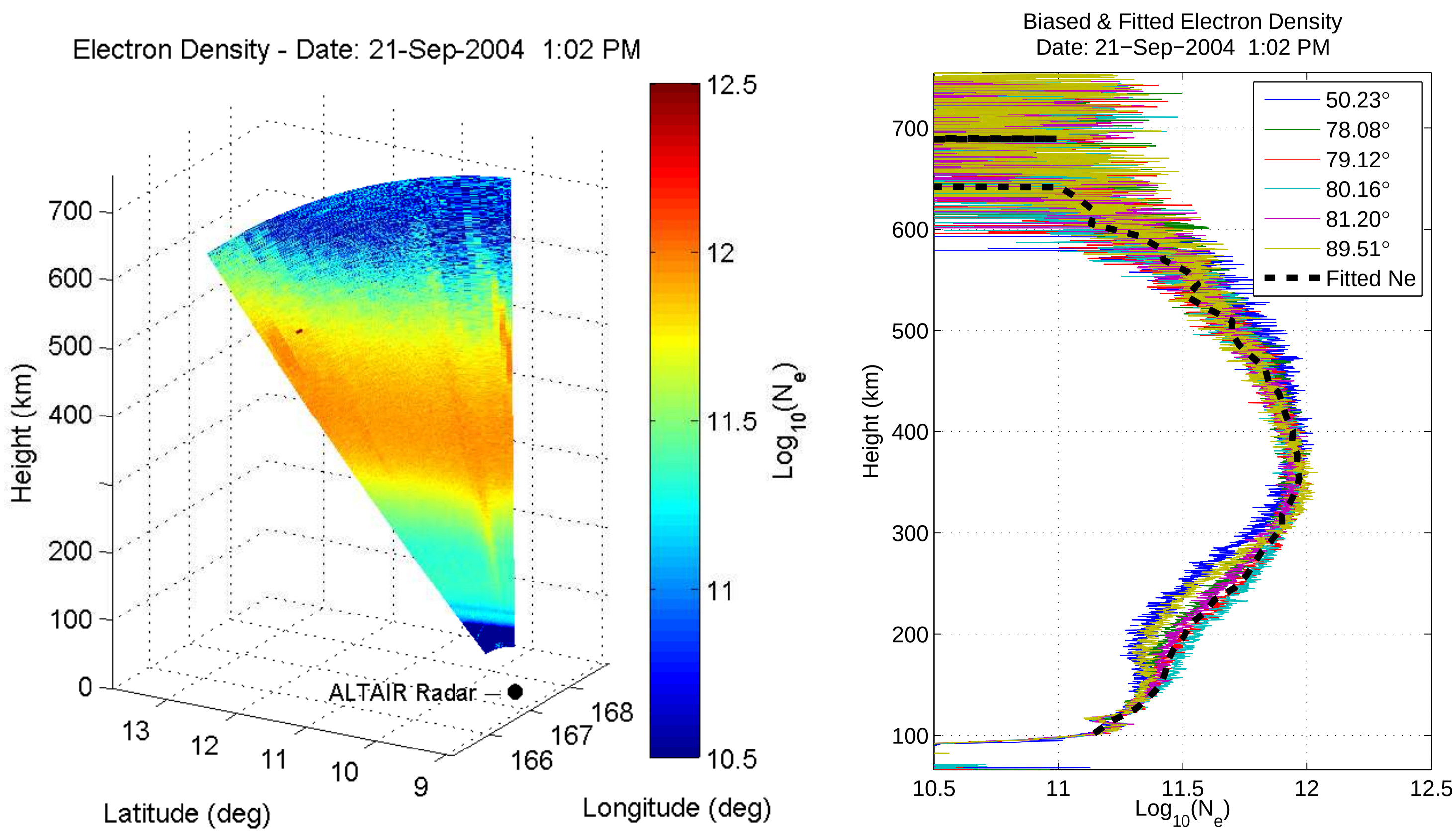

(a) (b)

Figure C.29 (a) Scan measurements and (b) electron density estimates — September 21, 2004 01:02 pm.

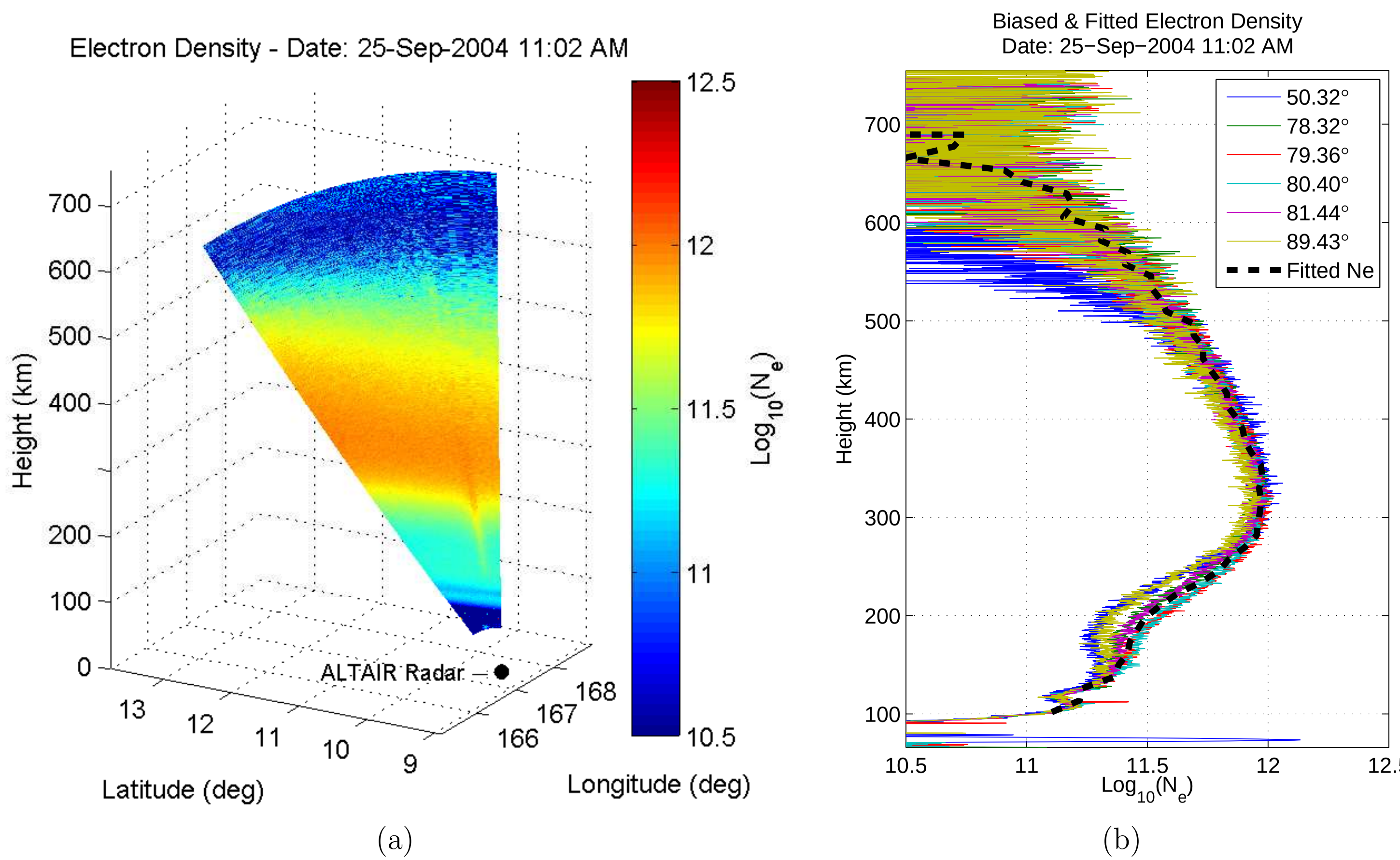

Figure C.30 (a) Scan measurements and (b) electron density estimates — September 25, 2004 11:02 am.

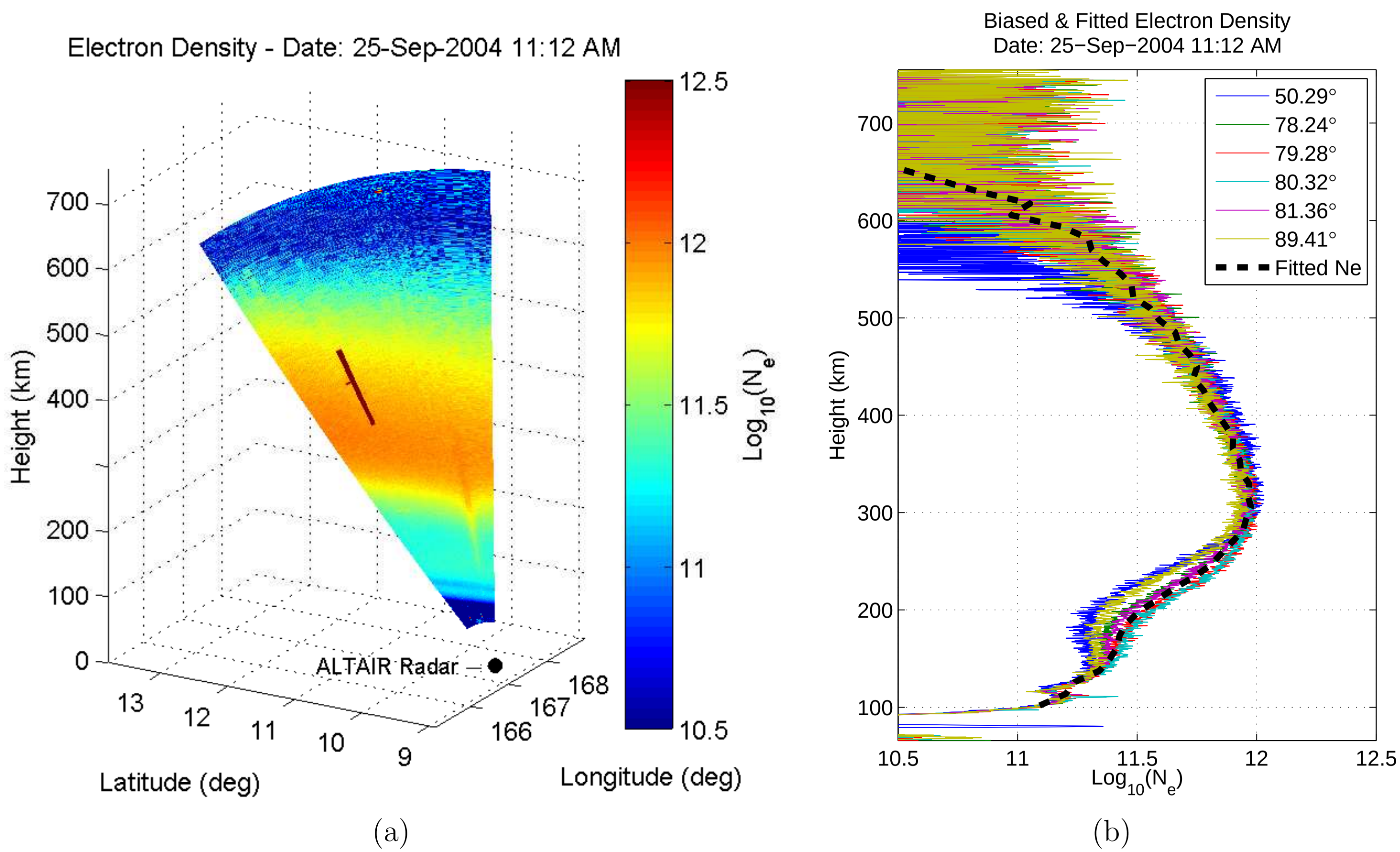

Figure C.31 (a) Scan measurements and (b) electron density estimates — September 25, 2004 11:12 am.

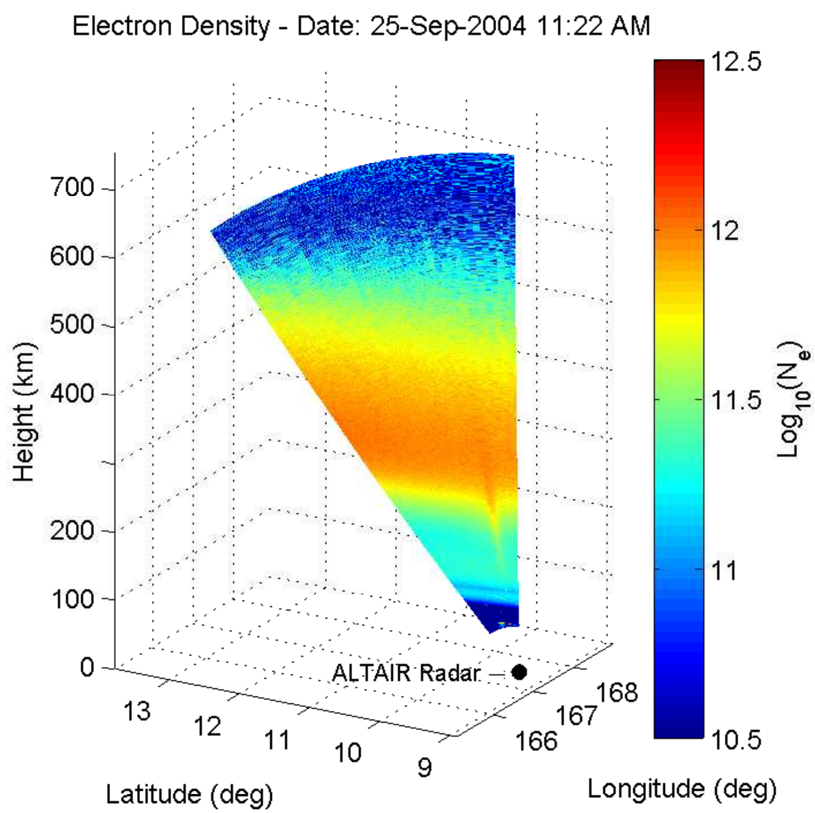

(a)

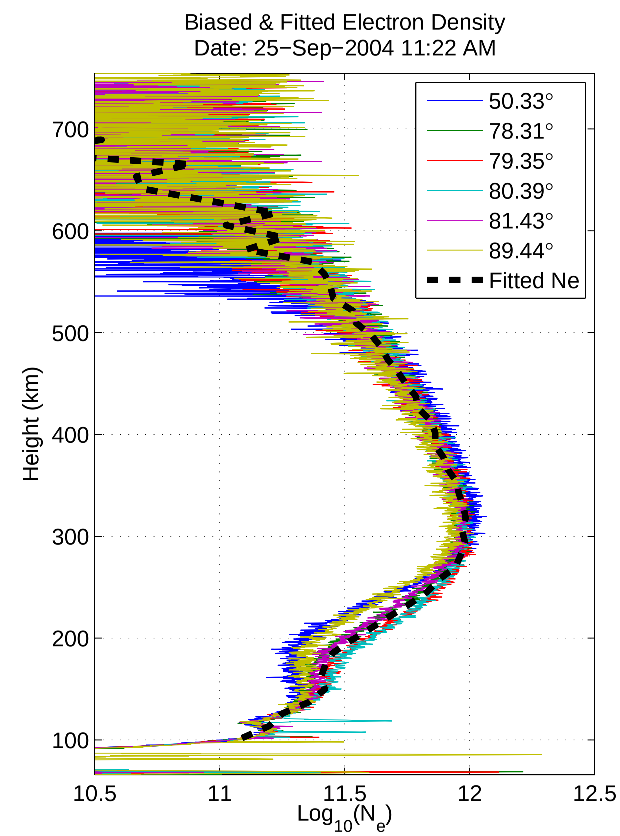

(b)

Figure C.32 (a) Scan measurements and (b) electron density estimates — September 25, 2004 11:22 am.

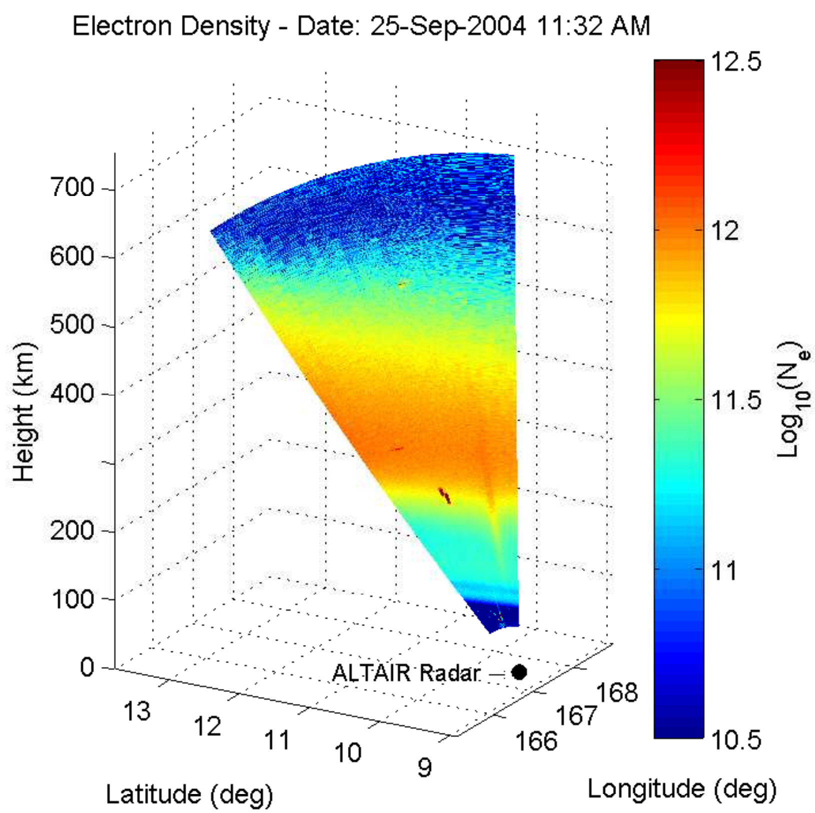

(a)

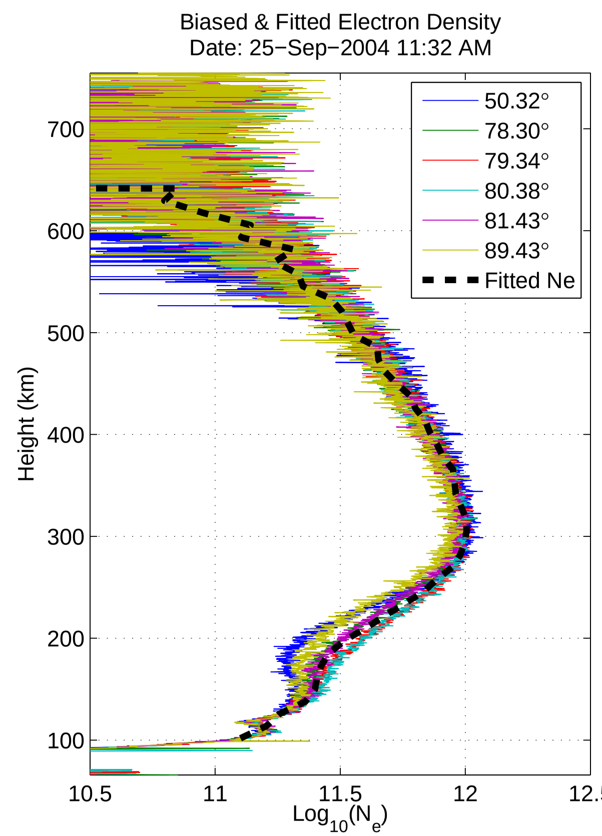

(b)

Figure C.33 (a) Scan measurements and (b) electron density estimates — September 25, 2004 11:32 am.

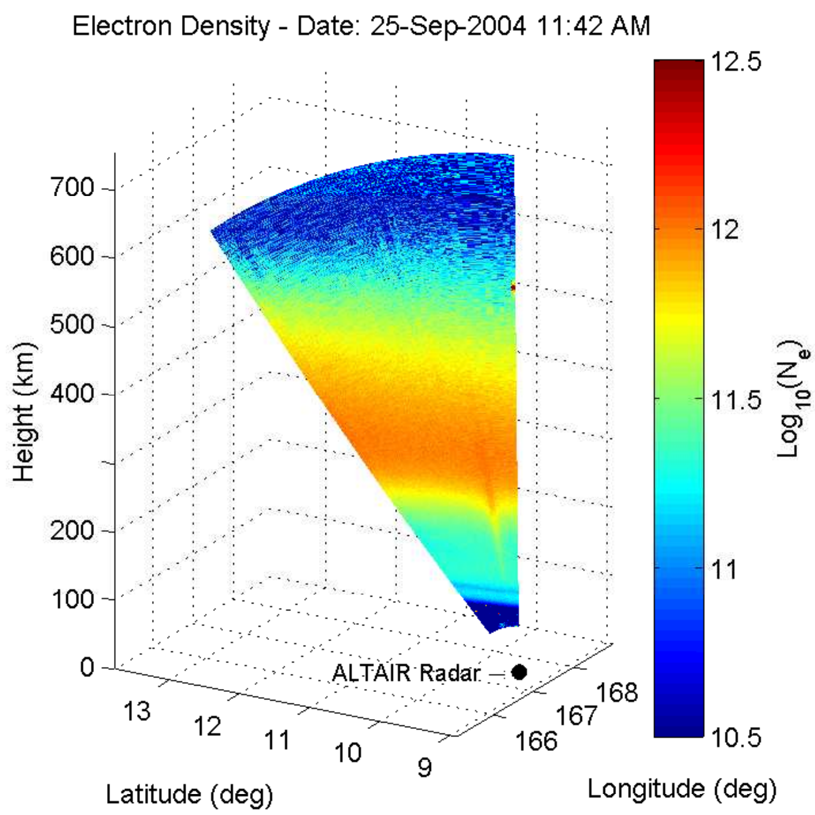

(a)

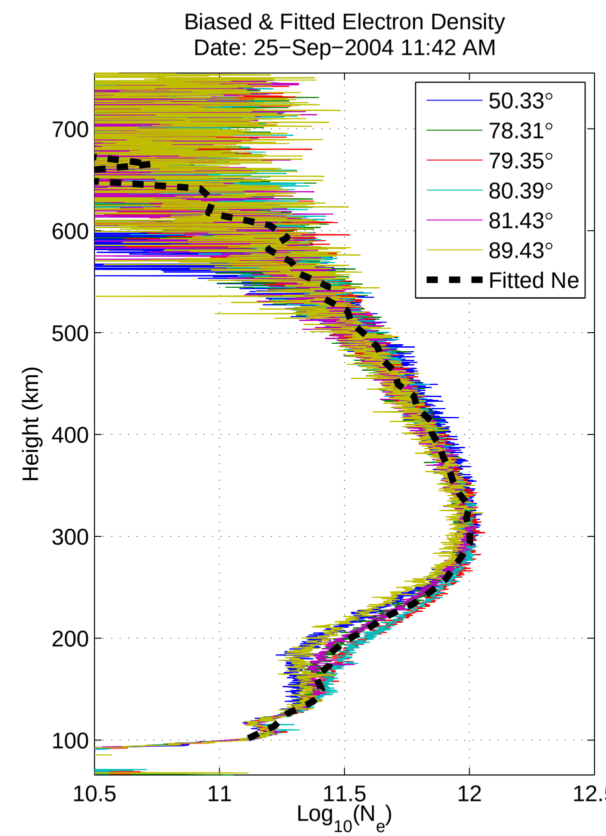

(b)

Figure C.34 (a) Scan measurements and (b) electron density estimates — September 25, 2004 11:42 am.

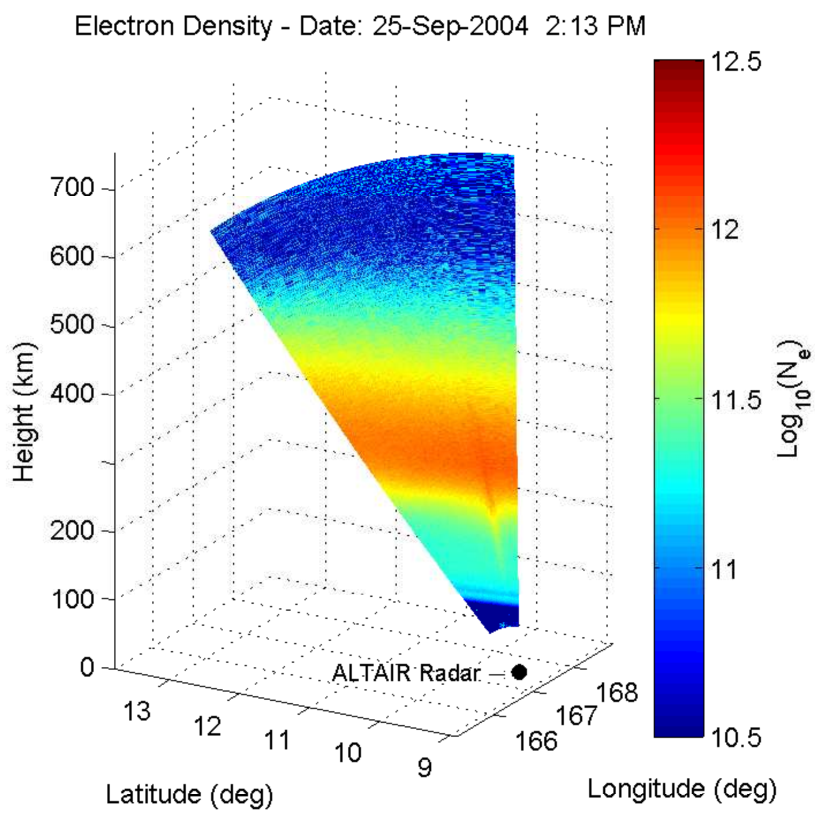

(a)

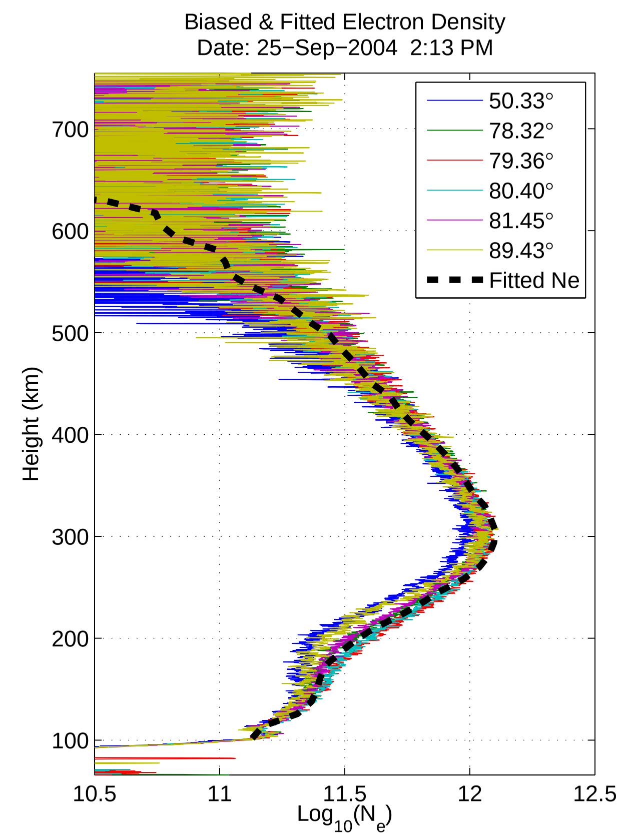

(b)

Figure C.35 (a) Scan measurements and (b) electron density estimates — September 25, 2004 02:13 pm.

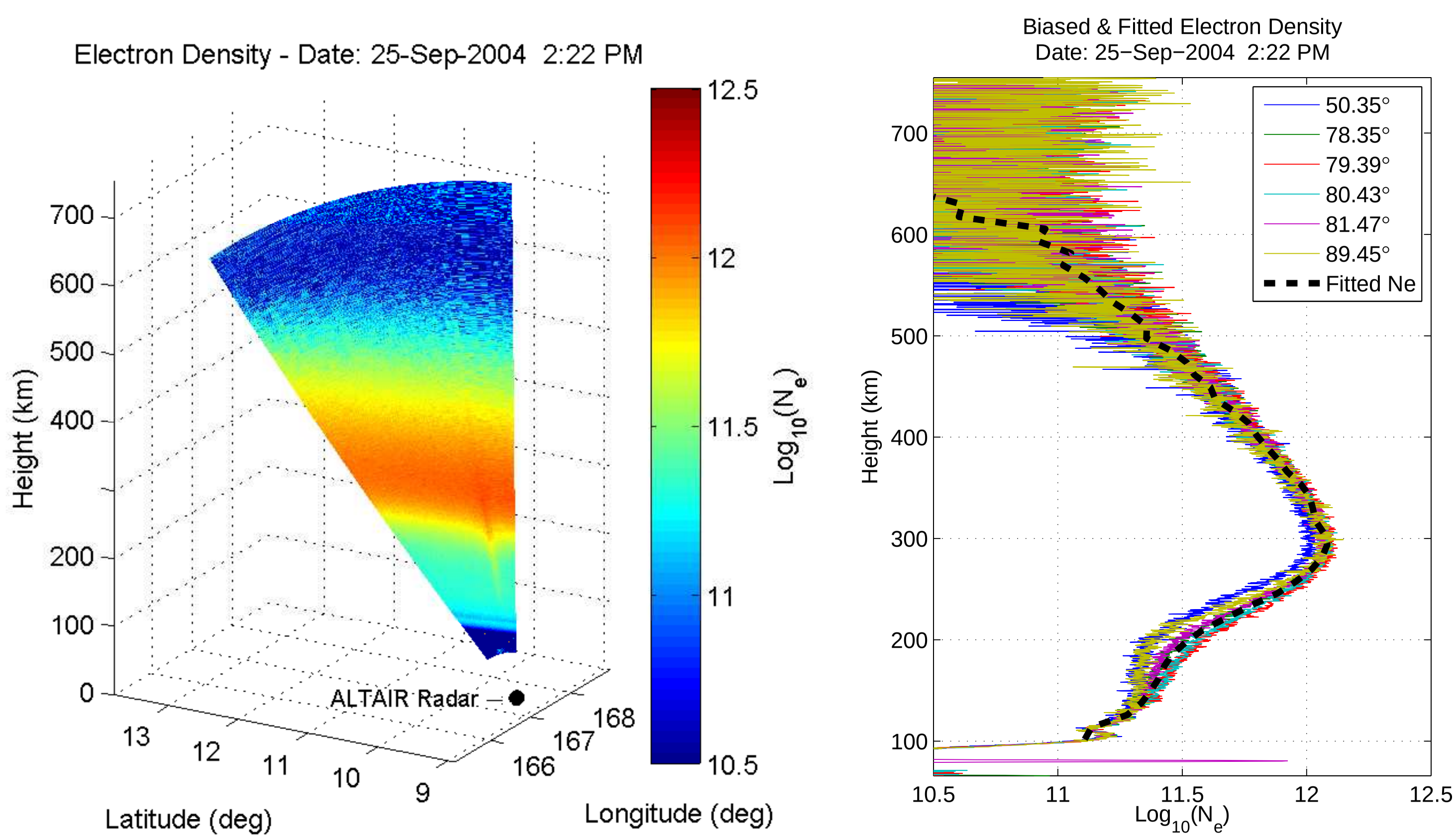

(a)

(b)

Figure C.36 (a) Scan measurements and (b) electron density estimates — September 25, 2004 02:22 pm.

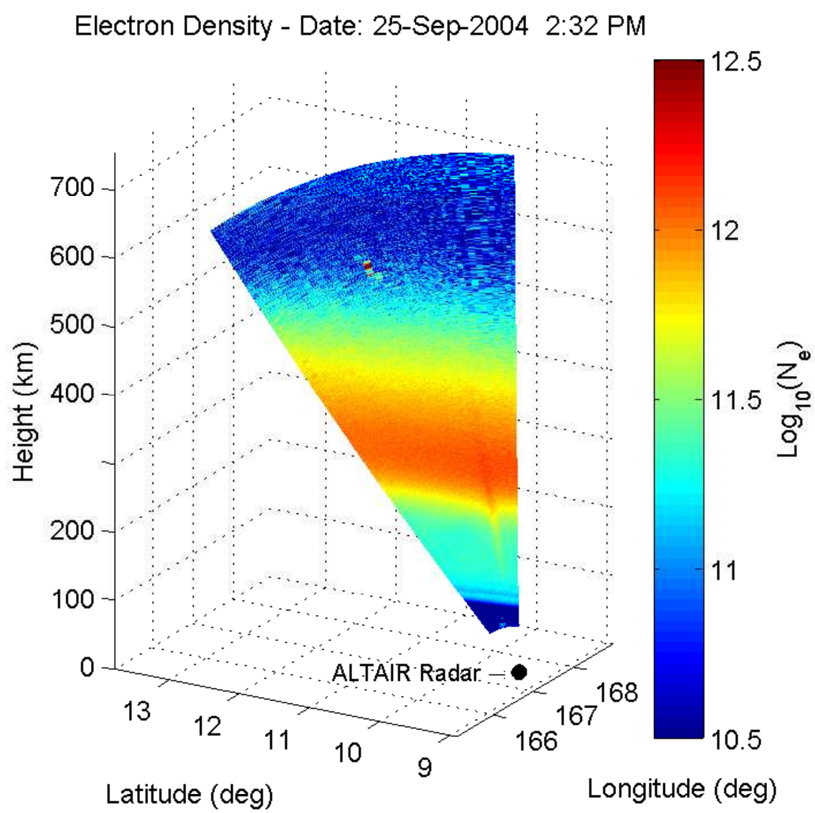

(a)

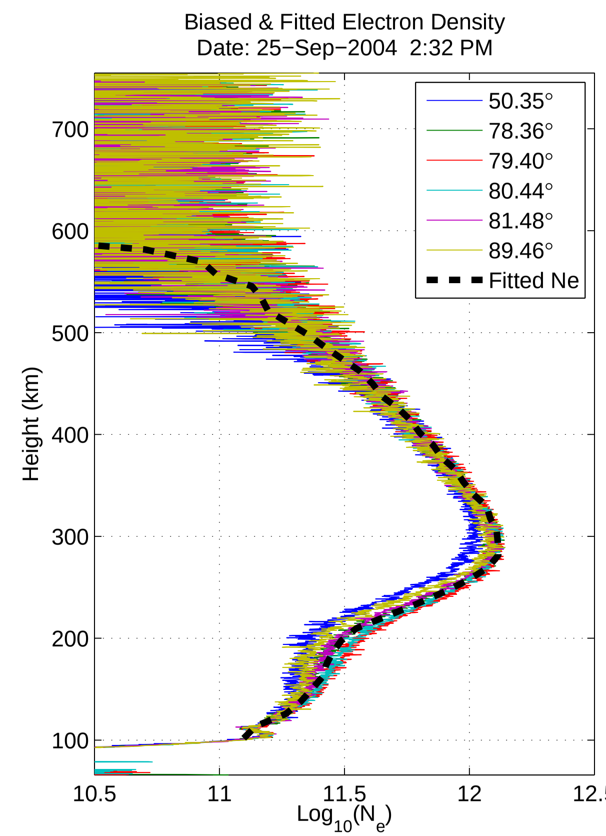

(b)

Figure C.37 (a) Scan measurements and (b) electron density estimates — September 25, 2004 02:32 pm.

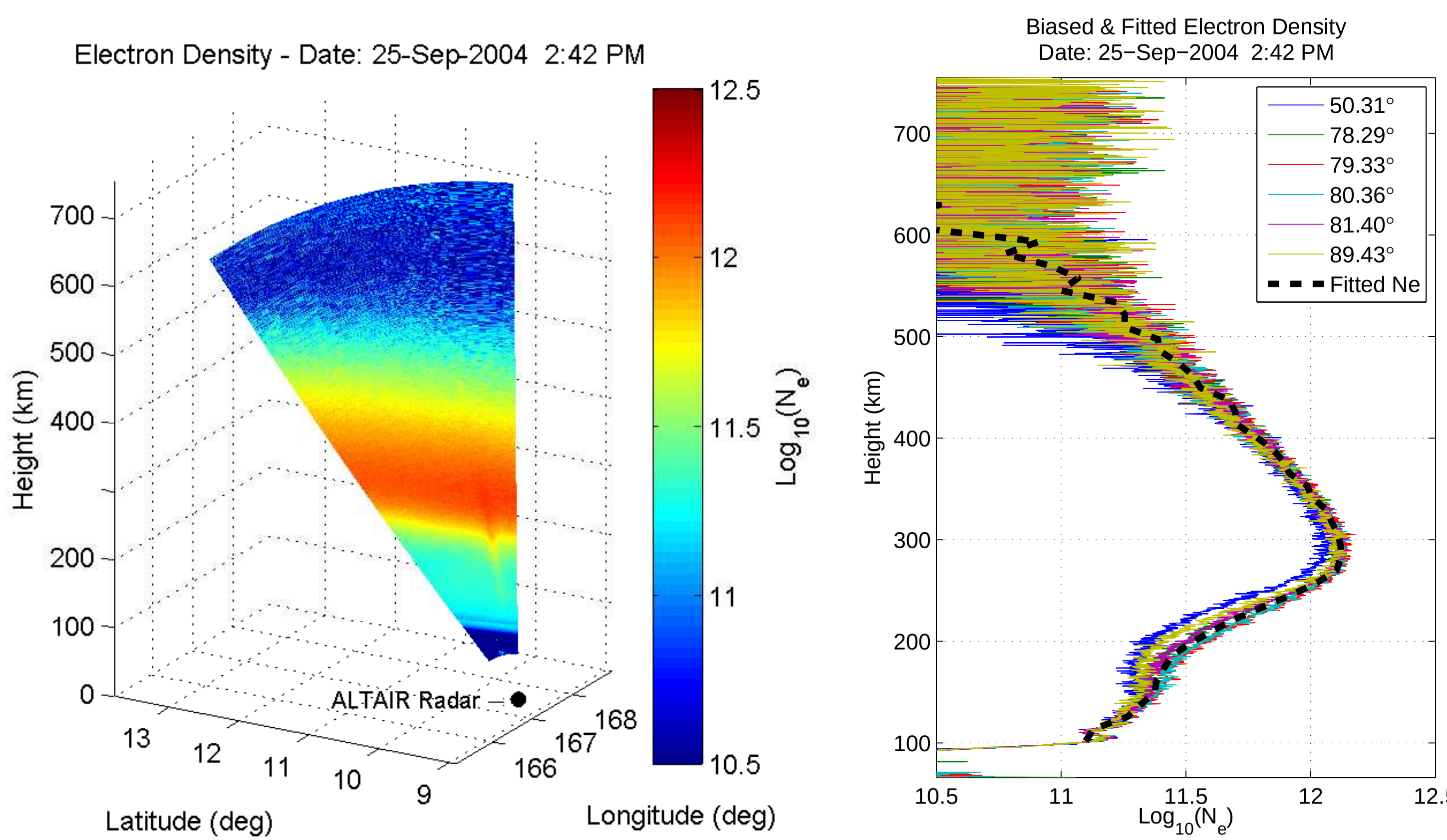

(a)

(b)

Figure C.38 (a) Scan measurements and (b) electron density estimates — September 25, 2004 02:42 pm.

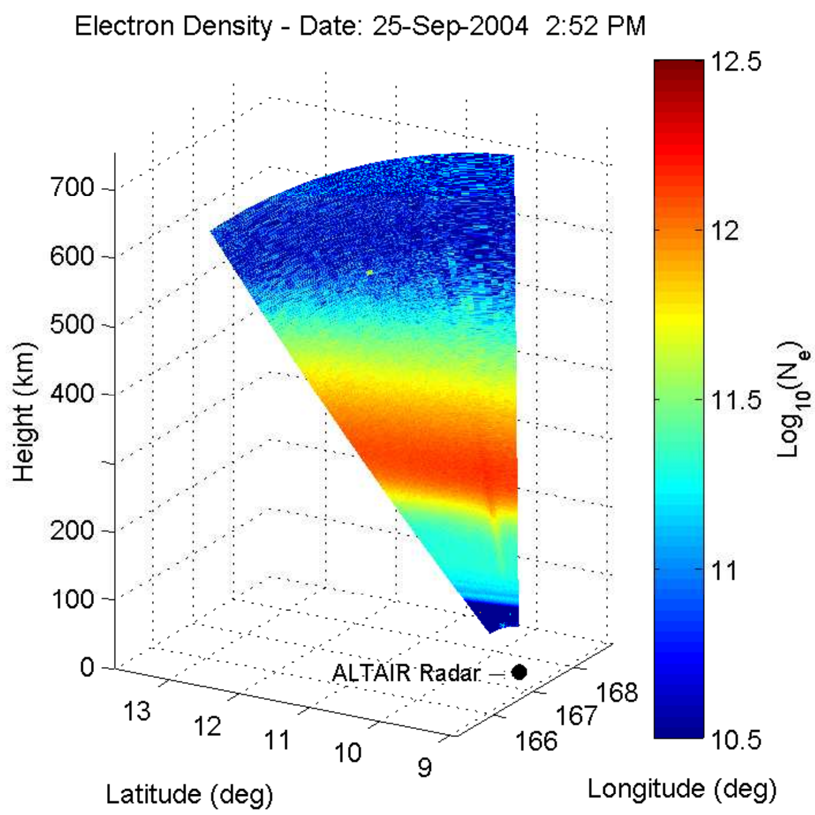

(a)

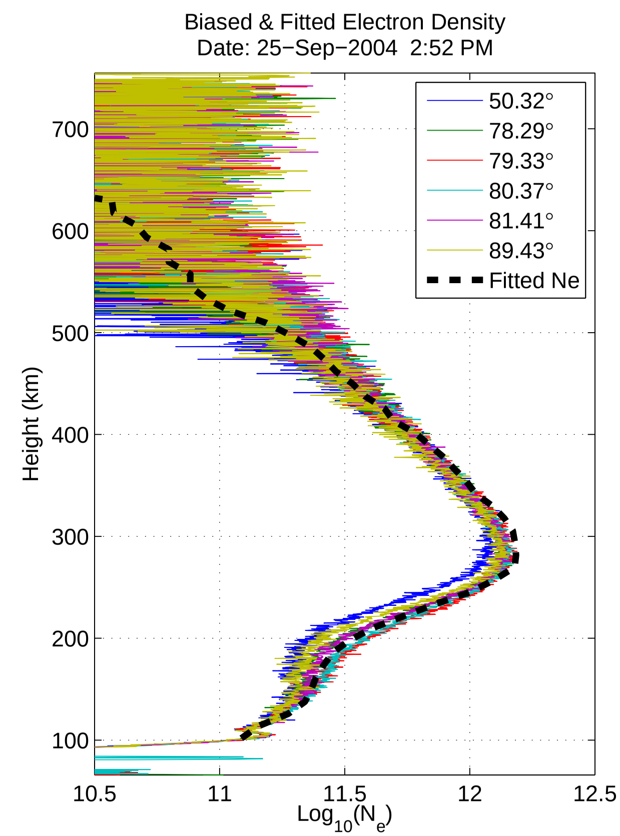

(b)

Figure C.39 (a) Scan measurements and (b) electron density estimates — September 25, 2004 02:52 pm.

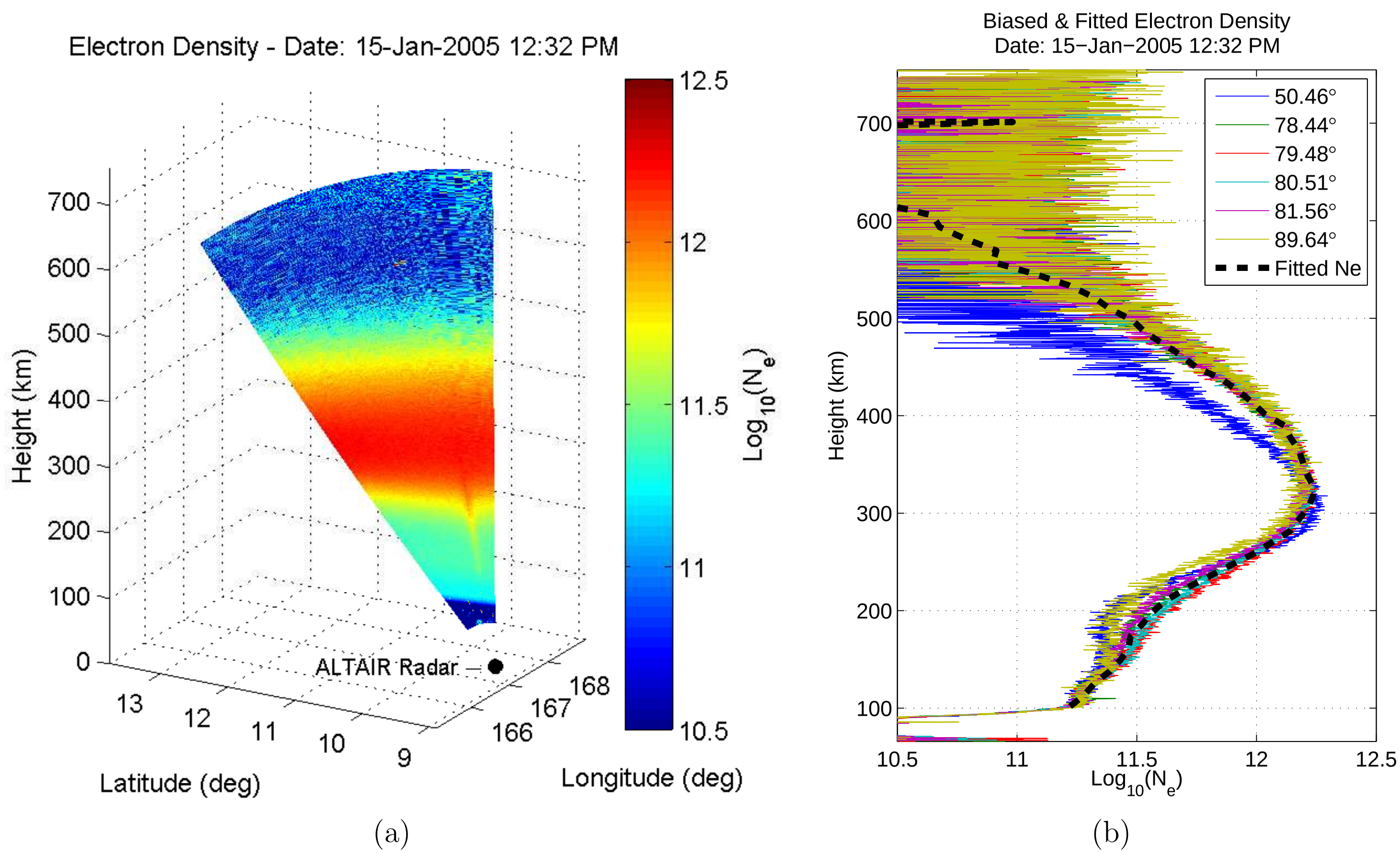

(a) (b)

Figure C.40 (a) Scan measurements and (b) electron density estimates — January 15, 2005 12:32 pm.

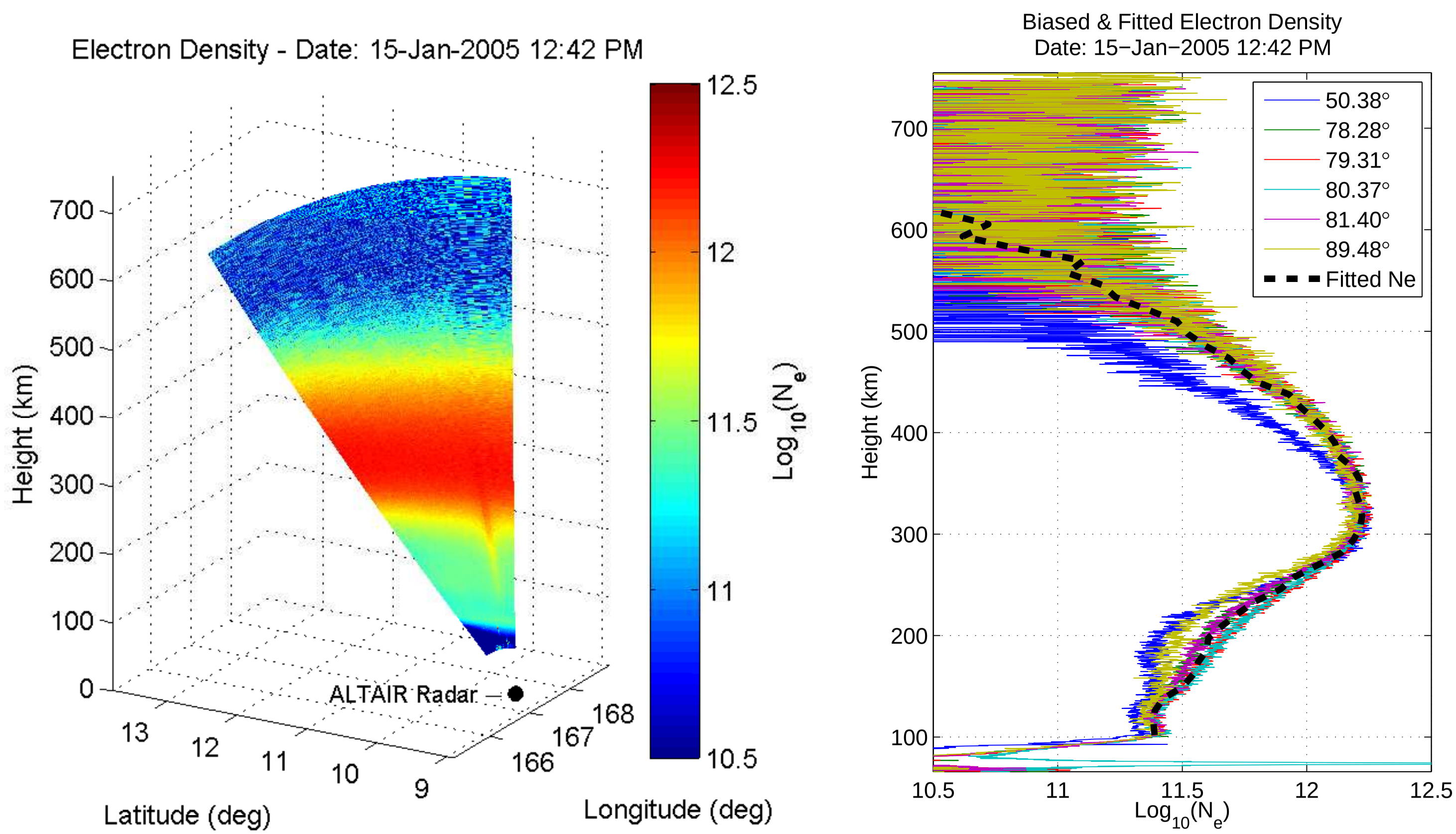

(a) (b)

Figure C.41 (a) Scan measurements and (b) electron density estimates — January 15, 2005 12:42 pm.

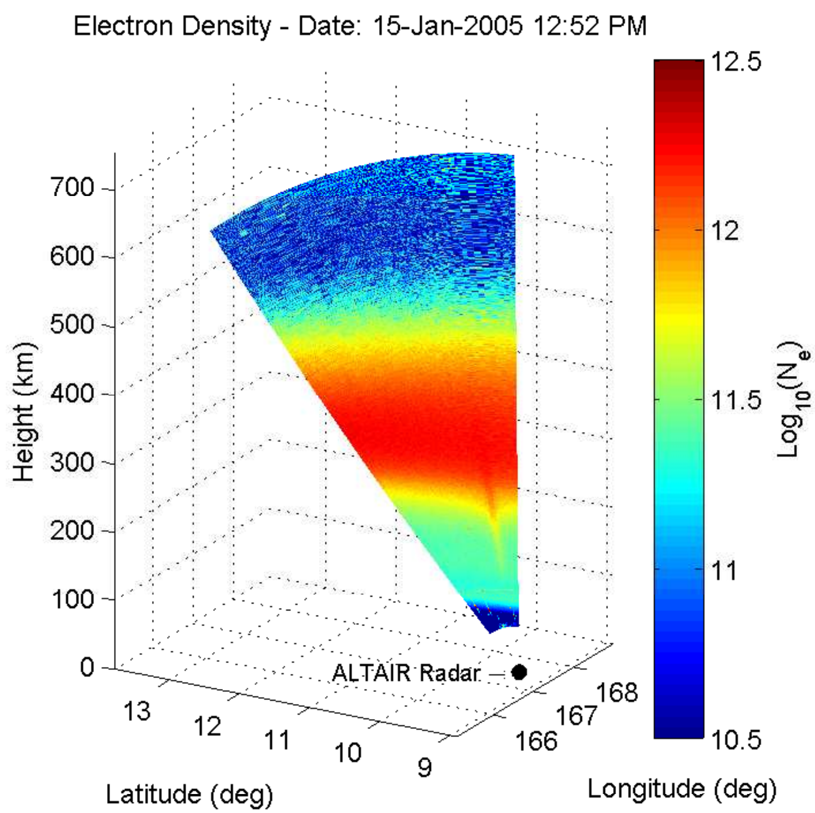

(a)

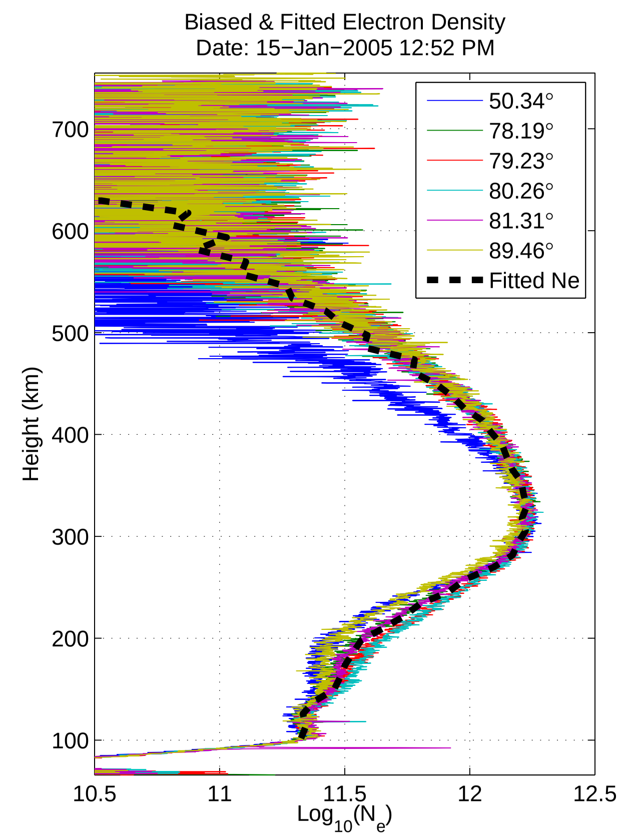

(b)

Figure C.42 (a) Scan measurements and (b) electron density estimates — January 15, 2005 12:52 pm.

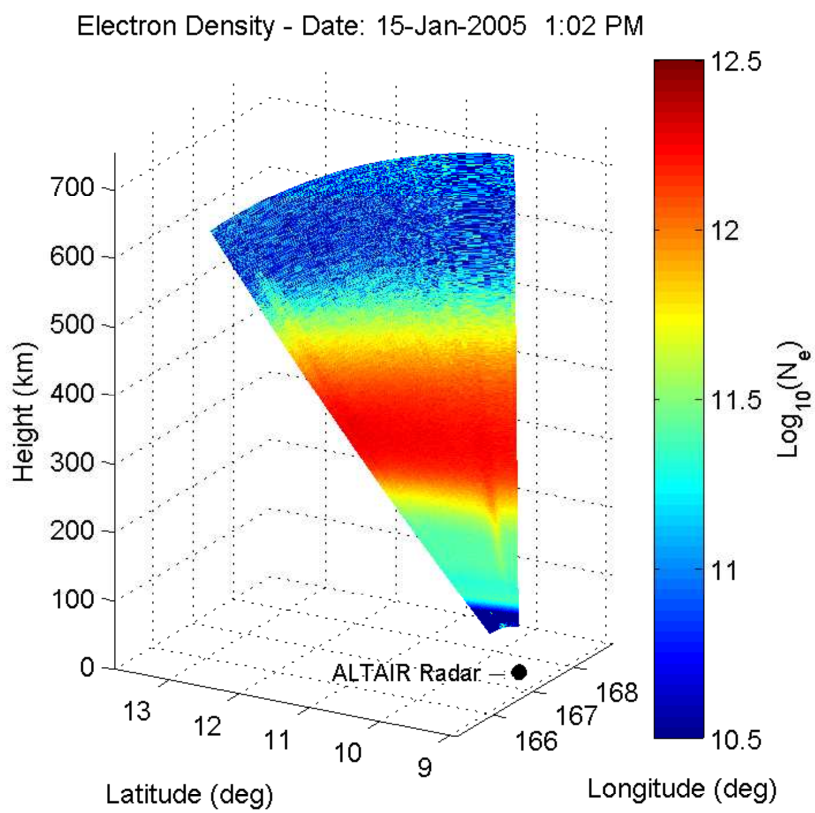

(a)

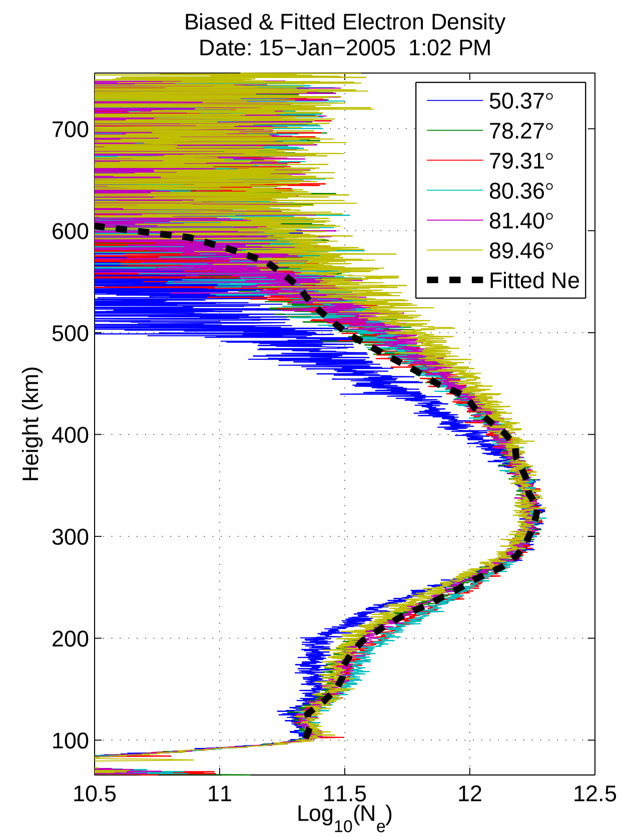

(b)

Figure C.43 (a) Scan measurements and (b) electron density estimates — January 15, 2005 01:02 pm.

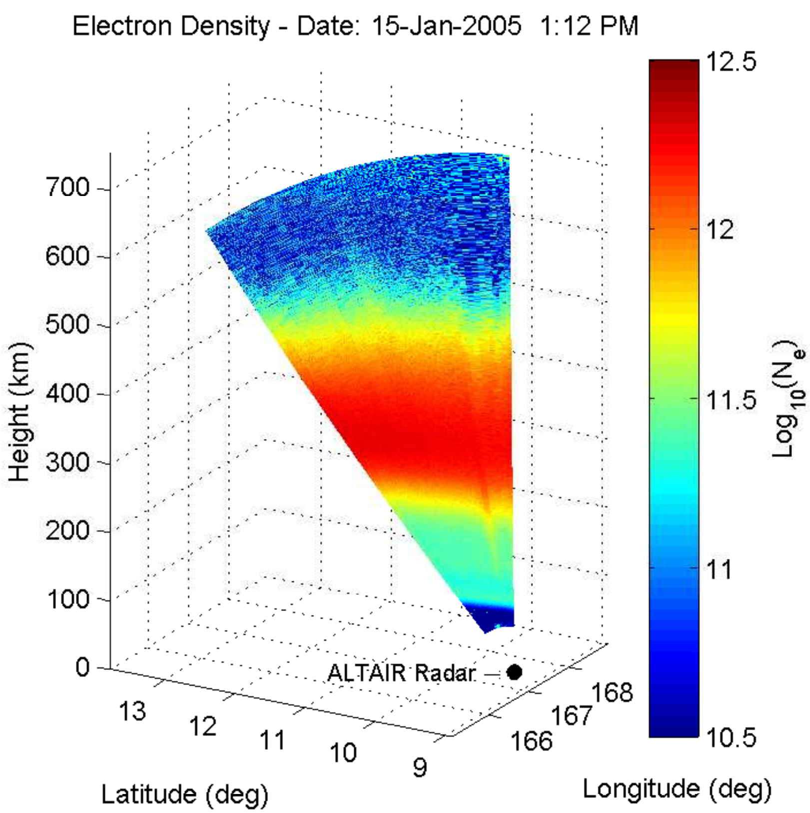

(a)

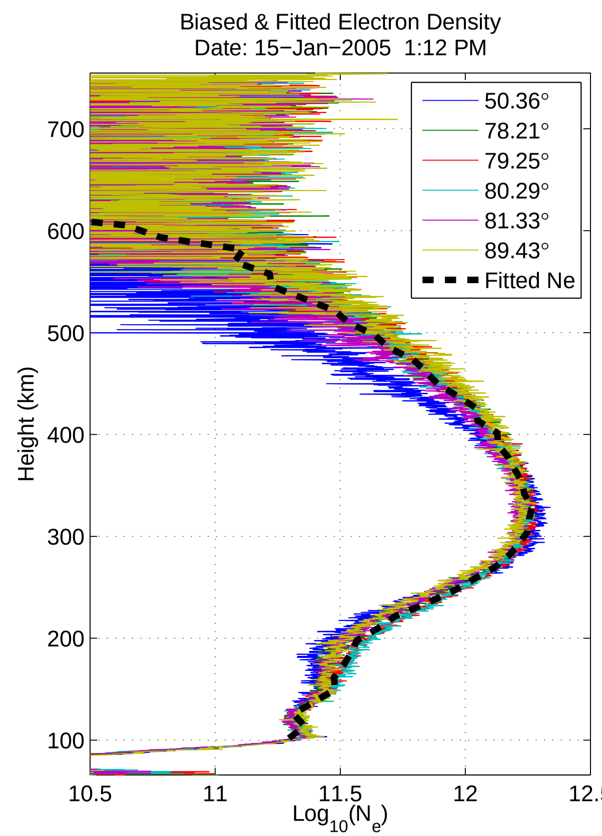

(b)

Figure C.44 (a) Scan measurements and (b) electron density estimates — January 15, 2005 01:12 pm.

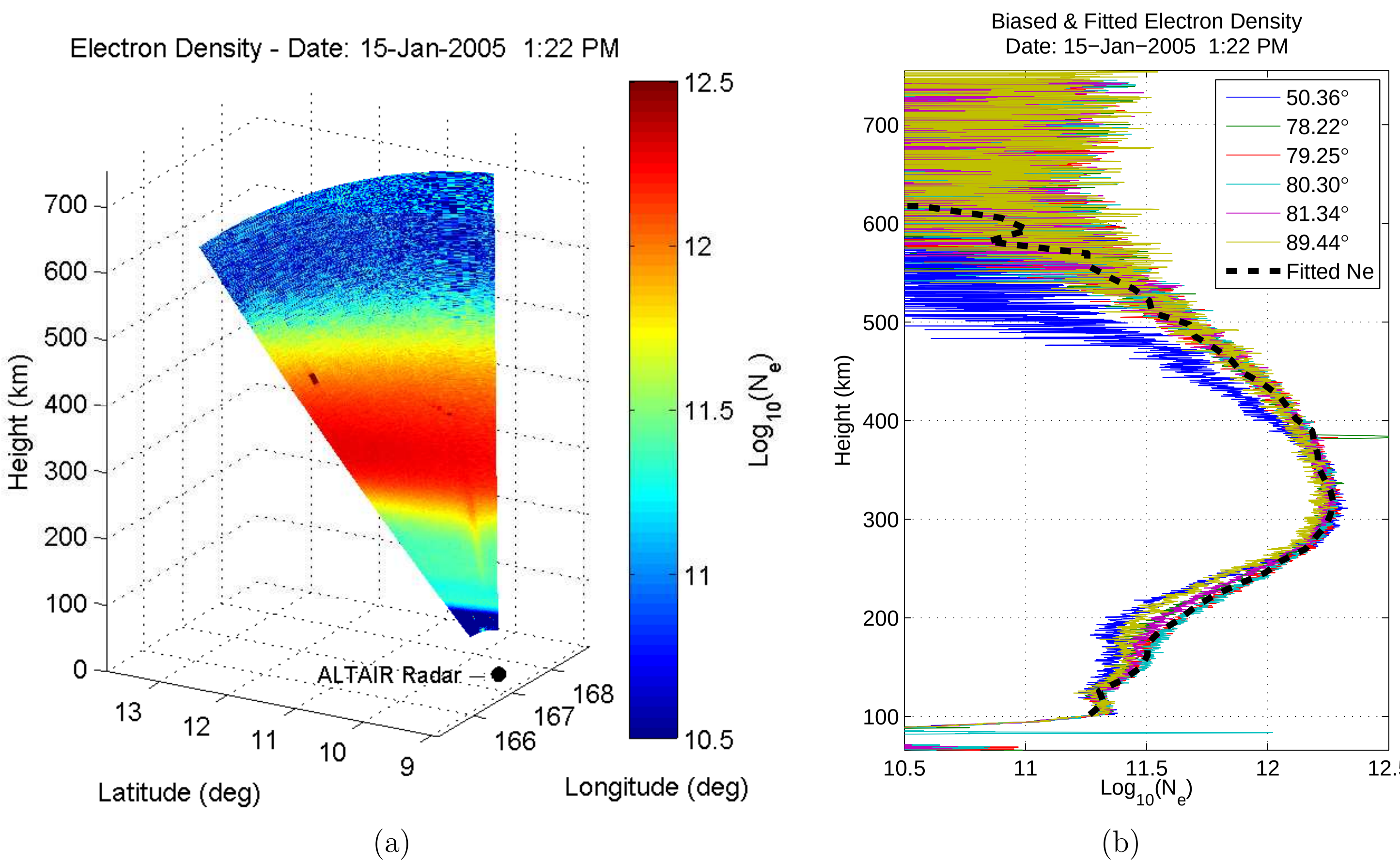

Figure C.45 (a) Scan measurements and (b) electron density estimates — January 15, 2005 01:22 pm.

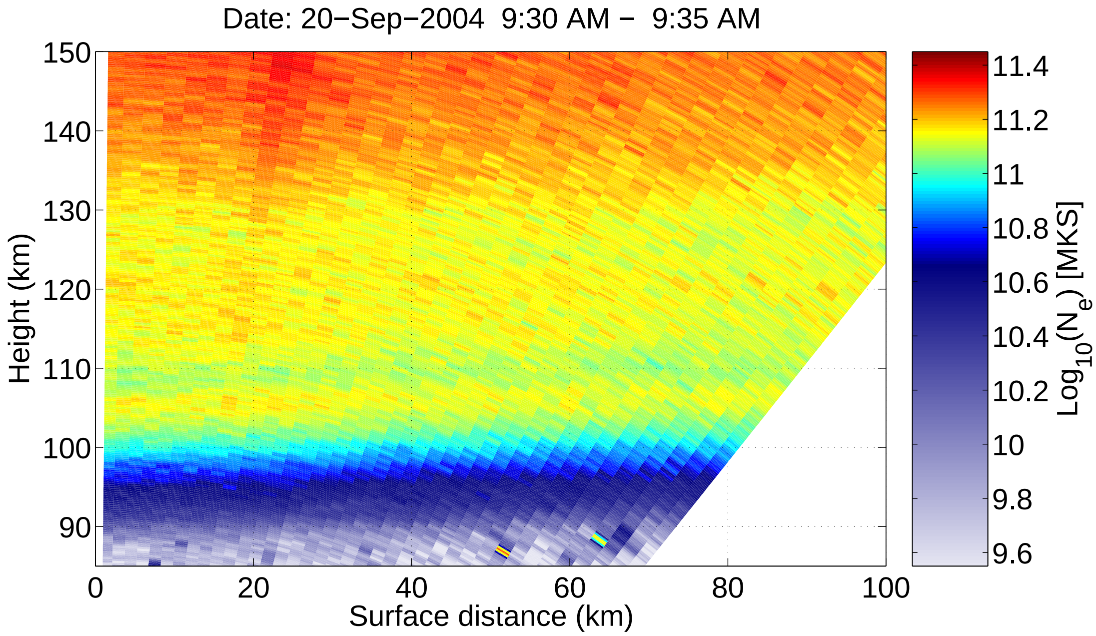

Figure C.46 E-region density map — September 20, 2004 09:30 am - 09:35 am.

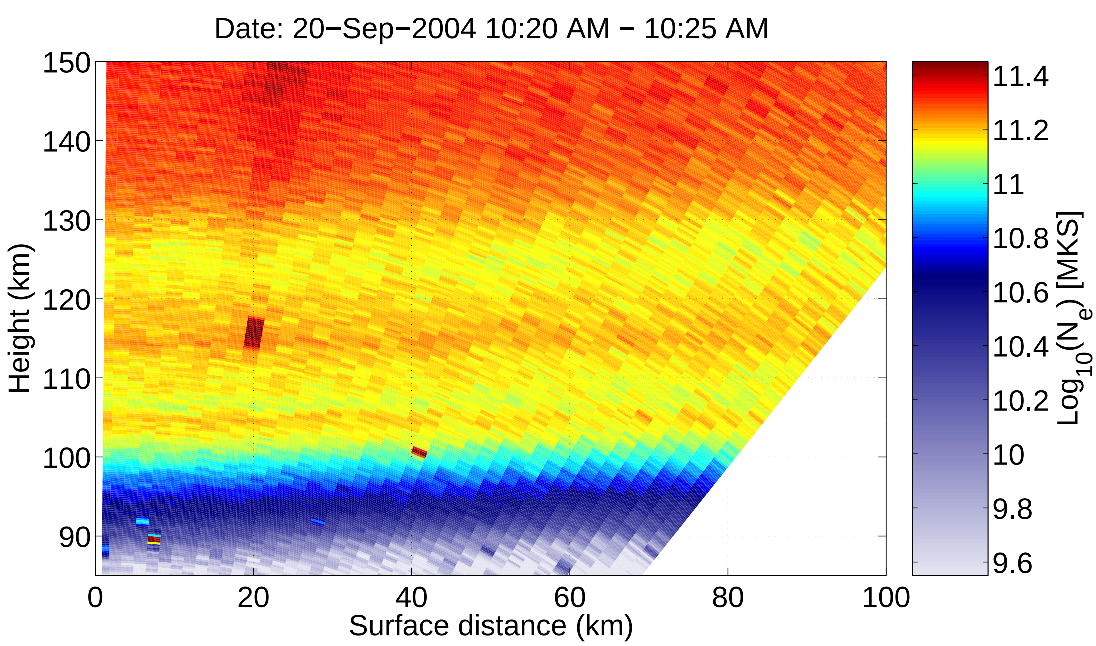

Figure C.47 E-region density map — September 20, 2004 10:20 am - 10:25 am.

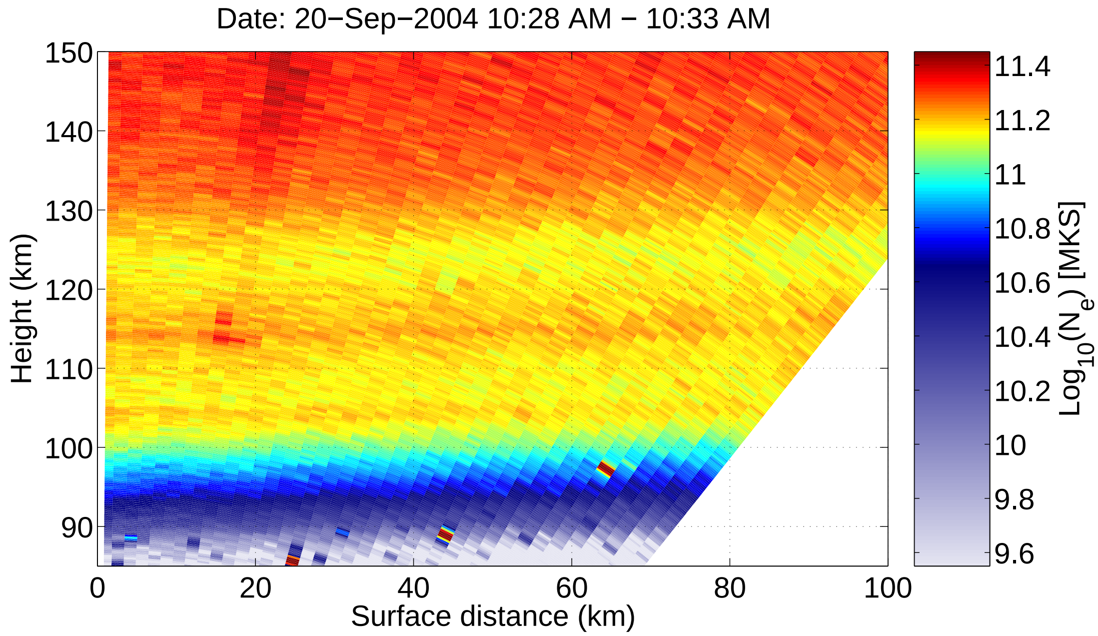

Figure C.48 E-region density map — September 20, 2004 10:28 am - 10:33 am.

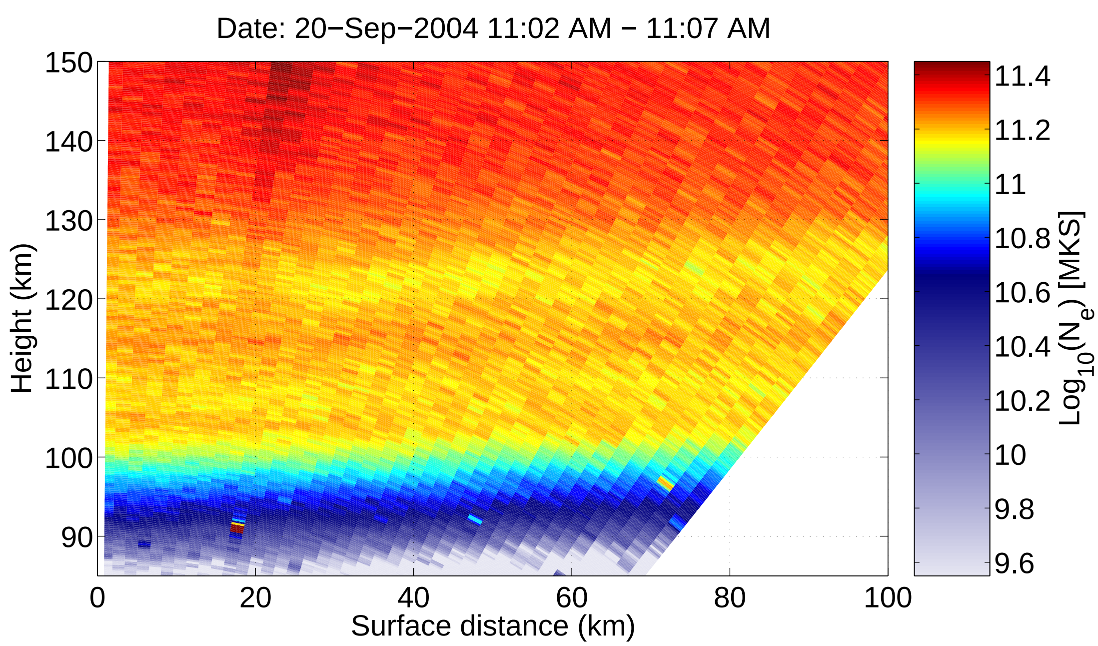

Figure C.49 E-region density map — September 20, 2004 11:02 am - 11:07 am.

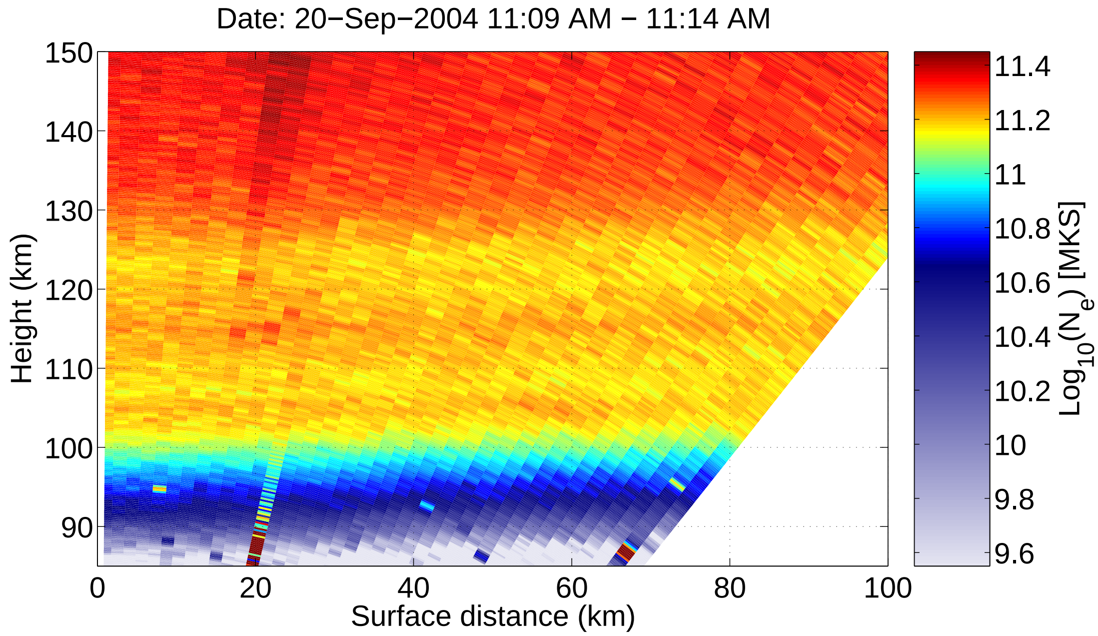

Figure C.50 E-region density map — September 20, 2004 11:09 am - 11:14 am.

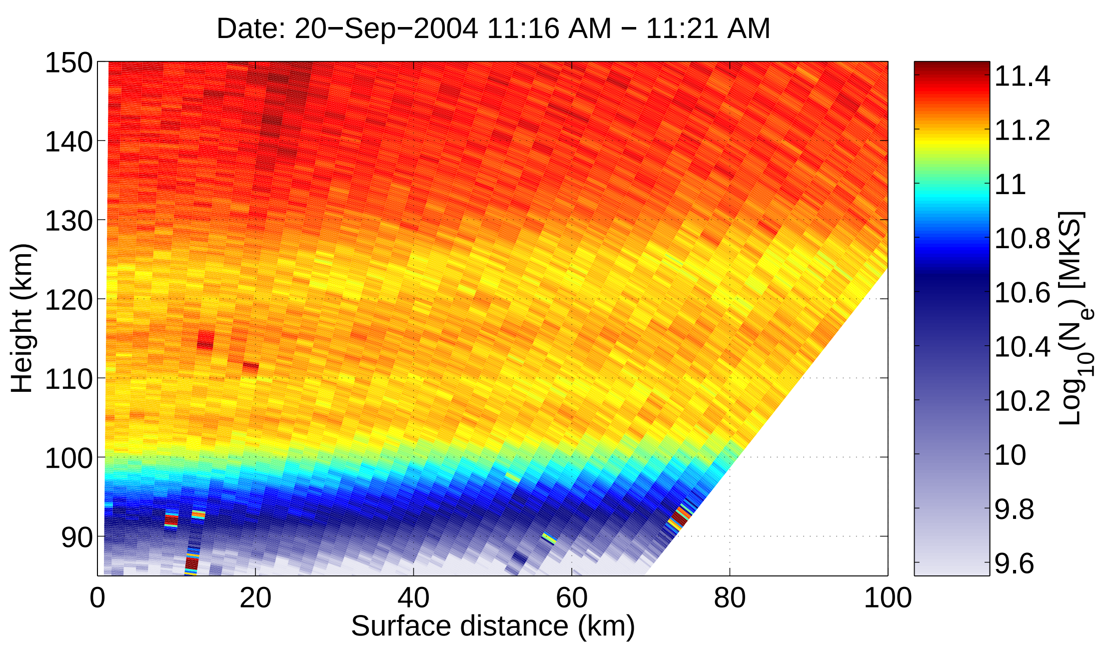

Figure C.51 E-region density map — September 20, 2004 11:16 am - 11:21 am.

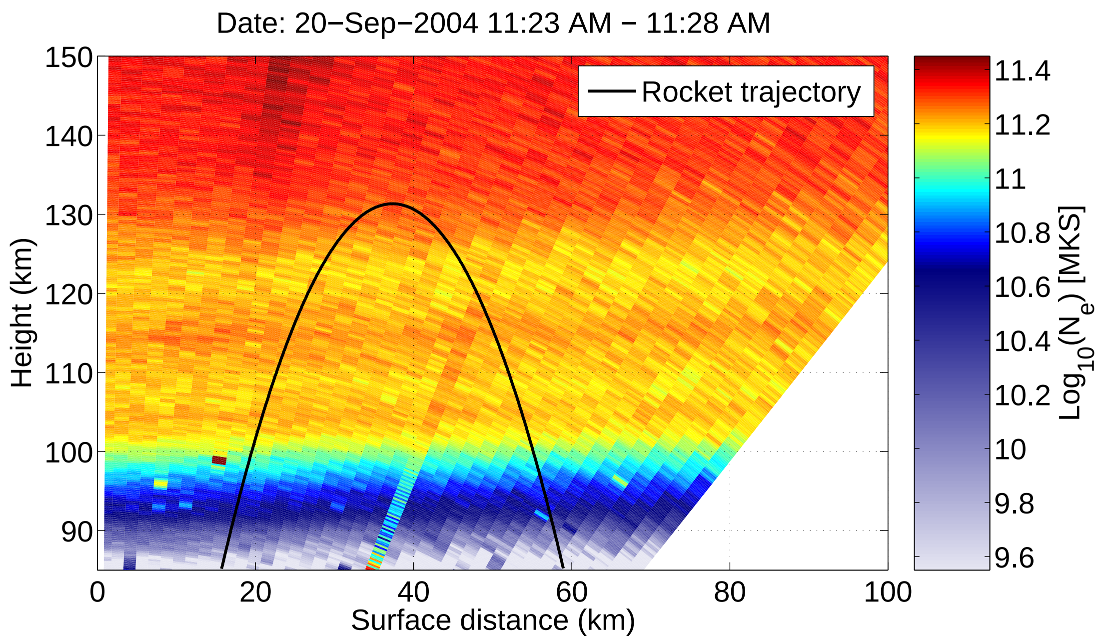

Figure C.52 E-region density map — September 20, 2004 11:23 am - 11:28 am.

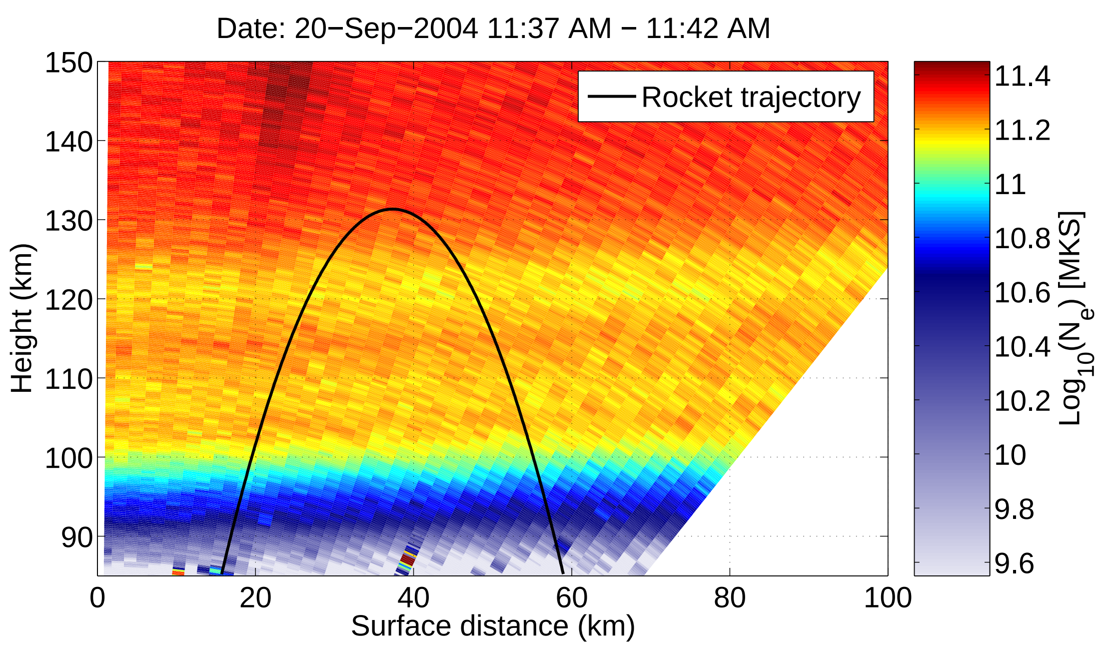

Figure C.53 E-region density map — September 20, 2004 11:37 am - 11:42 am.

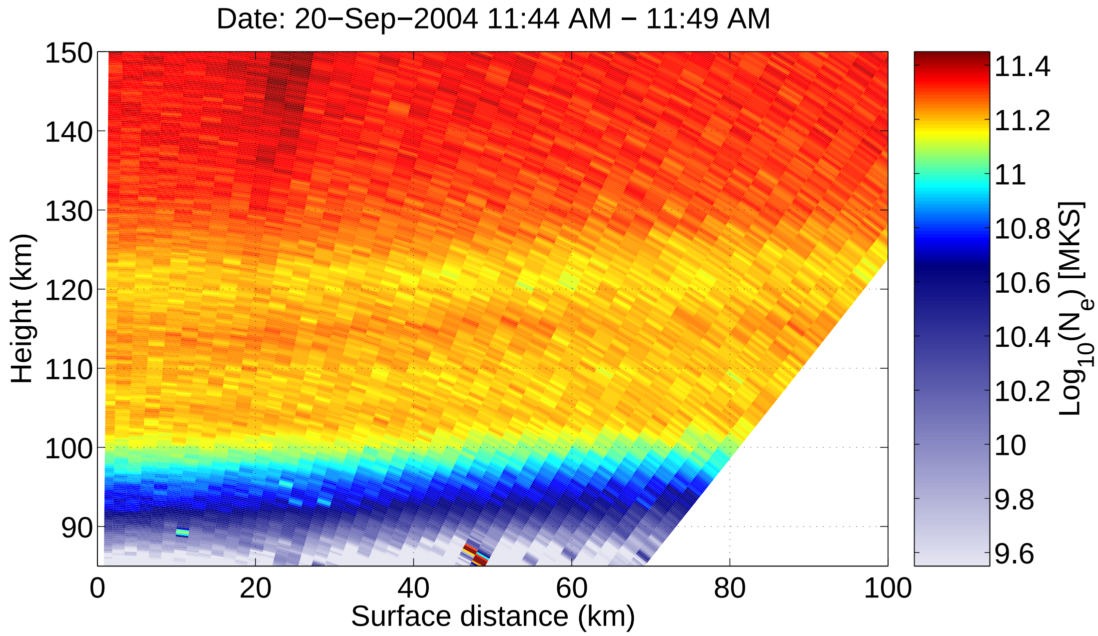

Figure C.54 E-region density map — September 20, 2004 11:44 am - 11:49 am.

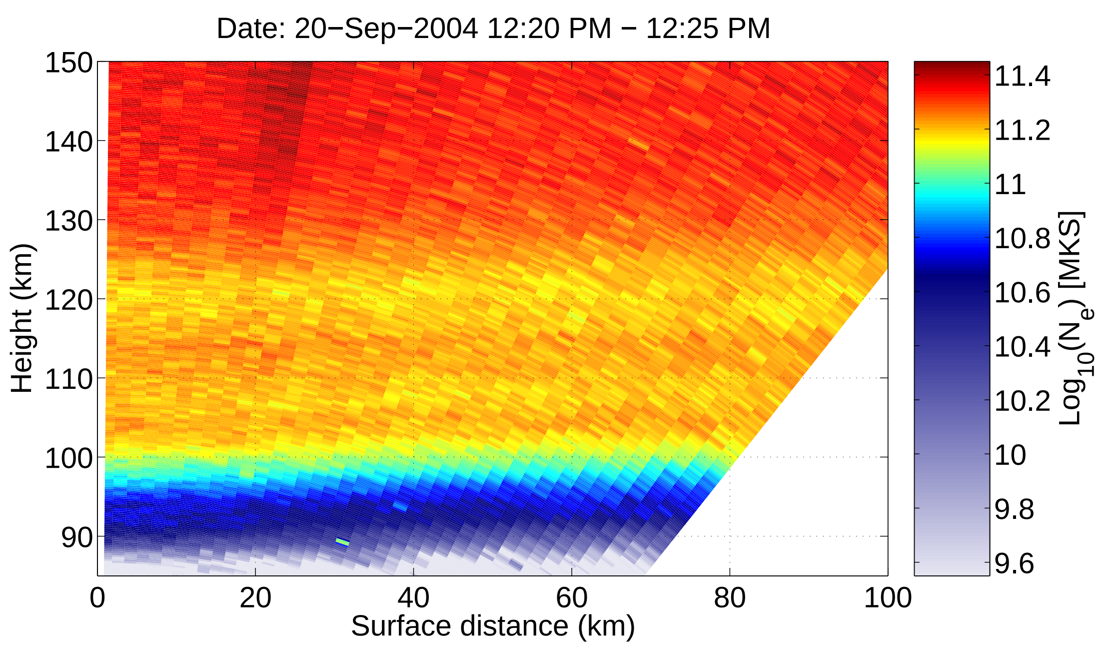

Figure C.55 E-region density map — September 20, 2004 12:20 pm - 12:25 pm.

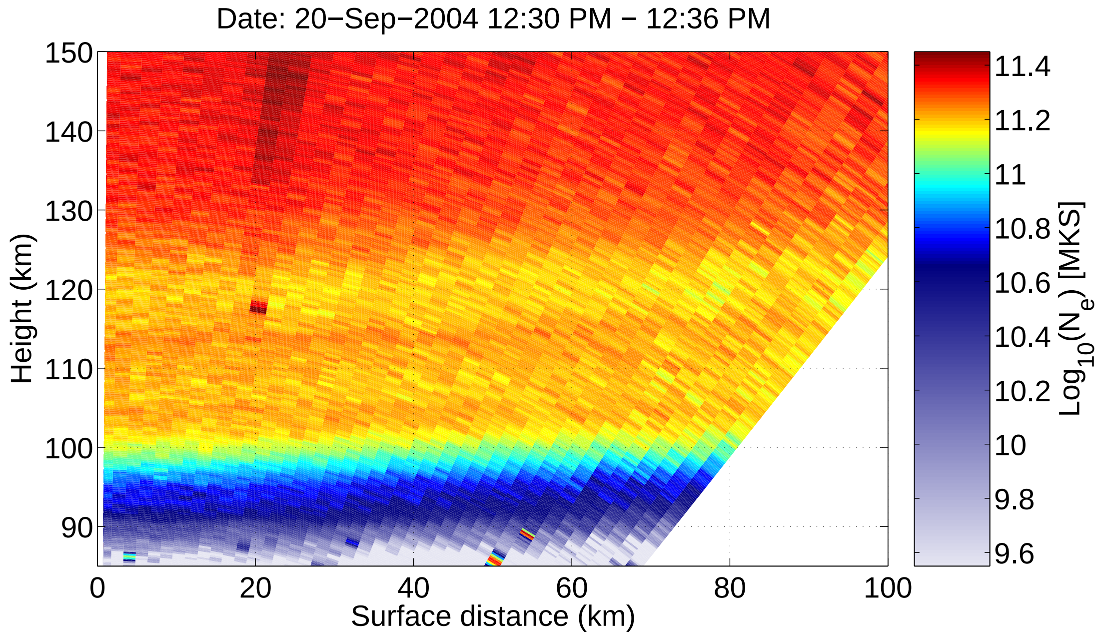

Figure C.56 E-region density map — September 20, 2004 12:30 pm - 12:36 pm.

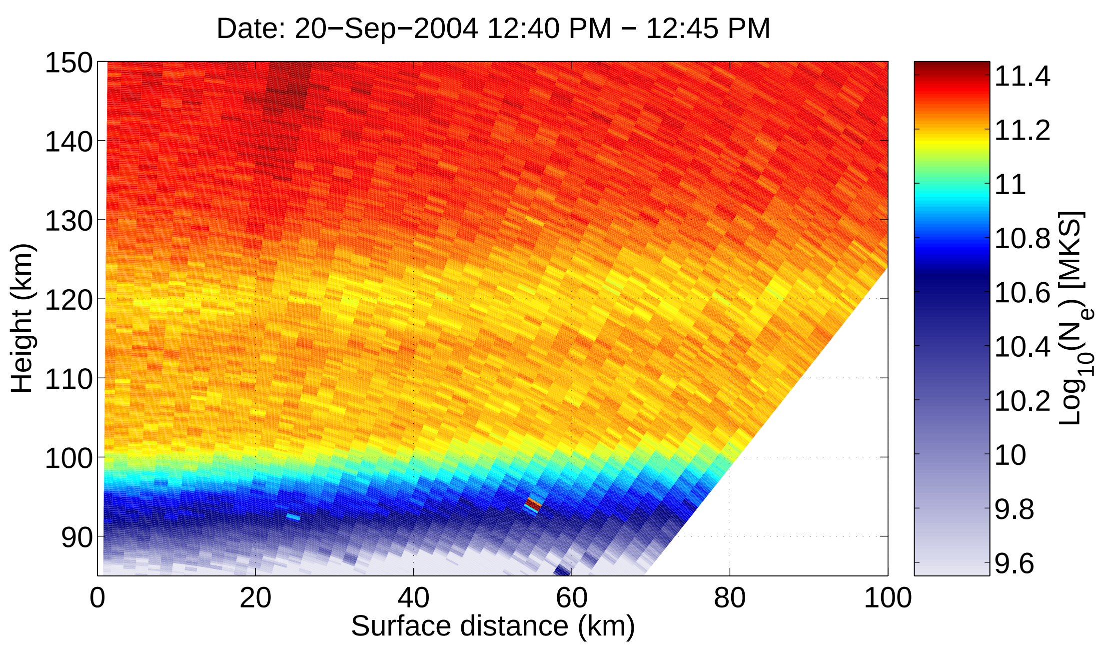

Figure C.57 E-region density map — September 20, 2004 12:40 pm - 12:45 pm.

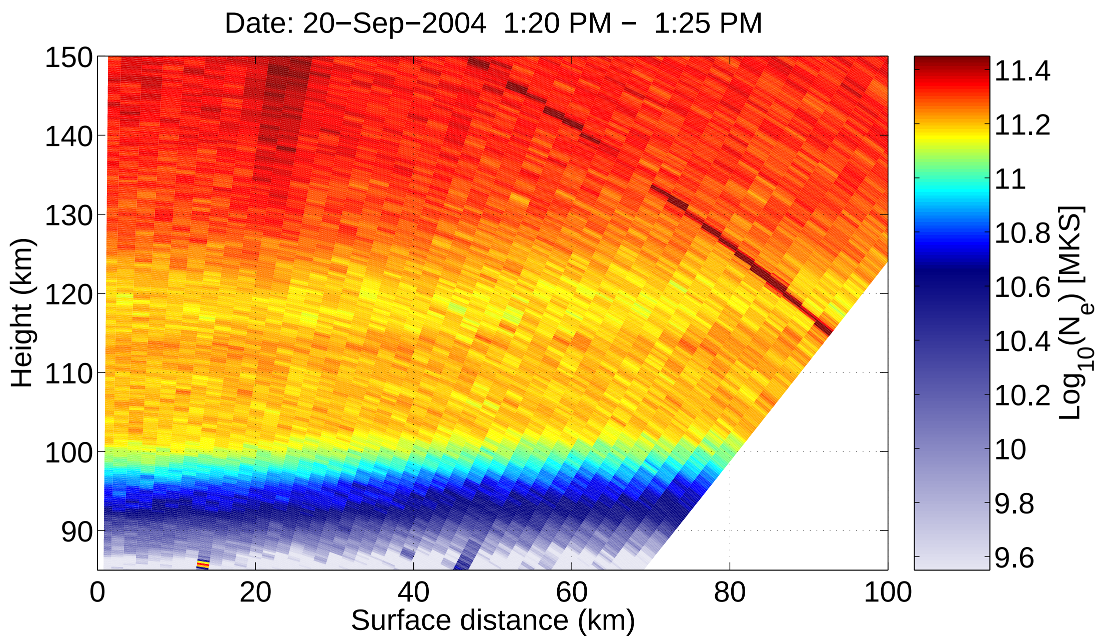

Figure C.58 E-region density map — September 20, 2004 01:20 pm - 01:25 pm.

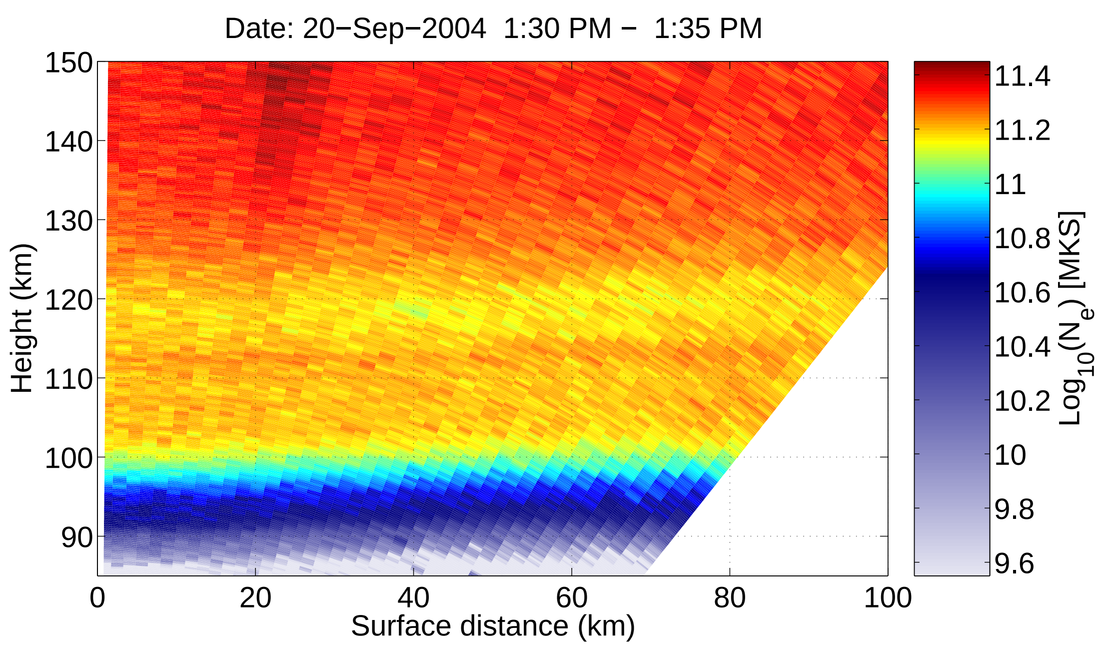

Figure C.59 E-region density map — September 20, 2004 01:30 pm - 01:35 pm.

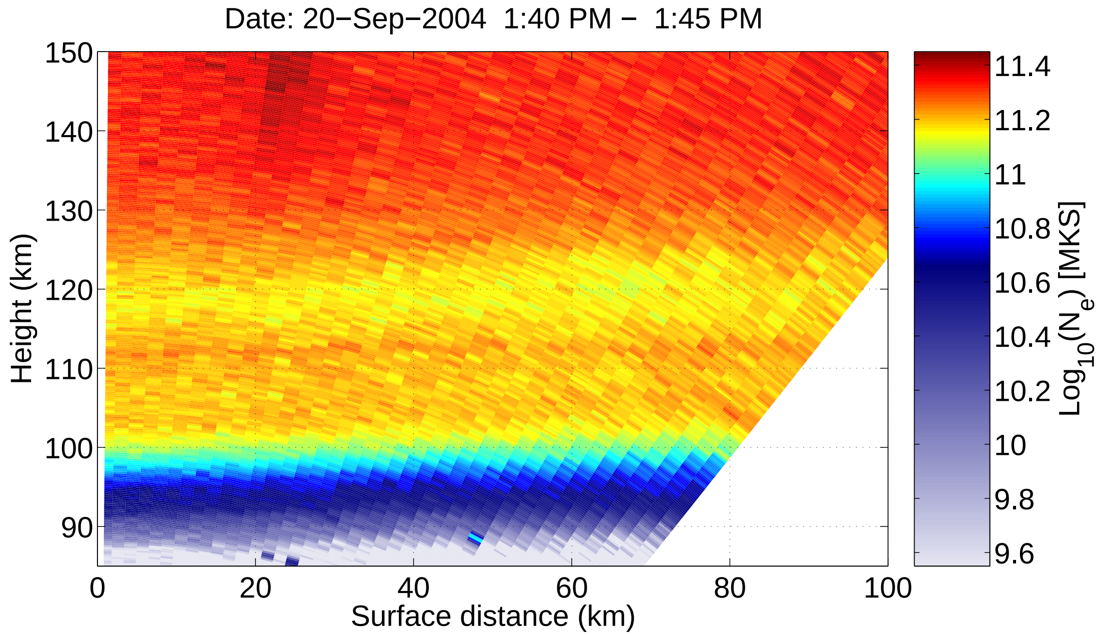

Figure C.60 E-region density map — September 20, 2004 01:40 pm - 01:45 pm.

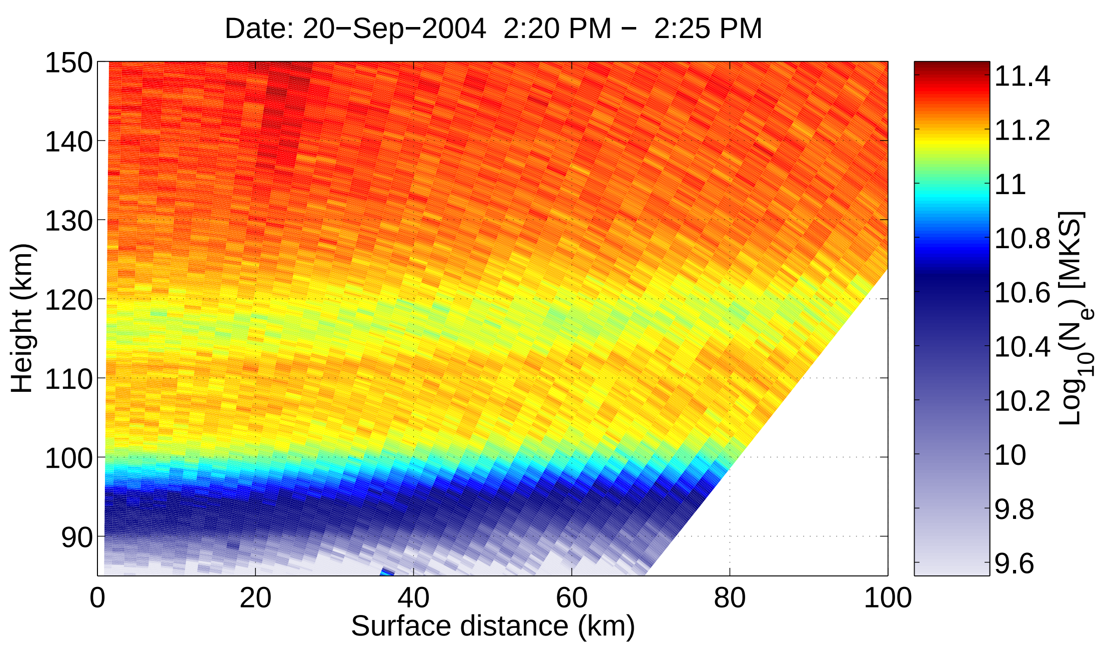

Figure C.61 E-region density map — September 20, 2004 02:20 pm - 02:25 pm.

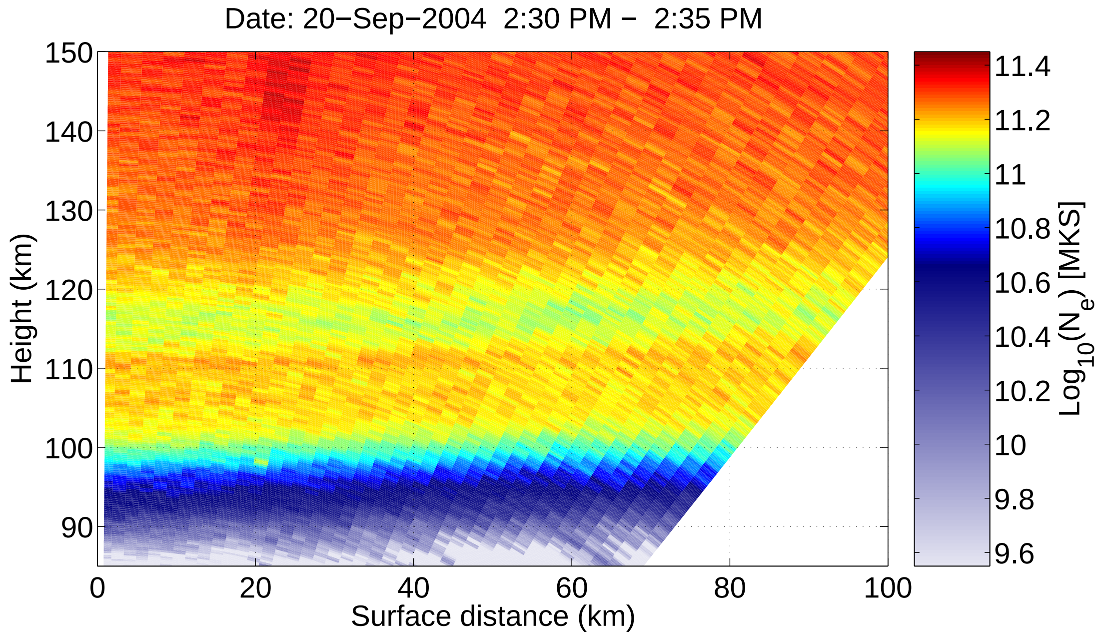

Figure C.62 *E*-region density map — September 20, 2004 02:30 pm - 02:35 pm.

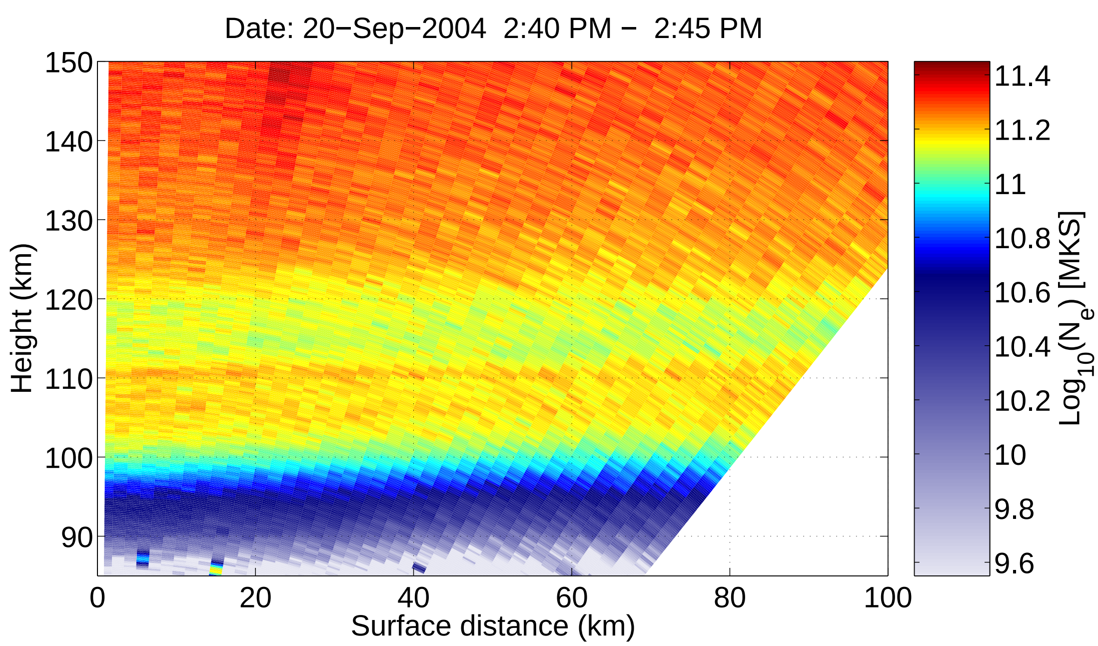

Figure C.63 *E*-region density map — September 20, 2004 02:40 pm - 02:45 pm.

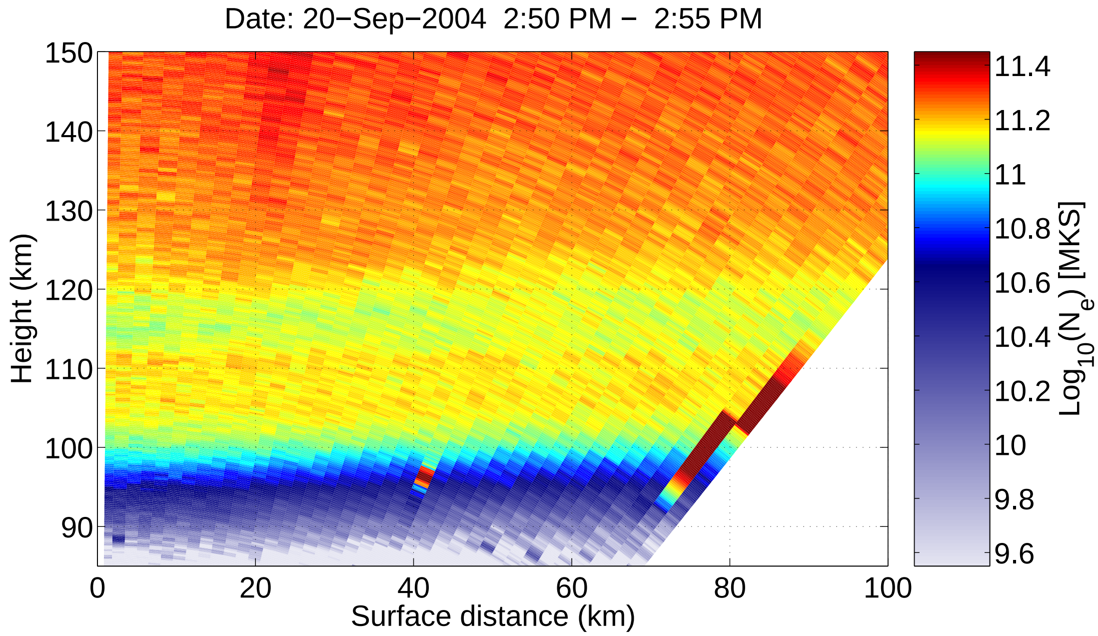

Figure C.64 E-region density map — September 20, 2004 02:50 pm - 02:55 pm.

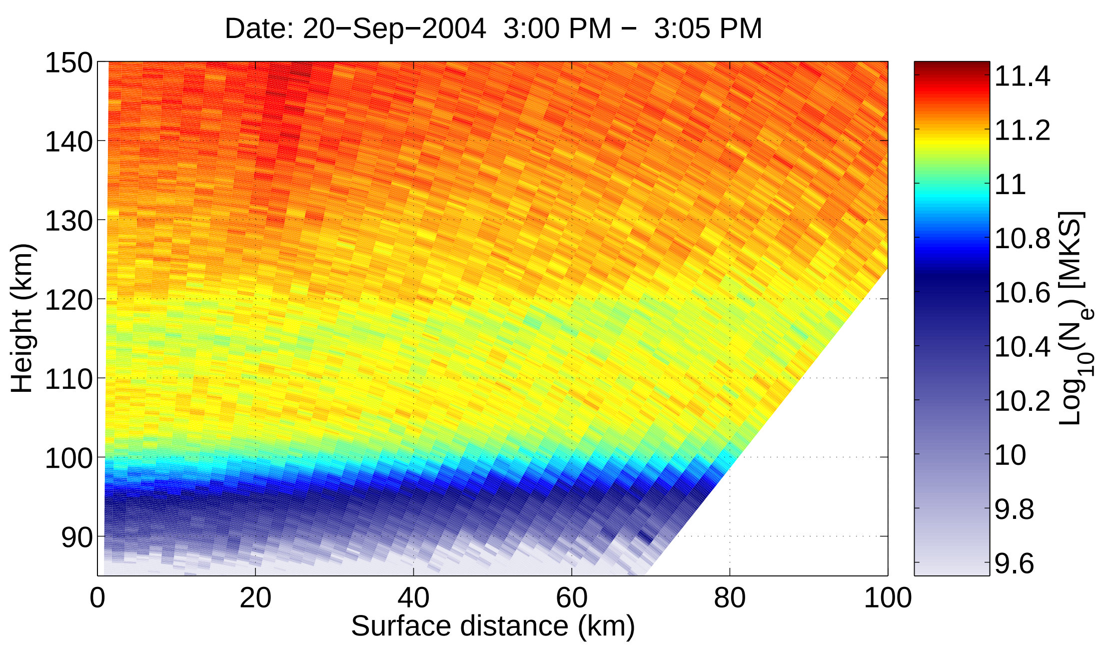

Figure C.65 E-region density map — September 20, 2004 03:00 pm - 03:05 pm.

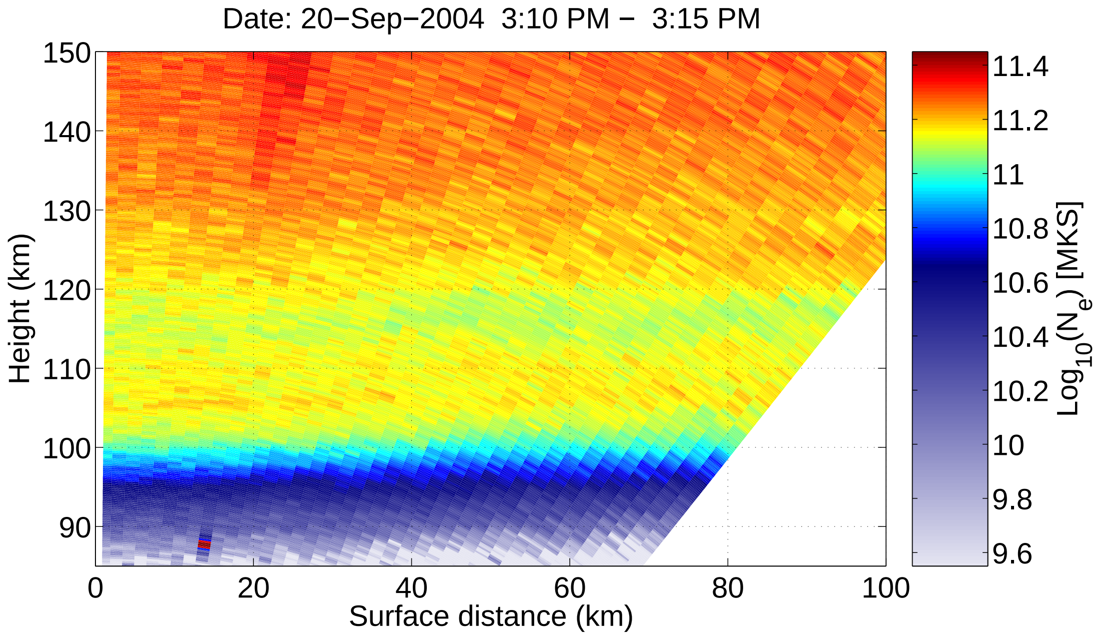

Figure C.66 E-region density map — September 20, 2004 03:10 pm - 03:15 pm.

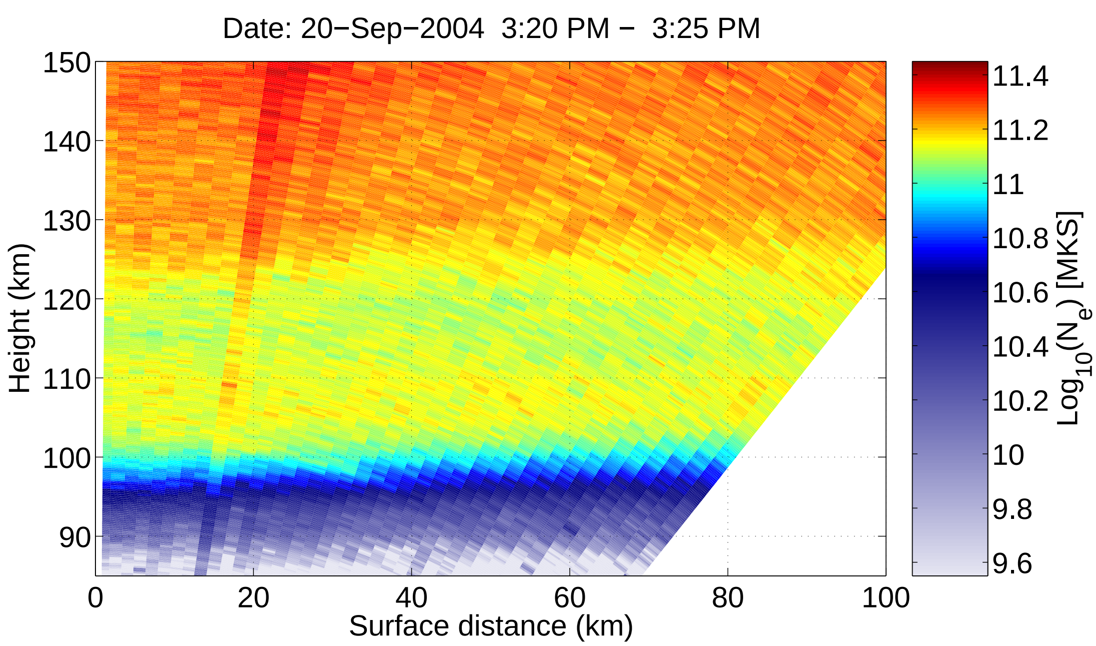

Figure C.67 E-region density map — September 20, 2004 03:20 pm - 03:25 pm.

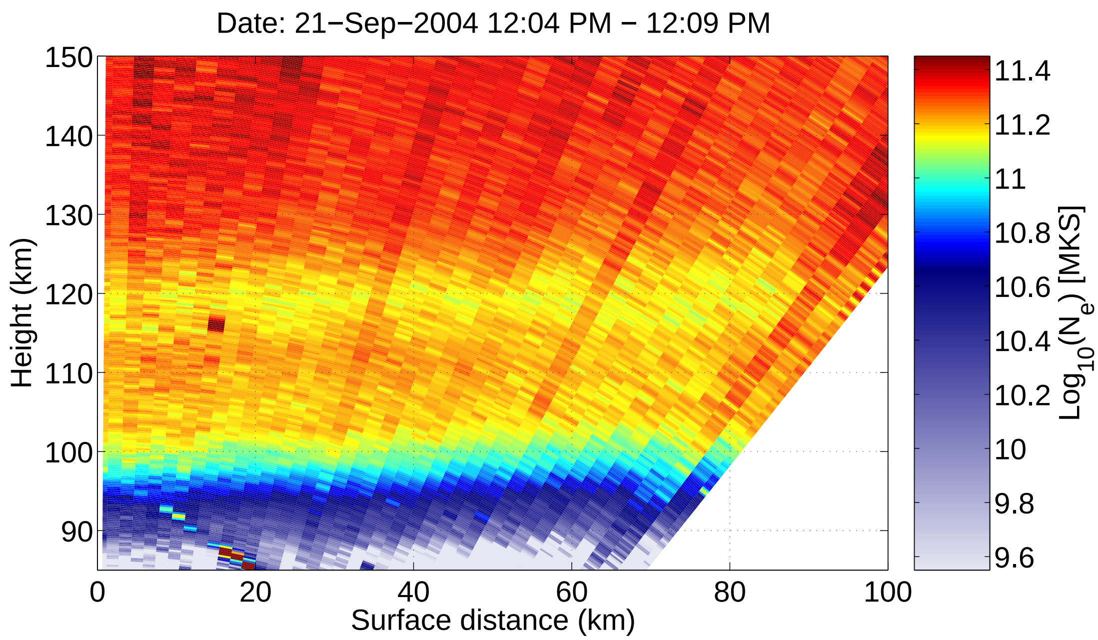

Figure C.68 *E*-region density map — September 21, 2004 12:04 pm - 12:09 pm.

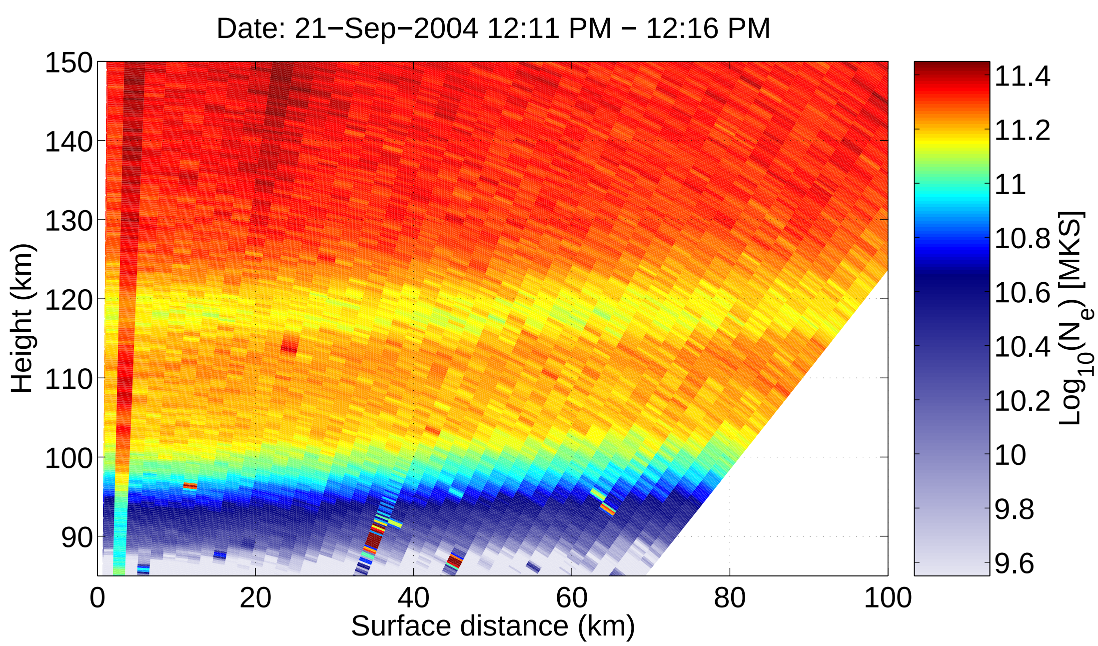

Figure C.69 *E*-region density map — September 21, 2004 12:11 pm - 12:16 pm.

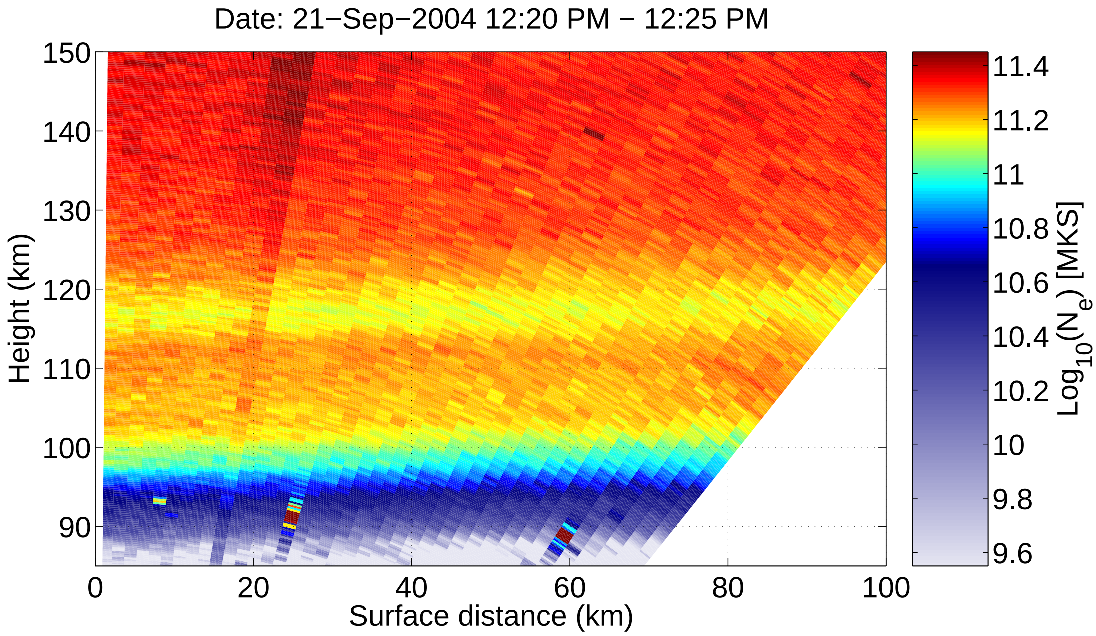

Figure C.70 E-region density map — September 21, 2004 12:20 pm - 12:25 pm.

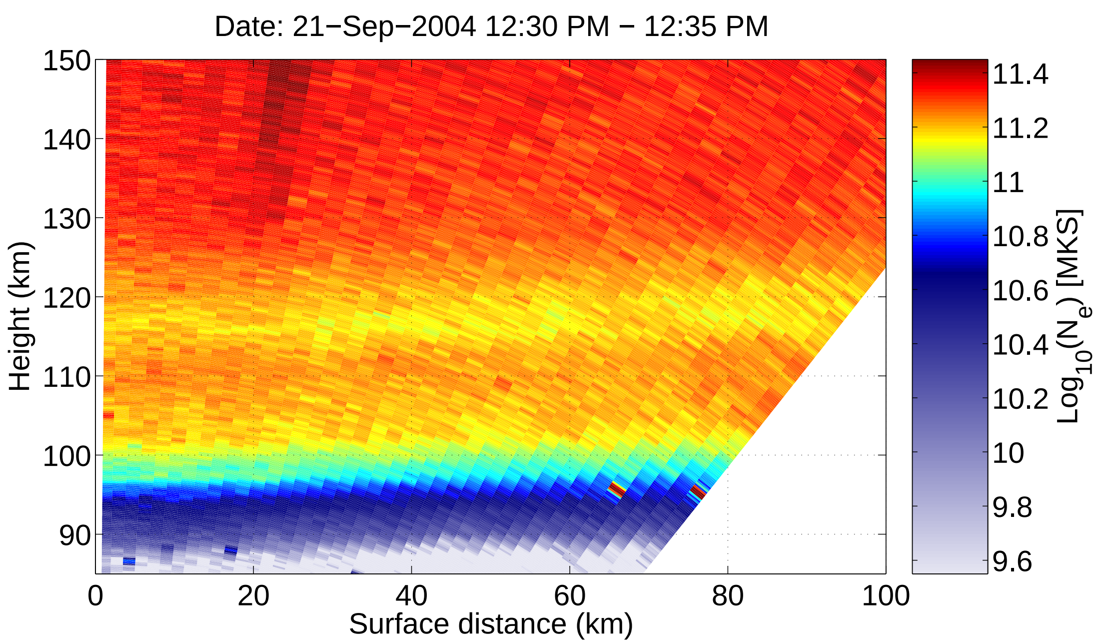

Figure C.71 E-region density map — September 21, 2004 12:30 pm - 12:35 pm.

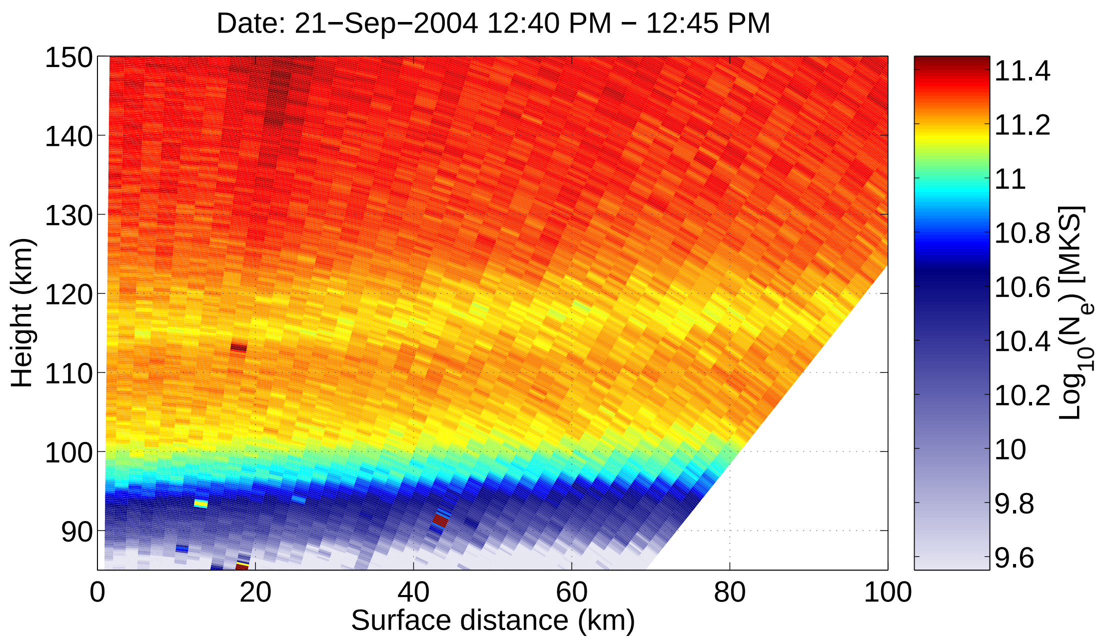

Figure C.72 *E*-region density map — September 21, 2004 12:40 pm - 12:45 pm.

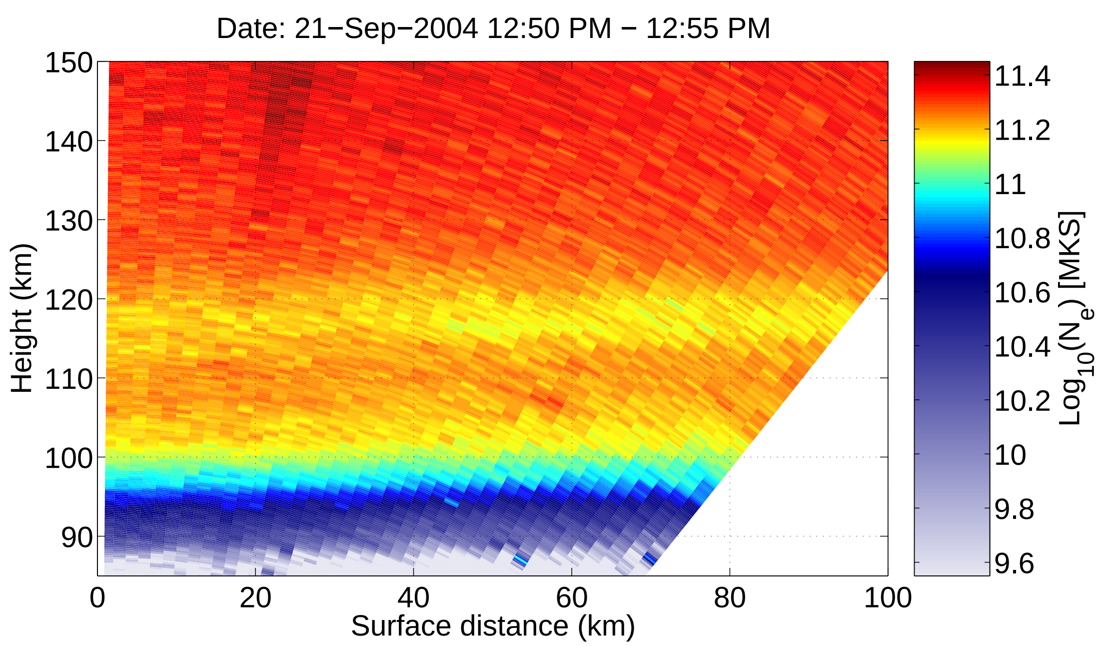

Figure C.73 *E*-region density map — September 21, 2004 12:50 pm - 12:55 pm.

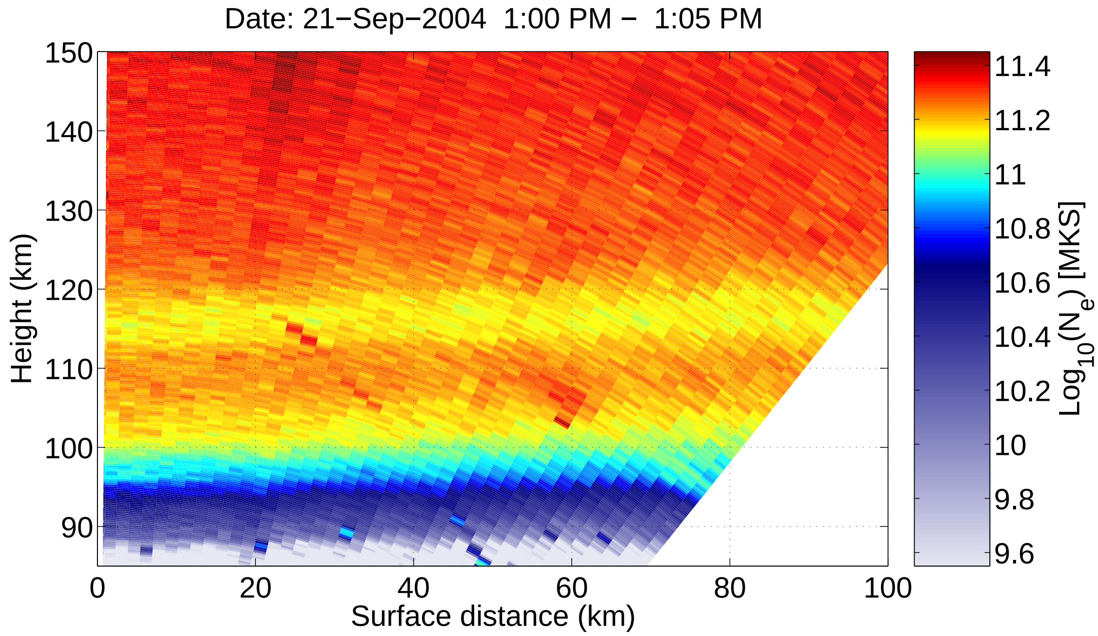

Figure C.74 E-region density map — September 21, 2004 01:00 pm - 01:05 pm.

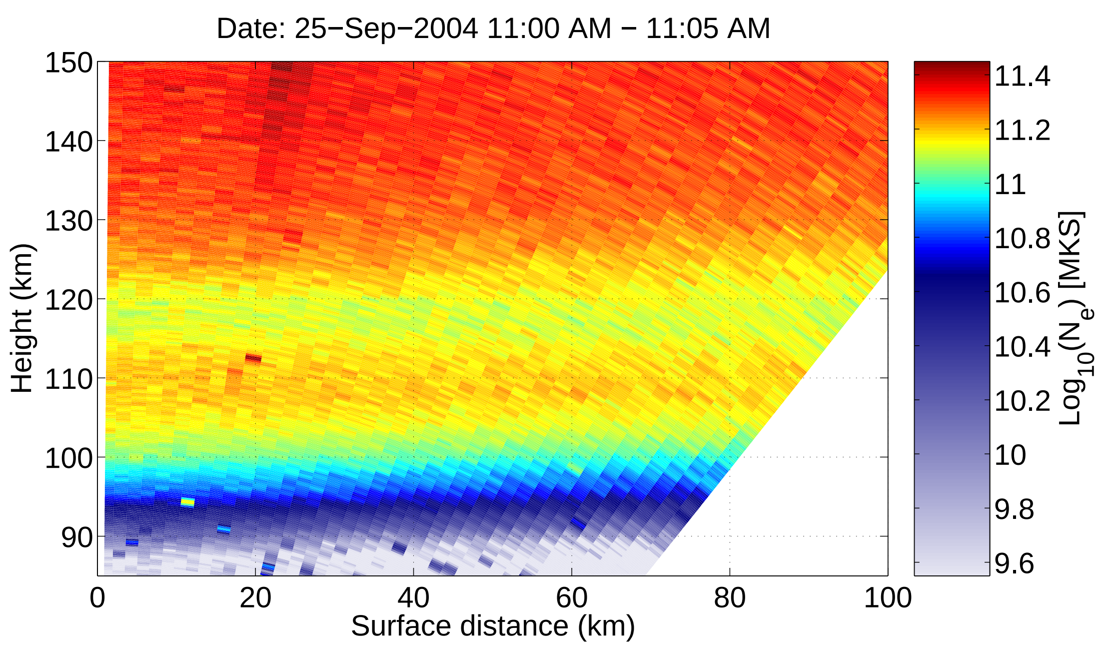

Figure C.75 E-region density map — September 25, 2004 11:00 am - 11:05 am.

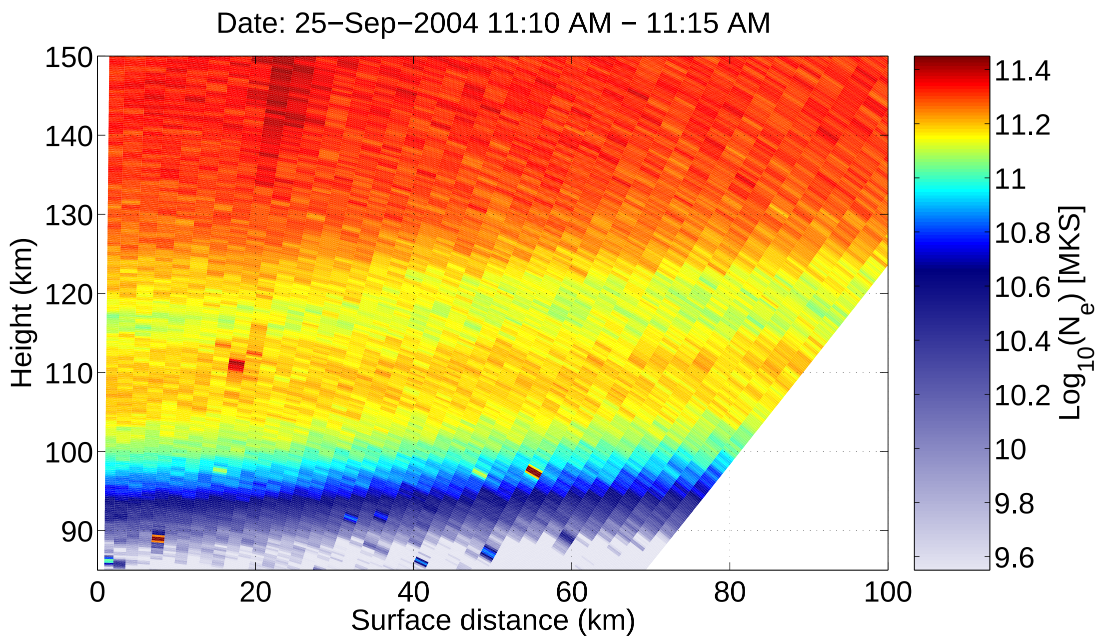

Figure C.76 E-region density map — September 25, 2004 11:10 am - 11:15 am.

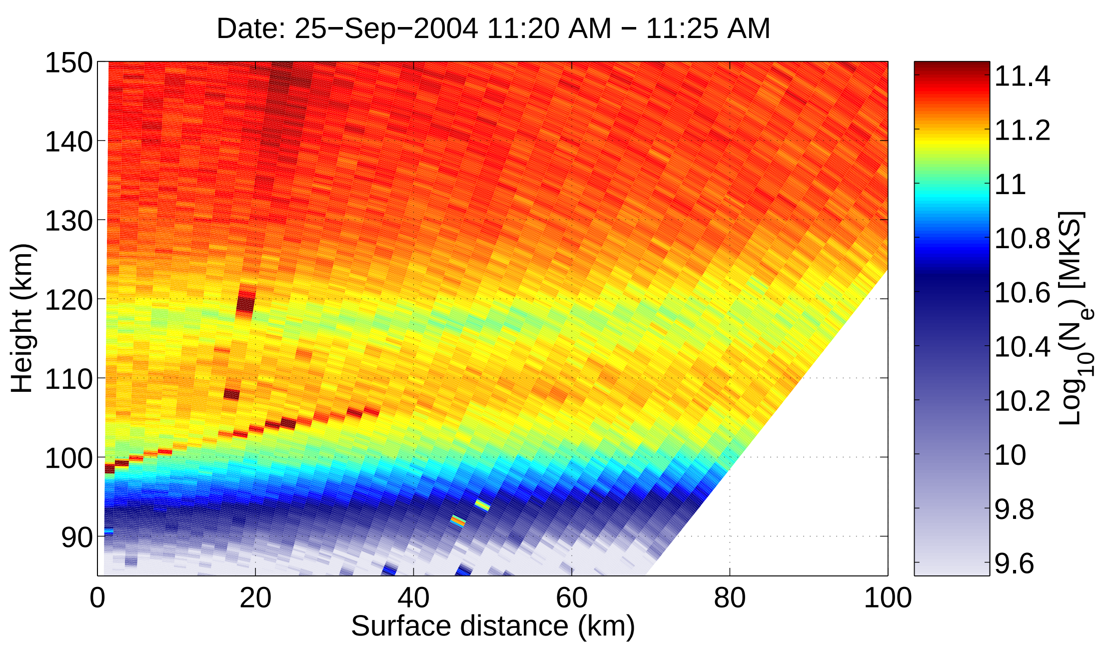

Figure C.77 E-region density map — September 25, 2004 11:20 am - 11:25 am.

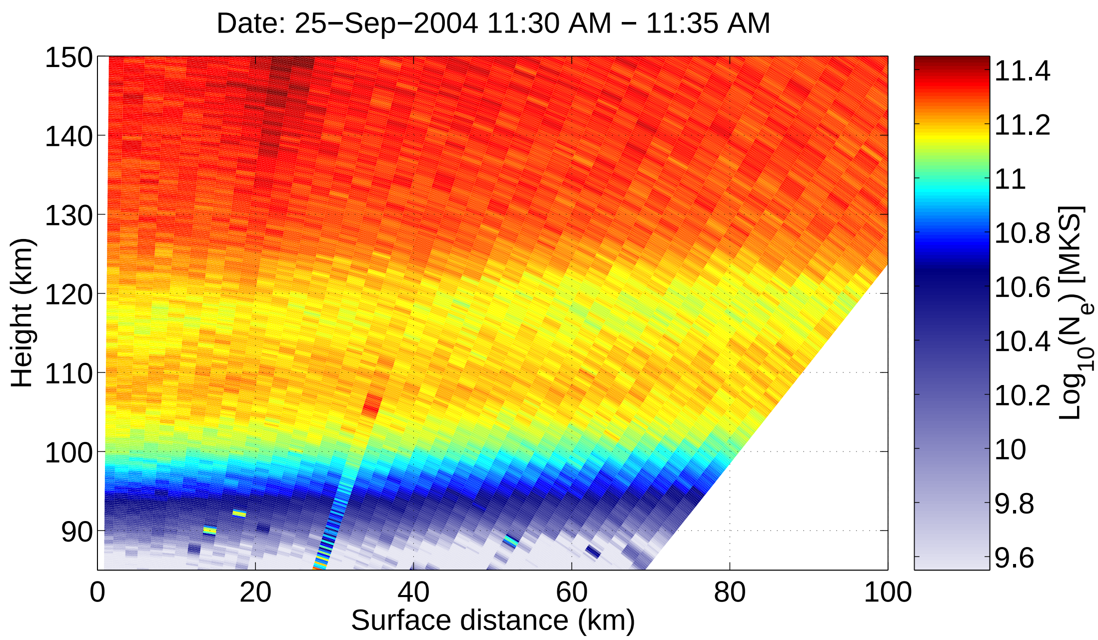

Figure C.78 E-region density map — September 25, 2004 11:30 am - 11:35 am.

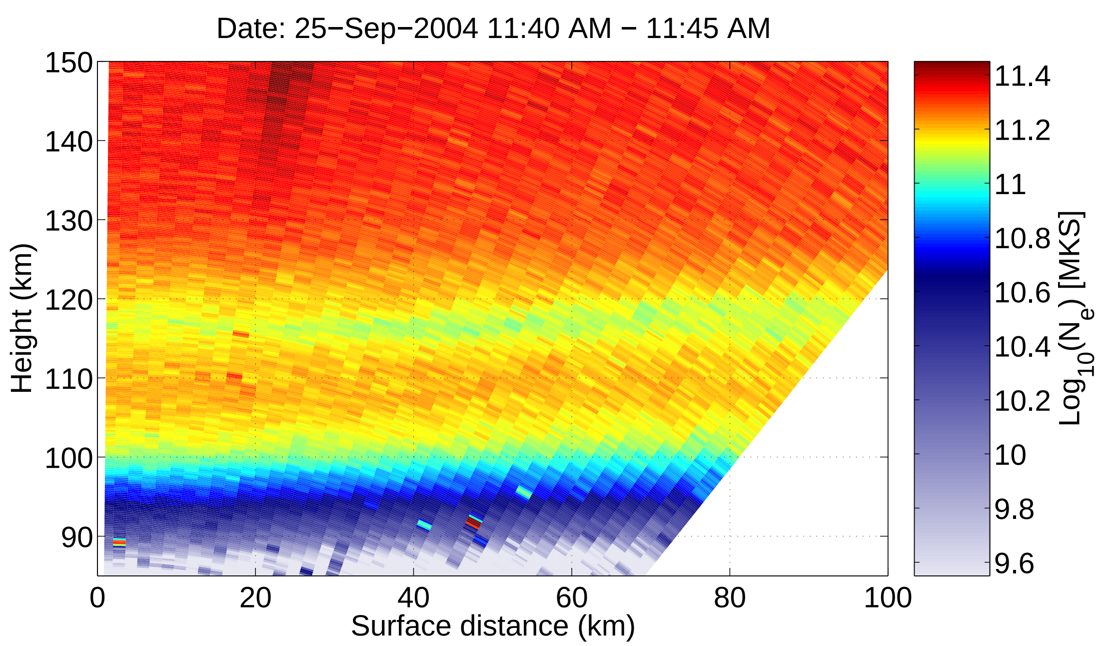

Figure C.79 E-region density map — September 25, 2004 11:40 am - 11:45 am.

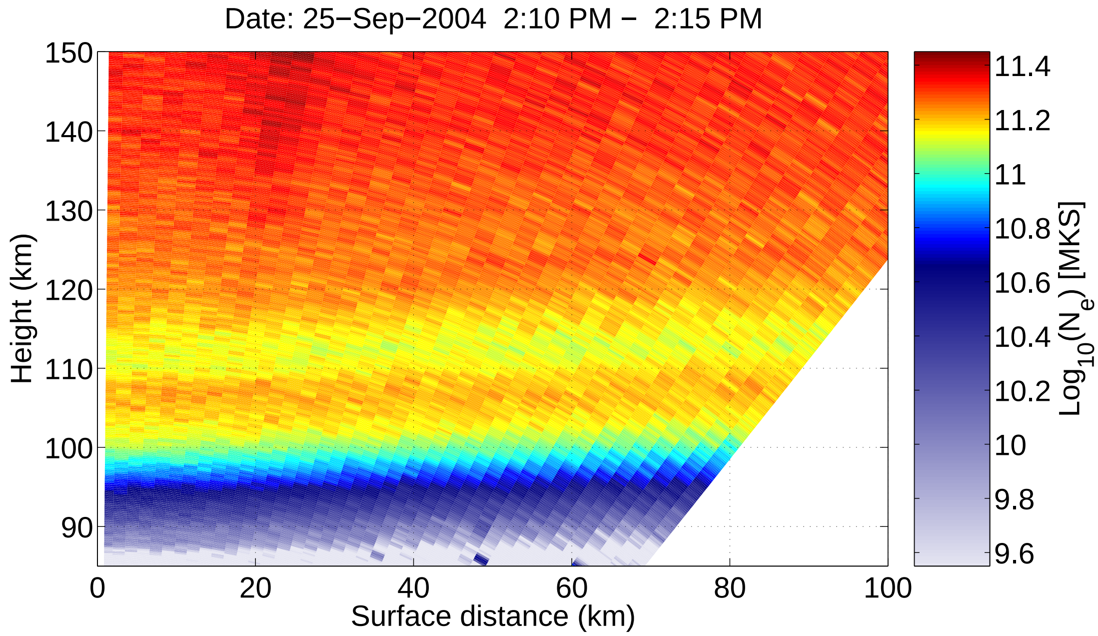

Figure C.80 E-region density map — September 25, 2004 02:10 pm - 02:15 pm.

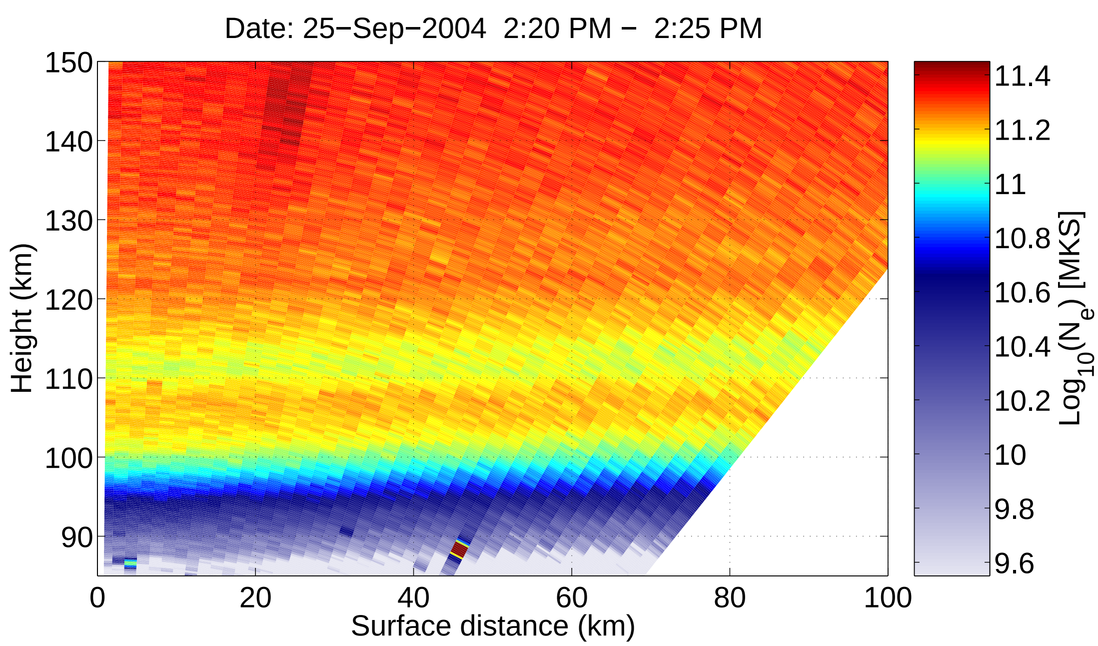

Figure C.81 E-region density map — September 25, 2004 02:20 pm - 02:25 pm.

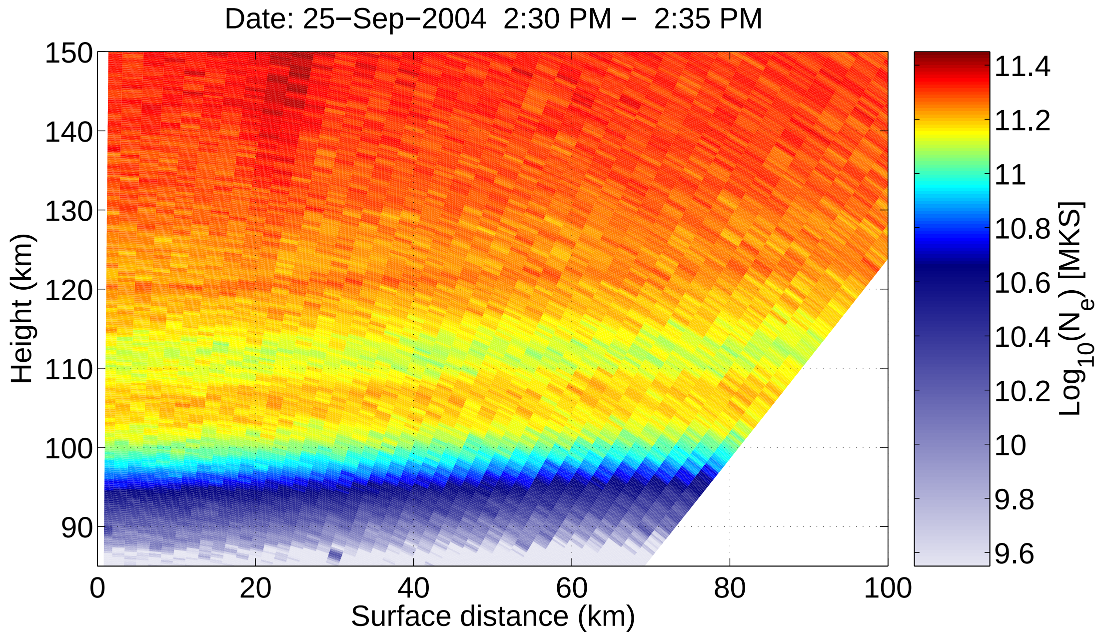

Figure C.82 *E*-region density map — September 25, 2004 02:30 pm - 02:35 pm.

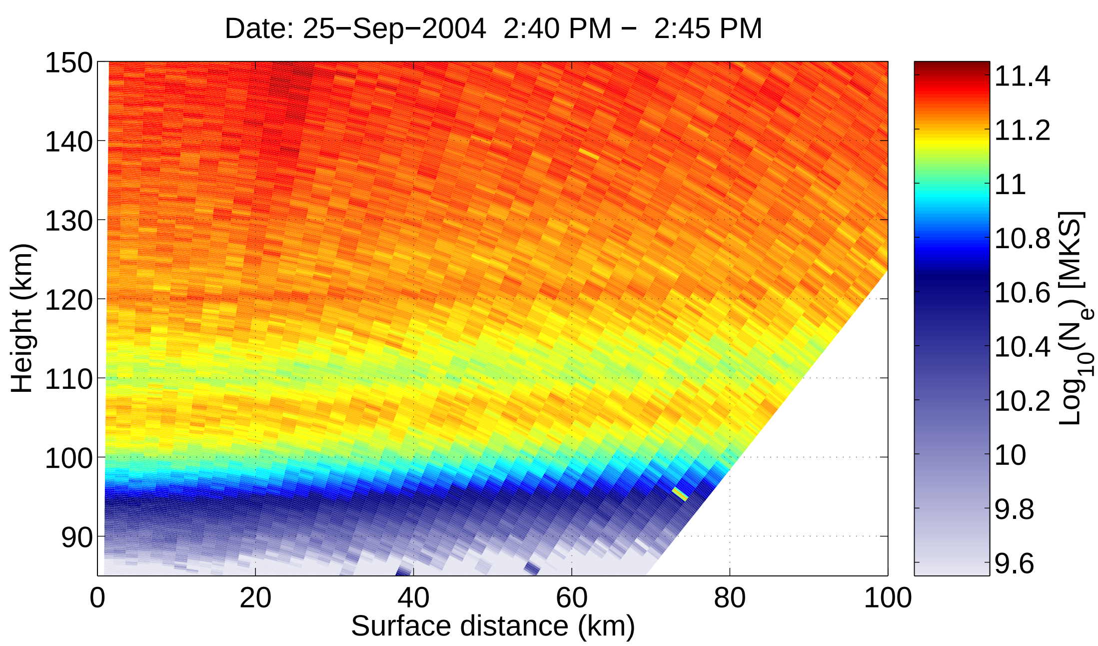

Figure C.83 *E*-region density map — September 25, 2004 02:40 pm - 02:45 pm.

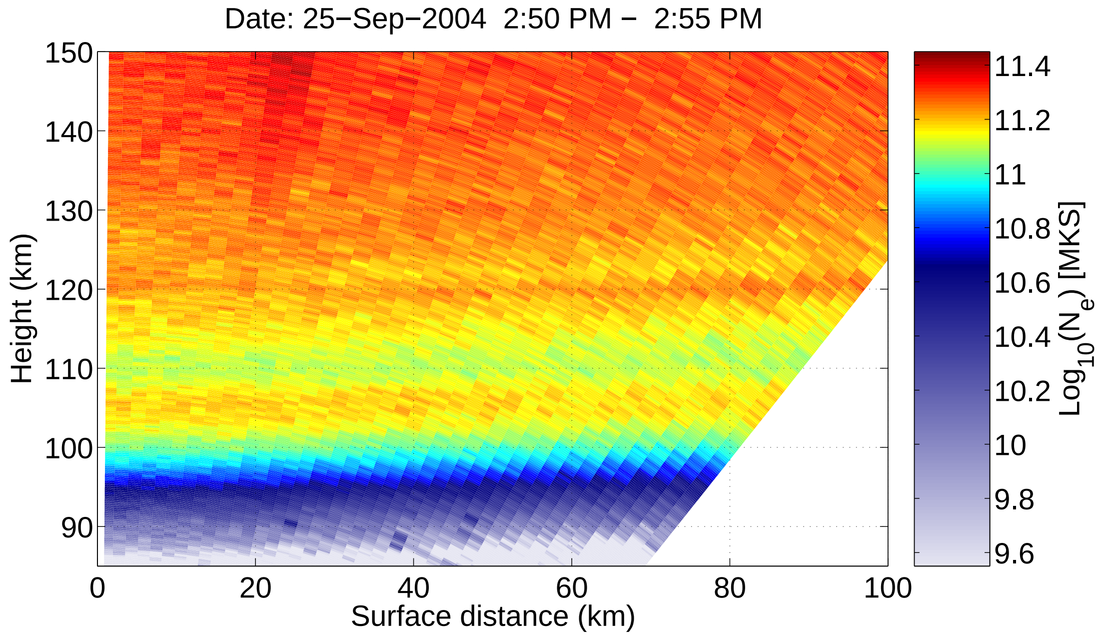

Figure C.84 *E*-region density map — September 25, 2004 02:50 pm - 02:55 pm.

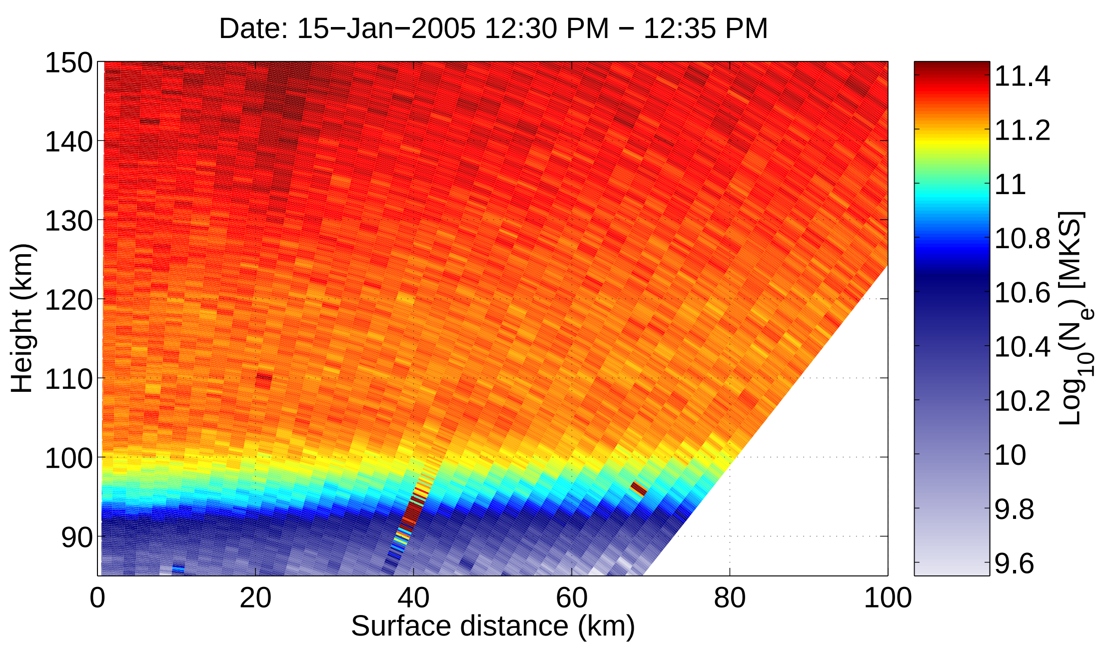

Figure C.85 *E*-region density map — January 15, 2005 12:30 pm - 12:35 pm.

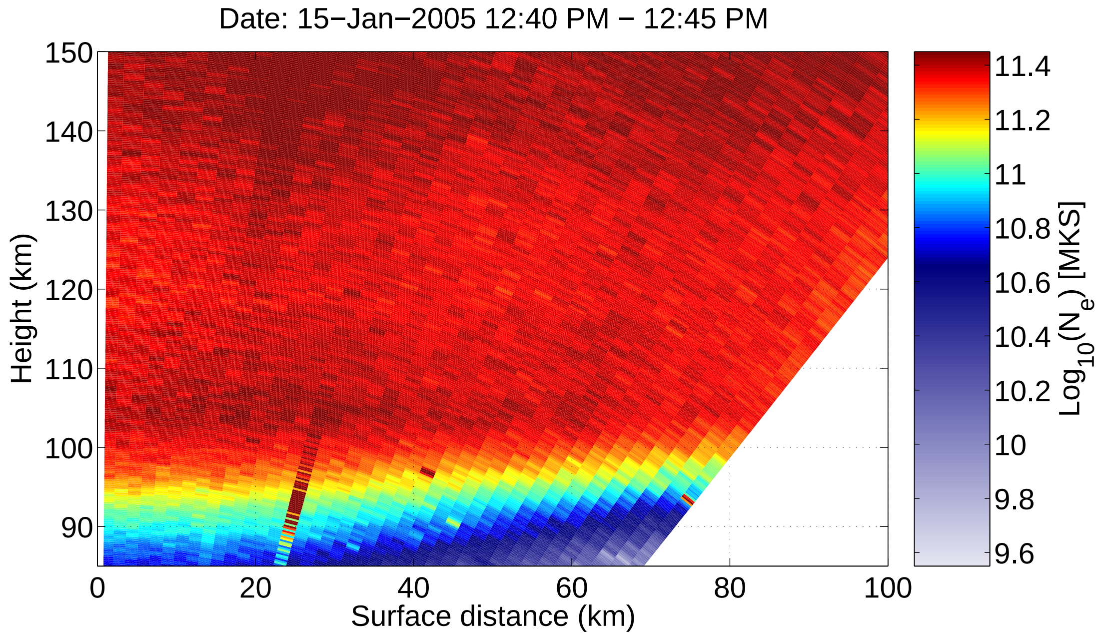

Figure C.86 *E*-region density map — January 15, 2005 12:40 pm - 12:45 pm.

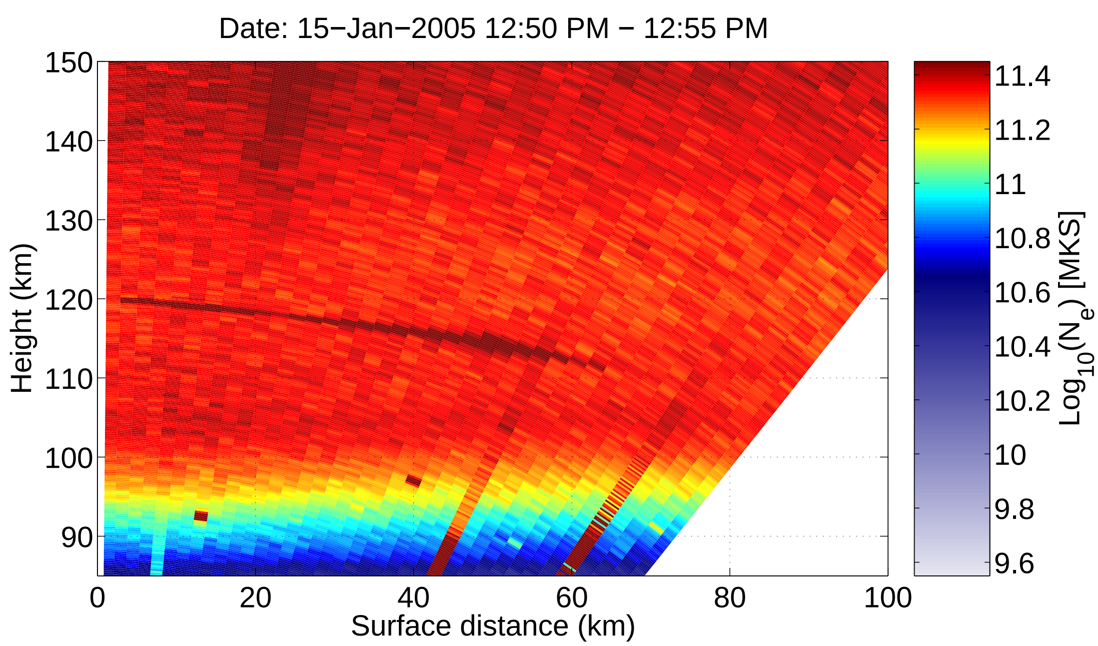

Figure C.87 *E*-region density map — January 15, 2005 12:50 pm - 12:55 pm.

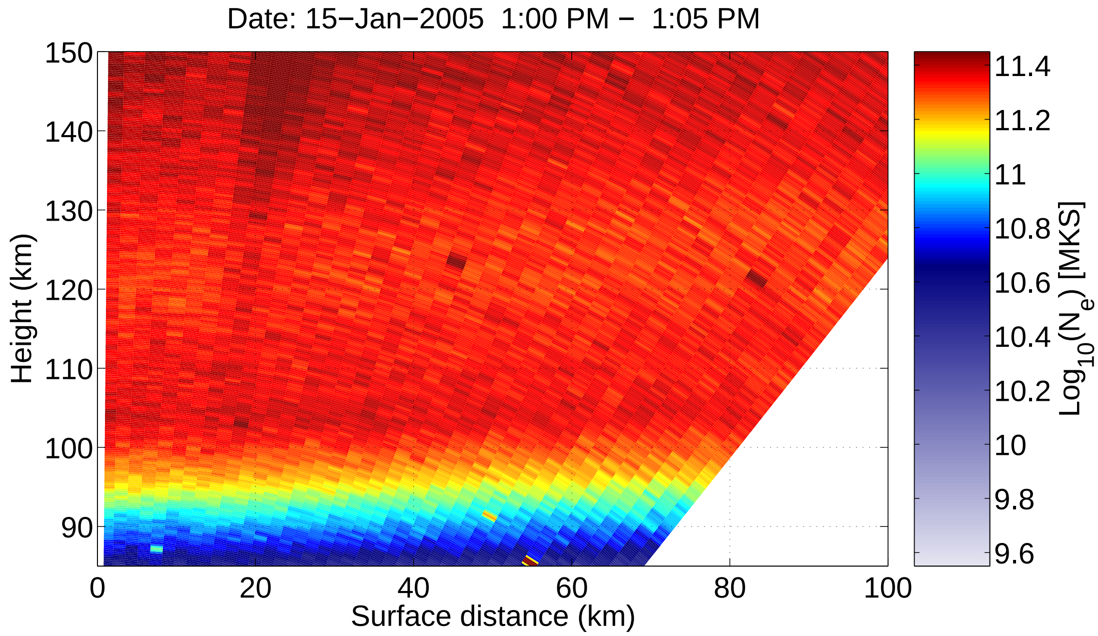

Figure C.88 E-region density map — January 15, 2005 01:00 pm - 01:05 pm.

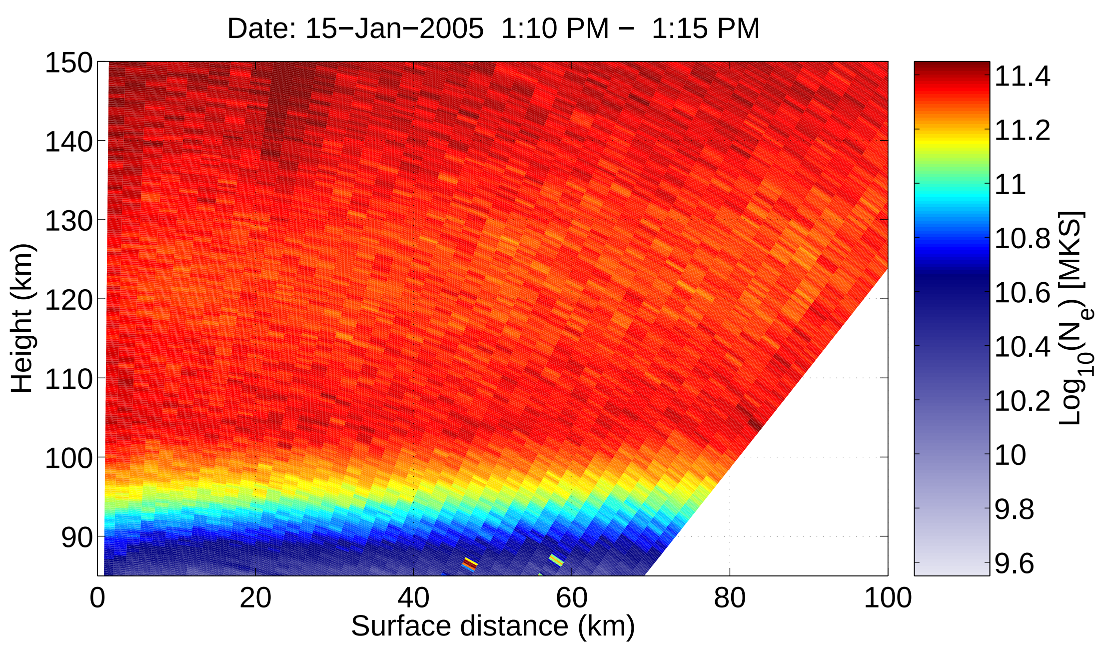

Figure C.89 E-region density map — January 15, 2005 01:10 pm - 01:15 pm.

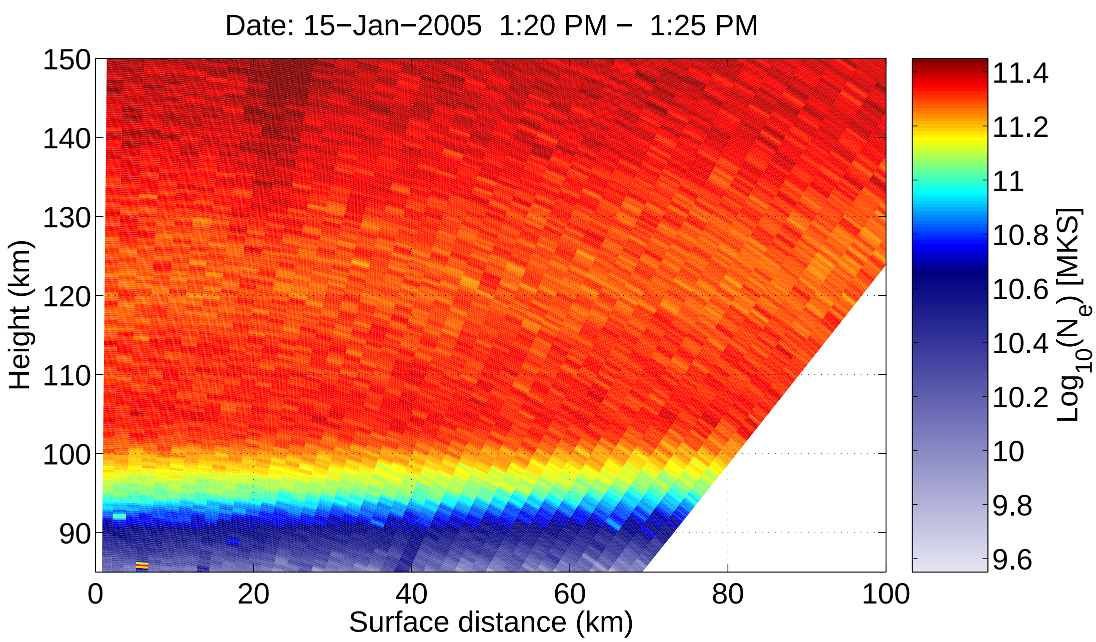

Figure C.90 E-region density map — January 15, 2005 01:20 pm - 01:25 pm.

REFERENCES

Beynon, W. J. G., and P. J. S. Williams, Incoherent scatter of radio waves from the ionosphere, *Reports on Progress in Physics*, *41*(6), 909–955, 1978.

Bilitza, D., International Reference Ionosphere 2000, *Radio Science*, *36*(2), 261–275, 2001.

Blahut, R. E., *Theory of Remote Image Formation*, Cambridge University Press, Cambridge, UK, 2004.

Dougherty, J. P., and D. T. Farley, A theory of incoherent scattering of radio waves by a plasma, *Proceedings of the Royal Society of London. Series A, Mathematical and Physical Sciences*, *259*(1296), 79–99, 1960.

Evans, J. V., Theory and practice of ionosphere study by Thomson scatter radar, *Proceedings of the IEEE*, *57*(4), 496–530, 1969.

Farley, D. T., A theory of incoherent scattering of radio waves by a plasma, 4. The effect of unequal ion and electron temperatures, *Journal of Geophysical Research*, *71*(17), 4091–4098, 1966.

Farley, D. T., Incoherent scatter at radio frequencies, *Journal of Atmospheric and Terrestrial Physics*, *32*(4), 693–704, 1970.

Farley, D. T., J. P. Dougherty, and D. W. Barron, A theory of incoherent scattering of radio waves by a plasma, 2. Scattering in a magnetic field, *Proceedings of the Royal Society of London. Series A, Mathematical and Physical Sciences*, *263*(1313), 238–258, 1961.

Fejer, J. A., Scattering of radio waves by an ionized gas in thermal equilibrium, *Canadian Journal of Physics*, *38*, 1114–1133, 1960.

Fejer, J. A., Scattering of radio waves by an ionized gas in thermal equilibrium in the presence of a uniform magnetic field, *Canadian Journal of Physics*, *39*, 716–740, 1961.

Friedrich, M., K. M. Torkar, G. A. Lehmacher, C. L. Croskey, J. D. Mitchell, E. Kudeki, and M. Milla, Rocket and incoherent scatter radar common-volume electron measurements of the equatorial lower ionosphere, *Geophysical Research Letters*, *33*(L08807), 1–4, 2006.

Gordon, W. E., Incoherent scattering of radio waves by free electrons with applications to space exploration by radar, *Proceedings of the Institute of Radio Engineers*, *46*, 1824–1829, 1958.

Hagfors, T., and R. A. Brockelman, A theory of collision dominated electron density fluctuations in a plasma with applications to incoherent scattering, *The Physics of Fluids*, *14*(6), 1143–1151, 1971.

Hansen, P. C., Analysis of discrete ill-posed problems by means of the L-curve, *SIAM Review*, *34*(4), 561–580, 1992.

Kudeki, E., *ECE 458 Lecture notes on Applications of Radiowave Propagation*, Department of Electrical and Computer Engineering, University of Illinois at Urbana-Champaign, Urbana, Illinois, 2006.

Kudeki, E., and M. Milla, Incoherent scatter spectrum theory for modes propagating perpendicular to the geomagnetic field, *Journal of Geophysical Research*, *111*(A06306), 1–3, 2006.

Kudeki, E., S. Bhattacharya, and R. F. Woodman, A new approach in incoherent scatter F region $E \times B$ drift measurements at Jicamarca, *Journal of Geophysical Research*, *104*(A12), 28,145–28,162, 1999.

Kudeki, E., R. F. Woodman, and Z. Feng, Incoherent scatter radar plasma density measurements at Jicamarca using a transverse-mode differential-phase method, *Geophysical Research Letters*, *30*(5), 1255, 2003.

Kudeki, E., M. Milla, M. Friedrich, G. Lehmacher, and D. Sponseller, ALTAIR incoherent scatter observations of the equatorial daytime ionosphere, *Geophysical Research Letters*, *33*(L08108), 1–5, 2006.

Lehmacher, G. A., C. L. Croskey, J. D. Mitchell, M. Friedrich, F.-J. Lubken, M. Rapp, E. Kudeki, and D. C. Fritts, Intense turbulence observed above mesospheric temperature inversion at equatorial latitude, *Geophysical Research Letters*, *33*(L08808), 1–5, 2006.

Lemnios, W. Z., and A. A. Grometstein, Overview of the Lincoln laboratory ballistic missile defense program, *Lincoln Laboratory Journal*, *13*(1), 9–32, 2002.

Levanon, N., *Radar principles*, Wiley-Interscience publication, New York, 1988.

Li, Y. L., C. H. Liu, and S. J. Franke, Adaptive evaluation of the Sommerfeld-type integral using the Chirp z-Transform, *IEEE transactions on antennas and propagation*, *39*(12), 1788–1791, 1991.

Milla, M., and E. Kudeki, F-region electron density and t_e/t_i measurements using incoherent scatter power data collected at altair, *Annales Geophysicae*, *24*(5), 1333–1342, 2006.

Rastogi, P. K., J. D. Mathews, W.-P. Ying, and J. Rottger, Simultaneous VHF and UHF radar observations of the mesosphere at arecibo during a solar flare: A check on the gradient-mixing hypothesis, *Radio Science*, *23*(97-105), 1988.

Sulzer, M. P., and S. A. González, The effect of electron Coulomb collisions on the incoherent scatter spectrum in the *F* region at Jicamarca, *Journal of Geophysical Research*, *104*(A10), 22,535–22,551, 1999.

Tikhonov, A. N., and V. A. Arsenin, *Solutions of ill-posed problems*, Winston & Sons, Washington, DC, 1977.

Tsunoda, R. T., First incoherent-scatter measurements of the equatorial E layer obtained with the ALTAIR radar, *Geophysical Research Letters*, *22*(7), 847–850, 1995.

Woodman, R. F., Incoherent scattering of electromagnetic waves by a plasma, Ph.D. thesis, Harvard University, Cambridge, Massachusetts, 1967.

Woodman, R. F., On a proper electron collision frequency for a Fokker-Planck collision model with Jicamarca applications, *Journal of Atmospheric and Solar-Terrestrial Physics*, *66*(17), 1521–1541, 2004.

Yeh, K. C., H. Y. Chao, and K. H. Lin, A study of the generalized Faraday effect in several media, *Radio Science*, *34*(1), 139–153, 1999.